

The Transition from Diffuse Molecular Gas to Molecular Cloud Material in Taurus

S. R. FEDERMAN,¹ JOHNATHAN S. RICE,¹ A. M. RITCHEY,² HWHYUN KIM,³ JOHN H. LACY,⁴
 PAUL F. GOLDSMITH,⁵ NICOLAS FLAGEY,^{6,7} GREGORY N. MACE,⁸ AND DAVID L. LAMBERT⁸

—

¹*University of Toledo, Department of Physics and Astronomy, Toledo, OH 43606, USA*

²*Eureka Scientific Inc., Oakland, CA 96402, USA*

³*Gemini Observatory/NSF's NOIRLab, Casilla 603, La Serena, Chile*

⁴*Department of Astronomy, University of Texas at Austin, Austin, TX 78712, USA*

⁵*Jet Propulsion Laboratory, California Institute of Technology, Pasadena, CA 91109, USA*

⁶*Canada France Hawaii Telescope Corporation, Kamuela, HI 96743, USA*

⁷*Space Telescope Science Institute, 3700 San Martin Drive, Baltimore, MD 21218, USA*

⁸*W. J. McDonald Observatory and Department of Astronomy, University of Texas at Austin, Austin, TX 78712, USA*

Submitted to ApJ

ABSTRACT

We study four lines of sight that probe the transition from diffuse molecular gas to molecular cloud material in Taurus. Measurements of atomic and molecular absorption are used to infer the distribution of species and the physical conditions toward stars behind the Taurus Molecular Cloud (TMC). New high-resolution spectra at visible and near infrared wavelengths of interstellar Ca II, Ca I, K I, CH, CH⁺, C₂, CN, and

Corresponding author: S. R. Federman

steven.federman@utoledo.edu, johnathan.s.rice@gmail.com, ritchey.astro@gmail.com, hkim@gemini.edu,
 lacy@astro.as.utexas.edu, paul.f.goldsmith@jpl.nasa.gov, nflagey@stsci.edu, gmace@astro.as.utexas.edu,
 dll@astro.as.utexas.edu

CO toward HD 28975 and HD 29647 are combined with data at visible wavelengths and published CO results from ultraviolet measurements for HD 27778 and HD 30122. Gas densities and temperatures are inferred from C₂, CN, and CO excitation and CN chemistry. Our results for HD 29647 are noteworthy because the CO column density is 10¹⁸ cm⁻² while C₂ and CO excitation reveals a temperature of 10 K and density about 1000 cm⁻³, more like conditions found in dark molecular clouds. Similar results arise from our chemical analysis for CN through reactions involving observations of CH, C₂, and NH. Enhanced potassium depletion and a reduced CH/H₂ column density ratio also suggest the presence of a dark cloud. The directions toward HD 27778 and HD 30122 probe molecule-rich diffuse clouds, which can be considered CO-dark gas, while the sight line toward HD 28975 represents an intermediate case. Maps of dust temperature help refine the description of the material along the four sight lines and provide an estimate of the distance between HD 29647 and a clump in the TMC. An Appendix provides results for the direction toward HD 26571; this star also probes diffuse molecular gas.

1. INTRODUCTION

There are numerous observational studies of diffuse atomic and molecular gas, based of a combination of absorption measurements spanning ultraviolet to radio wavelengths as well as emission lines at cm and mm wavelengths. More recent examples include a number of comprehensive studies (Liszt & Lucas 1996, 1998, 2002; Welty & Hobbs 2001; Pan et al. 2005; Sonnentrucker et al. 2007; Sheffer et al. 2008; Jenkins 2009; Burgh et al. 2010; Gerin et al. 2010; Jenkins & Tripp 2011; Indriolo & McCall 2012). The same can be said of dark molecular clouds from observations at infrared through radio wavelengths (e.g., Myers & Benson 1983; Myers et al. 1983; Gaida et al. 1984; Patel et al. 1995, 1998; Mizuno et al. 2001; Pineda et al. 2008; Rosolowsky et al. 2008; Pineda et al. 2010; Lacy et al. 2017). However, there are few published studies of dark clouds with a focus on absorption at visible wavelengths for direct comparison with the efforts on diffuse atomic and molecular clouds. Here we define dark clouds as having CO column densities, $N(\text{CO})$, in excess of 10¹⁷ cm⁻² so that a

substantial fraction of elemental carbon is in gas-phase CO. Such column densities are significantly greater than those in sight lines used as benchmarks for diffuse molecular gas, such as toward ζ Oph, where the CO column density is $\sim 10^{15} \text{ cm}^{-2}$ (Lambert et al. 1994). This regime of dark clouds with $N(\text{CO})$ of 10^{17} cm^{-2} contains the final stages of the chemical transitions from atomic to molecular gas for carbon (C^+ to CO), nitrogen (N to NH_3), and oxygen (O to H_2O) and where CO, CO_2 , and H_2O ices begin to coat interstellar dust grains. In this paper, we present a detailed study of this regime for portions of the Taurus Molecular Cloud (TMC) probed by the background stars HD 28975 and HD 29647. In particular, data on Ca II, K I, CN, CH^+ , CH, C_2 , and CO are analyzed and compared with available results as well as newly acquired data for the nearby sight lines toward HD 27778 and HD 30122.

Previous results for two directions, those toward HD 29647 and HD 200775, are used as guides on how to proceed. It is important to note that these sight lines are dominated by a single velocity component. Crutcher (1985) combined measurements of atomic and molecular absorption at visible wavelengths with millimeter-wave emission from CO and its isotopologues, CN, HCN, and HCO^+ . His detailed analysis revealed $N(\text{CO})$ of about $1.5 \times 10^{17} \text{ cm}^{-2}$, H_2 densities of 800 cm^{-3} , and a kinetic temperature of 10 K. Earlier C_2 measurements were described by Hobbs et al. (1983) and Lutz & Crutcher (1983), and subsequently published results on CH, C_2 , and CN appeared in Thorburn et al. (2003). All the previously published data at visible wavelengths for HD 29647 were acquired at moderate spectral resolution (about 7 to 15 km s^{-1}). A comprehensive analysis of atomic and molecular absorption toward HD 200775 (Federman et al. 1997) at high-spectral resolution (2 to 3 km s^{-1}) was followed by measurements on CO absorption at ultraviolet wavelengths with the *International Ultraviolet Explorer* (Knauth et al. 2001) and the *Far Ultraviolet Spectroscopic Explorer* (FUSE) (Sheffer et al. 2008). These measurements probed the Photon Dominated Region (PDR) in NGC 7023 in front of HD 200775. The results indicate $N(\text{CO}) = 1.9 \times 10^{17} \text{ cm}^{-2}$, proton densities [$n(\text{H}) + 2n(\text{H}_2)$] between 300 and 900 cm^{-3} , and a kinetic temperature of 40 K. Here, we extend this body of work through high-resolution observations (about 2.5 and 6.5 km s^{-1} , respectively) in the

visible and near infrared toward HD 28975 and HD 29647, combined with similar-quality results for the nearby directions toward HD 27778 and HD 30122.

In order to place our study into context, Figure 1 shows a map of ^{13}CO intensity (Pineda et al. 2010) indicating the lines of sight to HD 27778, HD 28975, HD 29647, and HD 30122. The more reddened stars (HD 28975 and HD 29647) lie behind regions containing filaments seen in ^{13}CO . Federman et al. (1994) noted that HD 27778 samples gas near L 1506, while HD 28975 and HD 29647 probe material in L 1529 and Heiles Cloud-2, respectively (see their Fig. 4c). The direction to HD 30122 lies beyond the ^{13}CO emission in Fig. 1. Also indicated in Fig. 1 are the sight lines toward embedded and background sources in Taurus that were used by Lacy et al. (2017) in their study of the CO/ H_2 ratio. These targets lie along paths with more intense and filamentary structures seen in ^{13}CO emission. The results from Lacy et al. (2017) are discussed further below when we consider the small, parsec scale variations in $N(\text{CO})$.

The outline for the remainder of the paper is the following. Section 2 provides an overview of our extensive set of observations: absorption from Ca II $\lambda 3933$, Ca I $\lambda 4226$, K I $\lambda 7698$ and from molecular bands CH [$B-X$ (0, 0) and $A-X$ (0, 0)], CH^+ [$A-X$ (0, 0) and (1, 0)], C_2 [$A-X$ (2, 0)], CN [$B-X$ (0, 0), (1, 0), and $A-X$ (2, 0)], NH [$A-X$ (0, 0)], and CO [2-0 rovibration]. The photometric data at infrared wavelengths are also described here. Section 3 presents the results from the absorption-line measurements and the chemical and excitation analyses we perform on them. Maps of dust temperature derived from the far infrared (FIR) data in the vicinity of the four stars are presented in this section and the enhanced FIR emission toward HD 29647 is used to estimate the distance between the star and the cloud. The discussion in Section 4 focuses on interpreting our work in terms of the transition from diffuse atomic and molecular gas to material in a molecular cloud. We attempt to integrate many of the previous efforts on molecular gas in Taurus into a self-consistent picture. Final remarks appear in Section 5. Appendix A provides the total equivalent widths determined from our spectra with comparisons to other measurements, while Appendices B and C discuss an analysis of ionization balance for calcium and a description of the line of sight toward HD 26571 from available data.

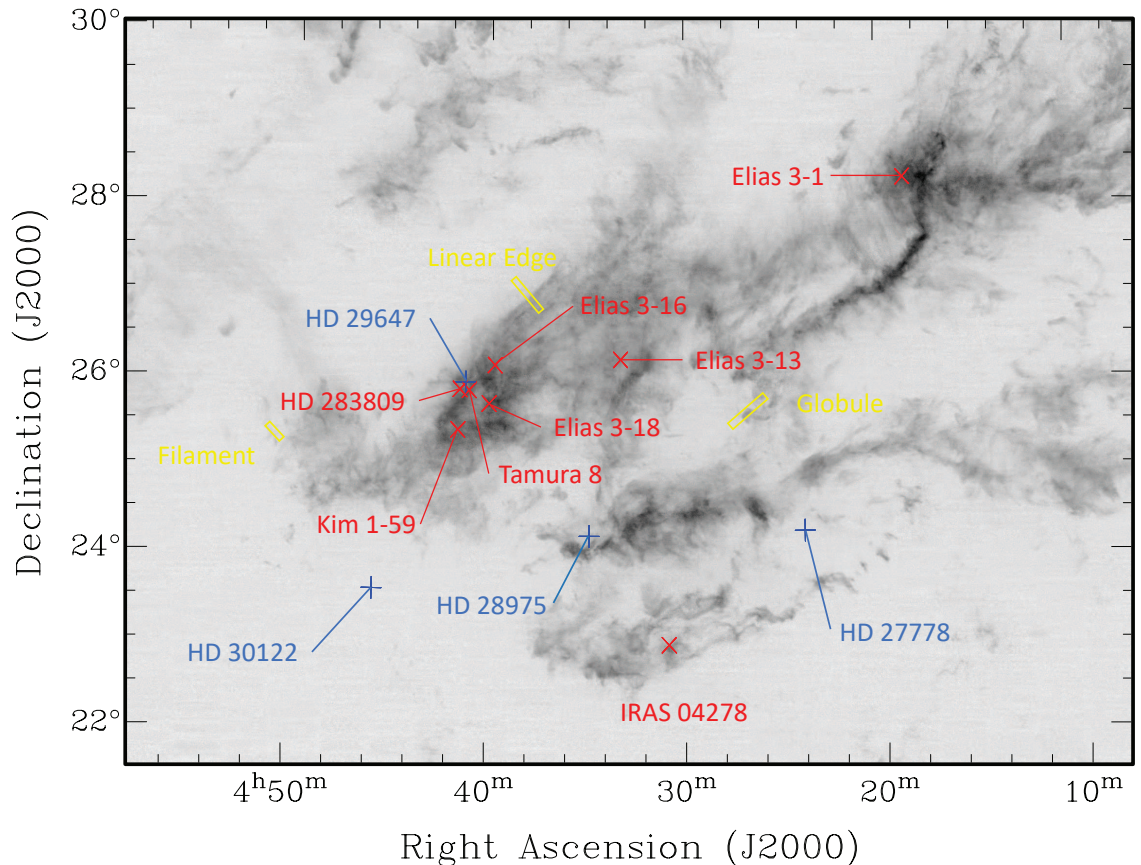


Figure 1. A map of ^{13}CO intensity for the Taurus Molecular Cloud from Pineda et al. (2010) providing the positions of stars discussed in the text. Our targets, HD 27778, HD 28975, HD 29647, and HD 30122, are shown in blue with plus signs, while those from Lacy et al. (2017) are shown in red and marked with an x. The regions labeled as the Filament, the Linear Edge, and the Globule (Goldsmith et al. 2010) are approximately represented by yellow rectangles.

2. OBSERVATIONS

Relevant data for the four stars appear in Table 1, where equatorial positions, apparent magnitudes at B , V , and K , spectral types, $E(B - V)$, and distances derived from *Gaia* Data Release 2 (DR2) are given. For the two stars with CO measurements at IR wavelengths, HD 28975 and HD 29647, the Table also provides K magnitudes. The coordinates come from the SIMBAD Database, operated at Centre de Données Astronomiques de Strasbourg (CDS) (Wenger et al. 2000), while the distances are based on the parallaxes in the database from *Gaia* DR2 discussed by Bailer-Jones et

al. (2018)⁸. Specific references for the other data are given in the table. In what follows, we describe the spectroscopic and photometric measurements for our study.

Table 1. Stellar Data

Star	R. A. (2000) ^a (<i>h.m.s</i>)	DEC (2000) ^a (<i>°.:''</i>)	<i>B</i>	<i>V</i>	<i>K</i>	SpT	<i>E(B − V)</i>	Distance ^b (pc)
HD 27778	04:24:00	+24:18:04	6.54 ^c	6.36 ^c	...	B3V ^d	0.37 ^e	224(2) ^f
HD 28975	04:34:50	+24:14:40	9.90 ^c	9.10 ^c	7.11 ^g	A4III ^h	0.60 ^h	194(2)
HD 29647	04:41:08	+25:59:34	9.22 ^h	8.31 ^h	5.36 ^g	B9III Hg-Mn ^d	1.09 ⁱ	155(2)
HD 30122	04:45:42	+23:37:41	6.41 ^c	6.34 ^c	...	B5III ^d	0.23 ^j	256(4)

^aSIMBAD – Wenger et al. 2000.

^b*Gaia* DR2 – Bailer-Jones et al. 2018.

^cTYCHO Catalog – Høg et al. 2000.

^dMooley et al. 2013.

^eJensen et al. 2007.

^fNumbers in parentheses are uncertainties in distance.

^g2MASS Catalog – Cutri et al. 2003.

^hDucati 2002.

ⁱCrutcher 1985.

^jFitzpatrick & Massa 2007.

2.1. *Tull Spectrograph*

Observations of HD 28975 and HD 29647 were acquired with the 2.7 m Harlan J. Smith Telescope (HJST) at McDonald Observatory using the Tull (2dcoudé) Spectrograph (TS, Tull et al. 1995) in its high-resolution mode (TS21). The TS data were obtained over the course of four nights in 2017 September. All of the observations employed the E1 grating with a 250 μm slit (Slit 3) and a

⁸ <http://gaia.ari.uni-heidelberg.de/tap.html>

2048 × 2048 CCD (TK3). Three separate wavelength settings were utilized. The first one provided access to the CN $B-X$ (0, 0) band near 3874 Å, the CH⁺ $A-X$ (0, 0) transition at 4232 Å, the CH $A-X$ (0, 0) transition at 4300 Å, the Ca II K line at 3933 Å, and the Ca I transition at 4226 Å. The second wavelength setting yielded data on the C₂ $A-X$ (2, 0) band near 8757 Å and the ^SR₂₁(0) line of the CN $A-X$ (2, 0) band at 7871.644 Å. A third setting was necessary to cover the K I line at 7698 Å. Multiple 30-minute exposures were taken of HD 28975 and HD 29647 at each wavelength setting. A set of 10 biases and 10 flats (per setting) were obtained each night, while Th-Ar comparison spectra were recorded throughout the night at intervals of 2–3 hours. Four 30-minute dark frames were acquired on the first night of the run.

The raw TS data were reduced using standard procedures within the Image Reduction and Analysis Facility (IRAF) environment. The overscan region in each of the raw images was fitted with a low-order polynomial and the excess counts were removed. An average bias was created for each night and was used to correct the darks, flats, stellar exposures, and comparison lamp frames. No dark correction was necessary because the level of dark current was found to be insignificant after the bias was removed. Cosmic rays were eliminated from the stellar and comparison lamp exposures. Any cosmic rays present in individual flat lamp exposures were effectively removed by taking the median of all flats for a given night. Scattered light was modeled in the dispersion and cross-dispersion directions and subtracted from the stellar exposures and from the median flat. The flat was then normalized to unity and divided into the stellar and comparison lamp frames. One-dimensional spectra were extracted from the processed images by summing across the width of each order. The extracted stellar spectra were calibrated in wavelength space after identifying emission lines in the Th-Ar comparison spectra. Finally, the wavelength calibrated spectra were shifted to the reference frame of the Local Standard of Rest (LSR). For these sight lines in Taurus, the difference between heliocentric and LSR velocities is about +10 km s⁻¹.

The multiple exposures of HD 28975 and HD 29647 obtained at a particular wavelength setting were co-added to maximize the signal-to-noise (S/N) ratio achieved in the final spectra. The co-added spectra were then normalized to the continuum by fitting low-order polynomials to regions free of

interstellar absorption within small spectral windows surrounding the interstellar lines of interest. From measurements of the widths of Th I emission lines in the comparison spectra, we find that a resolving power of $R = \lambda/\Delta\lambda \approx 125,000$ was achieved for the observations covering the short wavelength lines and the C₂ band. For the observations covering the K I line, which were acquired on the last night of the run, a somewhat lower resolving power of $R \approx 110,000$ was attained. The S/N ratios achieved in the final co-added spectra of HD 28975 and HD 29647 were ~ 30 in the vicinity of the CN *B–X* and Ca II lines, ~ 80 near the CH, CH⁺, and Ca I transitions, ~ 150 near the C₂ and K I features, and ~ 250 near the CN *A–X* transition at 7871 Å.

A similar set of TS spectra for gas toward HD 30122 was acquired in 2019 September and December. These observations employed the short wavelength setting (covering the CN *B–X*, CH, CH⁺, Ca I, and Ca II lines), and the K I setting, but did not include the setting covering the C₂ band. The procedures used for obtaining and reducing the data were the same as those described above. The resolving power of the spectrograph was essentially unchanged for these observing runs compared to the previous one. The resulting S/N ratios were ~ 100 and ~ 140 near the CN *B–X* and Ca II lines, respectively, ~ 170 near the CH, CH⁺, and Ca I transitions, and ~ 40 near the K I line.

Figure 2 displays TS spectra showing molecular absorption from CN *B–X* (0, 0) R(0), CH $\lambda 4300$, CH⁺ $\lambda 4232$, followed by atomic absorption from Ca I, K I, and Ca II. The lines toward HD 28975 appear on the left side, and those toward HD 29647 on the right. Numerous stellar features complicate the analysis of the spectra obtained for HD 29647 (a HgMn star). For example, the interstellar CH $\lambda 4300$ line is partially blended with a stellar Mn II line that has a laboratory wavelength of 4300.25 Å (see Figure 2). In addition, the Ca II $\lambda 3933$ line is most likely a complicated blend of stellar and interstellar absorption. (As a result, we make no attempt to derive a Ca II column density toward HD 29647.) The poorer S/N ratio obtained for TS spectra acquired below 4000 Å arises from decreased stellar flux caused by a combination of significant reddening by foreground dust and less sensitivity for the spectrograph.

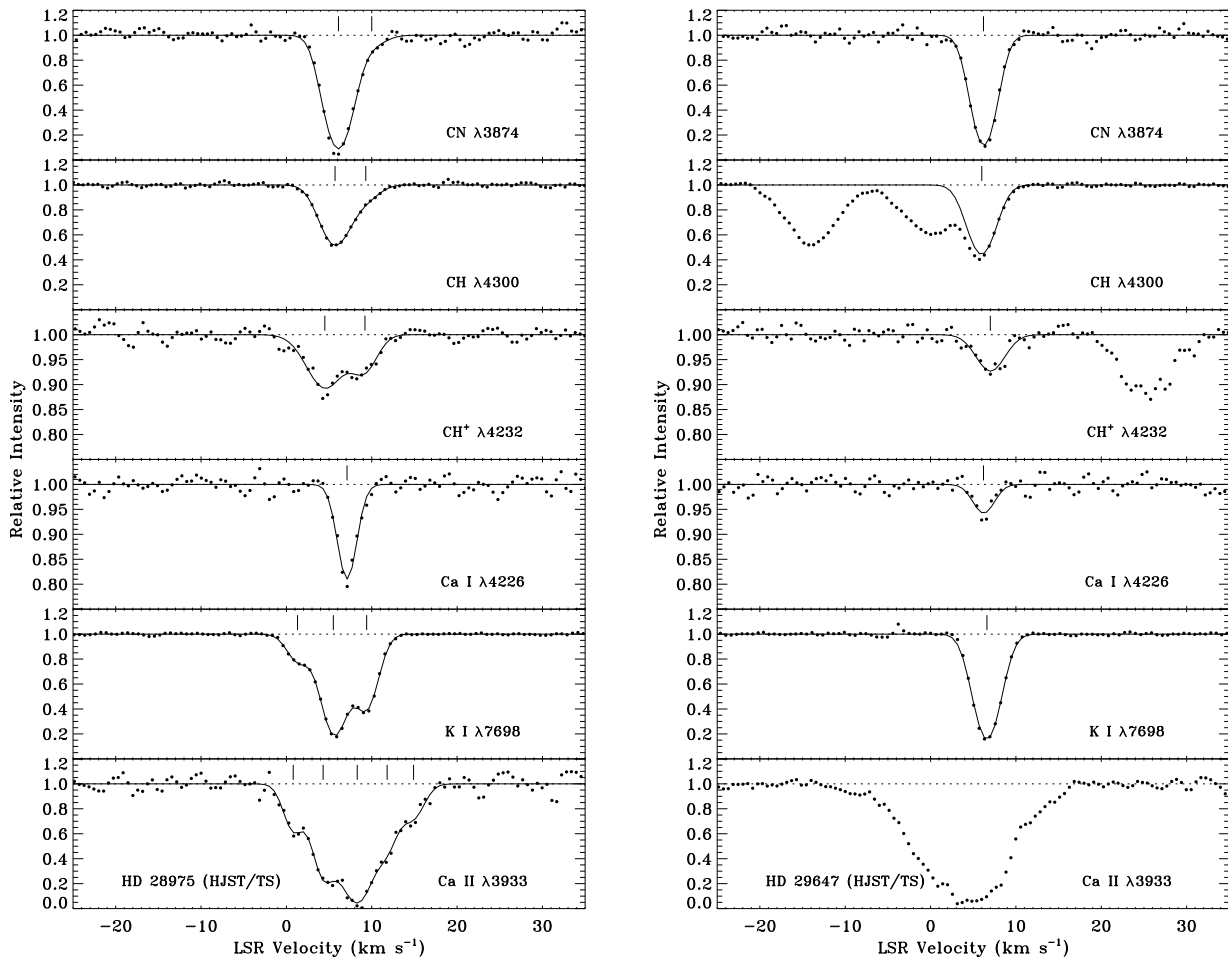


Figure 2. TS spectra of interstellar absorption toward HD 28975 (left panels) and HD 29647 (right panels) at visible wavelengths. Note that the vertical scales differ from panel to panel. Many stellar features from HD 29647 are seen, especially affecting absorption from interstellar CH and Ca II. The two stellar lines near CH are Ti II at 4300.042 Å and Mn II at 4300.254 Å. In the case for Ca II, there is no clear evidence for absorption from interstellar material. The complex profile of the Ca II feature, which resembles that of the stellar Fe II line lying near the interstellar CH⁺ line, makes it difficult to discern the presence of interstellar Ca II. The vertical tick marks above the spectra indicate the velocities for each component.

2.2. Ultraviolet and Visual Echelle Spectrograph

Archival spectra of HD 27778 and HD 29647, acquired using the Ultraviolet and Visual Echelle Spectrograph (UVES) of the Very Large Telescope (VLT), were obtained from the European Southern Observatory (ESO) Science Archive Facility. The VLT/UVES spectra of HD 29647 were acquired in 2008 August under program 081.D-0498 (PI: S. Hubrig) and cover nearly the entire visible spectrum

from 3300 to 9500 Å (with gaps between 4500 and 5700 Å and between 7500 and 7700 Å). Observations of HD 27778 were obtained in 2014 October and November under program 194.C-0833 (PI: N. Cox). These data (likewise) cover essentially the entire visible spectrum (with small gaps) from 3100 to 10400 Å (see Cox et al. 2017). In addition to providing duplicate observations of the lines already covered by the TS data (for HD 29647), the VLT/UVES spectra provide information on the NH $A-X$ (0, 0) band near 3358 Å, the CN $B-X$ (1, 0) band near 3579 Å, the CH⁺ $A-X$ (1, 0) transition at 3957 Å, the CH $B-X$ (0, 0) lines near 3886 Å, the C₃ $A-X$ (000)–(000) band near 4051 Å, and the C₂ $A-X$ (3, 0) band near 7719 Å. Severe contamination from telluric features (and stellar lines in the case of HD 29647) prevented our use of features associated with the C₃ and C₂ (3, 0) bands.

After downloading the raw science and calibration frames from the ESO archive, the VLT/UVES data were reduced using the UVES pipeline software, which corrects for the bias in the data, subtracts scattered light, finds and extracts the echelle orders, flat fields the data, applies a dispersion solution, and then merges the orders to produce a final spectrum. The optimal extraction method was adopted for data obtained with the blue arm. However, for data obtained with the red arm, for which the default reduction procedures often lead to residual fringing and rippling in the reduced spectra, the average extraction method was used and the flat fields were divided into the stellar spectra pixel by pixel (rather than after extracting the spectra as is the default approach). The extracted and merged spectra were then shifted to the LSR frame of reference and small segments of spectra surrounding interstellar lines of interest were normalized to the continuum in the same way as for the TS data discussed above. The VLT/UVES spectra are characterized by higher S/N ratios than were achieved with the TS data (by factors of 3 to 8 for HD 29647), but the UVES data were acquired at lower spectral resolution. (The blue UVES data have $R \approx 80,000$, while $R \approx 100,000$ applies to the red data.)

Additional examples of TS and UVES spectra for our targets appear in Figures 3 and 4. Figure 3 displays TS spectra for HD 30122 (left panels) and UVES spectra for HD 27778 (right panels), adopting the same format as in Fig. 2. (We note that a stellar feature affecting the Ca II profile toward HD 30122 was fitted and removed from the spectrum during the continuum normalization

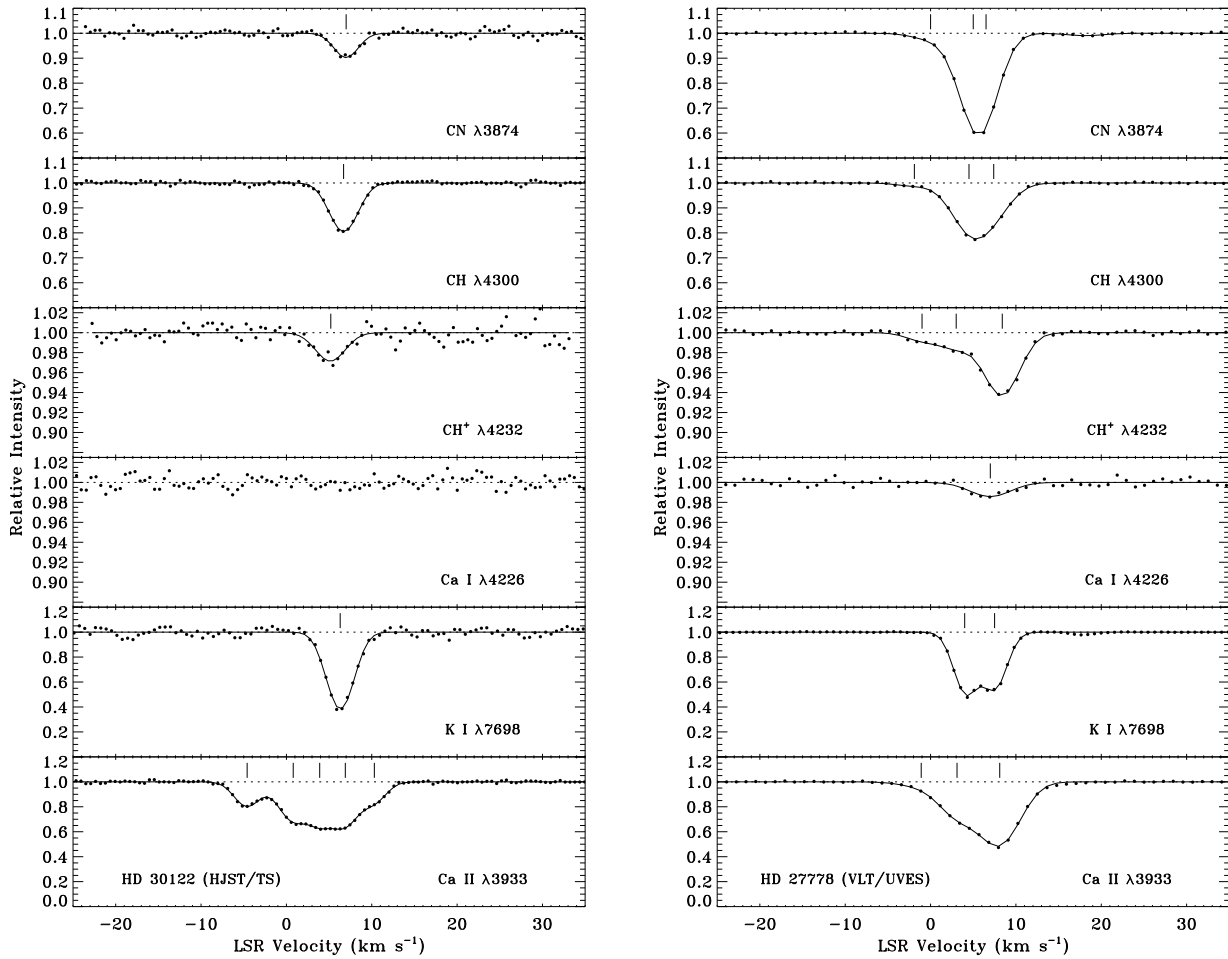


Figure 3. Interstellar absorption toward HD 30122 with TS (left panels) and toward HD 27778 with UVES (right panels) at visible wavelengths. In the spectrum for HD 30122, a broad stellar Fe II feature near the interstellar CH⁺ line was removed, as was stellar absorption from Ca II, before fitting. See Fig. 2 for additional details.

process.) The rich spectra of the C₂ A–X (2, 0) band toward HD 28975 and HD 29647 appear in Figure 4. The P-, Q-, and R-branches show detections up to $J'' = 8$ (and 10) toward HD 28975 (HD 29647). The total equivalent widths of interstellar species seen in our spectra from TS and UVES are given in Appendix A, as is a comparison with other determinations.

2.3. IGRINS

High-resolution ($R \approx 45,000$) near infrared (14,500 to 24,500 Å) spectra were obtained with the Immersion GRating Infrared Spectrometer (IGRINS; Yuk et al. 2010; Park et al. 2014). The spectrum of HD 29647 employed IGRINS on HJST at McDonald Observatory in 2016 January, while the

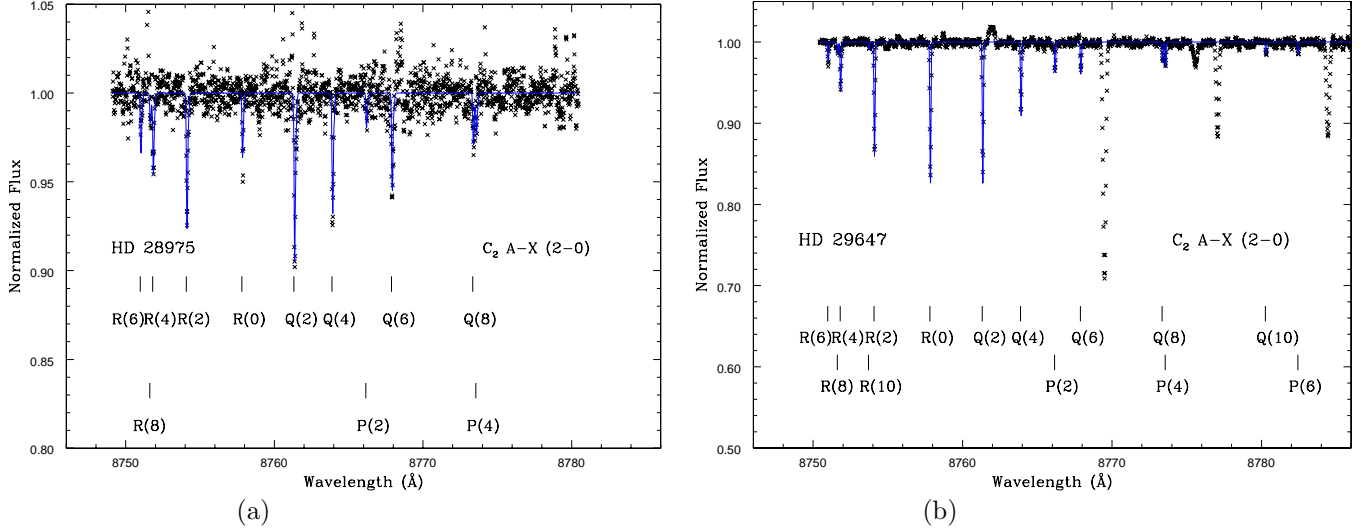


Figure 4. Absorption from the C_2 $A-X$ (2, 0) band toward HD 28975 with TS (a) and toward HD 29647 with UVES (b). The UVES spectrum for HD 29647 provides detections of the Q(10) and P(6) lines. The bump near Q(2) in plot (b) is from the residuals remaining after removing the strong Paschen line of H I at 8750 Å. The other, unidentified lines are stellar absorption from Mn II at 8769.176 and 8784.127 Å and Kr I at 8776.750 Å. Observed (x) and synthesized (blue line) spectra are presented. Details of the profile fitting are described in §3.1. Line identifications appear below the features.

spectrum of HD 28975 is from IGRINS when it was installed on the 4.3 m Lowell Discovery Telescope (LDT) in 2018 October (Mace et al. 2016, 2018). During the LDT measurements, a mechanical anomaly degraded the spectral resolution, reducing R to 35,000. On both telescopes the spectral format of IGRINS is unchanged. Targets were observed in two positions on the slit to facilitate sky subtraction, and the A0V star κ Tau was observed at a similar airmass after each science target to use for telluric correction. Spectra were extracted using the IGRINS pipeline (Lee et al. 2017)⁹, which performs flat-field correction, wavelength calibration with night sky OH emission and telluric absorption lines, and optimal extraction of the one-dimensional spectrum. Telluric absorption lines were corrected by dividing the science spectrum by the κ Tau spectrum, after the latter had been divided by the Vega model of Kurucz (1979).

⁹ <https://github.com/igrins/plp/tree/v2.1-alpha.3>

The scientific goals of our project required spectra with S/N ratio of about 500. We took care when removing the telluric lines so that residual absorption was less than 1% of the target star's continuum. This was accomplished by applying small corrections to the spectrum of k Tau. First, we made an adjustment so that the airmasses for k Tau and our targets were essentially the same; this step removed the telluric CO features in the wavelength intervals of interest to us. However, variation in the water vapor during the observations caused residuals. These were corrected by multiplying or dividing by a small power of a telluric water vapor absorption spectrum calculated from the HITRAN line list (Rothman et al. 2005) and the U.S. Standard Atmosphere, provided by JHL.

We sought absorption by interstellar CO and ^{13}CO in their 2-0 rovibrational bands, with respective R(0) lines at 2.3453 and 2.3978 μm . While the H₂ S(0) line from the 1-0 rovibrational band at 2.2232 μm may be observed in IGRINS spectra (Lacy et al. 2017), the S/N ratios obtained by us and H₂ column densities less than 10^{22} cm^{-2} toward HD 28975 and HD 29647 prevented our seeing H₂ absorption. Normalized spectra showing CO toward our two targets appear in Figure 5. We did not detect ^{13}CO absorption, but we discuss a meaningful upper limit toward HD 29647 in §4. Appendix A also provides equivalent widths from the CO spectra.

2.4. IR Photometry

We use the mid- to far-IR images publicly available to describe the environment of each line of sight. Whenever possible, we use the images with the best angular resolution: Spitzer in the mid-IR (3.6 to 24 microns from the Taurus Legacy Survey, Rebull et al. 2010), far-IR (160 microns, Flagey et al. 2009), and Herschel in the far-IR (70 to 500 microns from the Guaranteed Time Key Programme, Kirk et al. 2013). For the line of sight toward HD 30122, which lies at the very edge of the Spitzer Taurus survey, we use the WISE all-sky images instead in the mid-IR (3.4 to 22 microns, Wright et al. 2010). We also use the dust temperature map from Flagey et al. (2009) derived from Spitzer 160 and IRIS 100 microns data (Miville-Deschênes & Lagache 2005). We search for previous mentions of the background stars in the literature to support our description.

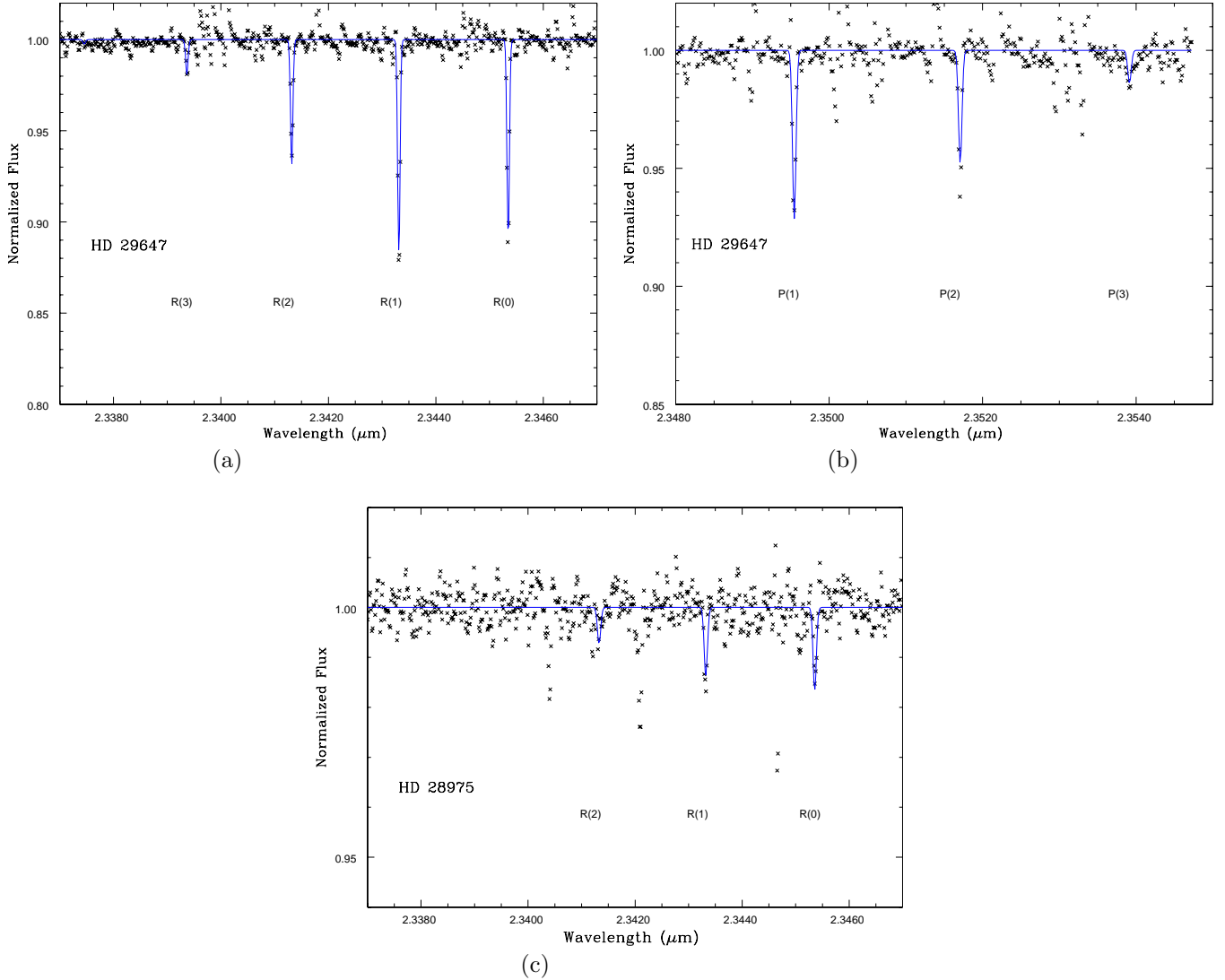


Figure 5. IGRINS spectra revealing absorption from the (a) R- and (b) P-branches of interstellar CO toward HD 29647, as well as the R-branch toward HD 28975 (c). Observed (x) and synthesized (blue line) spectra are presented. Details of the profile fitting are described in §3.1. Line identifications appear below the features.

3. RESULTS AND ANALYSIS

3.1. Profile Syntheses

We utilized modified versions of the FORTRAN program ISMOD developed by Y. Sheffer (e.g., Sheffer et al. 2008) for our profile syntheses. The program fits one or more Voigt components to an absorption profile and returns the column density $N(X)$ for species X, b -value, and velocity v_{LSR} of

each component after minimizing the root mean square in the residual spectrum. Oscillator strengths (f -values) for atomic lines were taken from Morton (2003). For the CH and CH⁺ transitions, we adopted f -values from Gredel et al. (1993). For the B - X and A - X bands of ¹²CN and ¹³CN, we used oscillator strengths from Brooke et al. (2014) and Sneden et al. (2014). The adopted f -value for the NH transition came from Fernando et al. (2018). As for the A - X (2, 0) band of C₂, the necessary data were compiled by Sonnentrucker et al. (2007), while for the (2, 0) rovibrational band of CO, they were from Black & Willner (1984). The large-scale calculations on the f -values for the C₂ A - X (2, 0) band (Kokkin et al. 2007; Schmidt & Bacskay 2007) confirm the value adopted by Sonnentrucker et al. (2007).

For many of the atomic and molecular transitions observed toward our targets, we fit each individual absorption profile separately. For HD 29647, the column densities derived independently from the various CH and CH⁺ transitions available from the UVES spectra allowed us to check the overall consistency in these column densities and compare them with those derived from the TS data. However, for some species (e.g., CN, CO, and C₂) more sophisticated profile fitting procedures were required. The R(0), R(1), and P(1) lines of the B - X (0, 0) band of ¹²CN toward HD 28975 and HD 29647 are very strong and hence are likely severely affected by optical depth effects, which makes deriving accurate column densities difficult. Since the UVES data toward HD 29647 provide access to both the (0, 0) and (1, 0) bands of the CN B - X system, we take advantage of the factor-of-10 difference in f -value for the two bands and fit the R(0) lines of the bands simultaneously to derive a single value for the column density in the $N'' = 0$ level. We then fit the R(1) and P(1) lines together to obtain a value for $N_{CN}(N = 1)$. We included fits to the corresponding ¹³CN features while synthesizing the R(0), R(1), and P(1) lines of the (0, 0) band. The R(2) and P(2) lines are weak and were fitted independently. The (1, 0) band was not covered by the TS observations (and the S/N is not nearly as good in the TS spectra as in the UVES data). We therefore fit the R(0), R(1), and P(1) lines recorded by the TS observations of HD 28975 and HD 29647 independently, but supplemented these determinations with fits to the weak CN line at 7871 Å, which is part of the A - X (2, 0) band and also probes the $N'' = 0$ level. This line was available in one of the orders from the

TS observations that provided the C_2 data. The CN lines are significantly weaker toward HD 27778 and HD 30122. Final CN column densities for these directions were derived from independent fits to the available lines. Fits to the CN lines from the $B-X$ (0, 0) band toward all four targets appear in Figure 6. The component structures derived from these and other fits to the atomic and molecular lines observed in the four directions are given in Table 2, where v_{LSR} , $N(X)$, and b -value are listed for each component.

A different approach was taken when fitting the C_2 and CO lines toward HD 28975 and HD 29647. It was a necessity for the CO lines because the data have coarser spectral resolution. The initial guesses for component structure were based on the TS and UVES results for CN. An additional constraint applied to the CO spectra was the rotational excitation temperature, $T_{0,J}(\text{CO})$. Lines associated with the same J'' in the P-, Q-, and R-branches in C_2 and in the P- and R-branches in CO (for HD 29647) provided consistency checks during the fitting process. The largest optical depth at line center approached 2 toward HD 29647. Acceptable fits were not always possible, and we had to keep some of the parameters fixed. For example, $T_{0,J}(\text{CO})$ was kept at 11.5 K toward HD 28975, with an allowed range of ± 2.5 K based on the root-mean-square outcomes. The resulting fits are provided in Figures 4 and 5. The total column densities for the two lines of sight appear in Table 3.

3.2. Rotational Excitation

Absorption from more than one rotational level in C_2 , CO, and CN was detected, allowing us to infer the physical conditions (gas density, gas temperature, and strength of the interstellar radiation field) from the amount of excitation above that due to the cosmic microwave background (CMB) at a temperature of $T_{\text{CMB}} = 2.725$ K (Fixsen 2009). According to Pan et al. (2005), the three molecules occupy similar regions along the line of sight to the background star. Because the processes leading to excitation differ, the results from C_2 , CO, and CN are complementary. In particular, C_2 excitation by atomic and molecular hydrogen and optical pumping (van Dishoeck & Black 1982) from low lying levels provides information on gas temperature and from levels greater than $J = 4$ on the ratio of gas density to strength of the infrared radiation field. Because C_2 is a homonuclear molecule, rotational transitions with ΔJ equal 1 are forbidden, unlike the cases for CO and CN. The IR radiation field

Table 2. Component Structure

Star	Ca II			K I			Ca I			CH ⁺			CH			CN		
	v_{LSR}	$N/10^{11}$	b	v_{LSR}	$N/10^{11}$	b	v_{LSR}	$N/10^{10}$	b	v_{LSR}	$N/10^{12}$	b	v_{LSR}	$N/10^{12}$	b	v_{LSR}	$N/10^{12}$	b
	(km s ⁻¹)	(cm ⁻²)	(km s ⁻¹)	(km s ⁻¹)	(cm ⁻²)	(km s ⁻¹)	(km s ⁻¹)	(cm ⁻²)	(km s ⁻¹)	(km s ⁻¹)	(cm ⁻²)	(km s ⁻¹)	(km s ⁻¹)	(cm ⁻²)	(km s ⁻¹)	(km s ⁻¹)	(cm ⁻²)	(km s ⁻¹)
HD 27778	-1.1	0.3	2.1	-1.0	0.6	0.5	-1.9	1.1	0.5	+0.0	0.5 ^a	1.6
	+3.1	2.6	1.5	+4.0	4.6	0.8	+3.0	1.2	0.9	+4.5	19.1	1.3	+5.0	8.0	1.2
	+8.1	6.9	2.0	+7.5	3.8	0.9	+7.0	0.4	2.1	+8.4	5.6	1.3	+7.4	10.5	1.2	+6.5	5.9	0.9
HD 28975	+0.8	2.5	0.6	+1.3	1.3	0.7
	+4.3	10.0	1.0	+5.5	21.2	1.0	+4.5	9.9	2.6	+5.7	50.0	1.6	+6.1	57.8	1.4
	+8.3	39.4	1.3	+9.4	7.6	0.7	+7.1	3.3	0.6	+9.2	4.4	1.5	+9.3	7.7	1.1	+10.0	1.7	1.6
	+11.8	3.7	0.9
	+14.9	1.6	1.0
HD 29647	^b	^b	^b	+6.6	29.1	1.0	+6.2	1.0	1.0	+7.0	5.2	1.9	+6.0	58.7	1.3	+6.2	86.6	1.1
HD 30122	-4.6	1.3	1.4
	+0.8	2.4	1.8
	+3.9	1.9	1.3	< 0.2	...	+5.2	2.1	2.0
	+6.9	2.4	1.5	+6.3	6.0	1.4	...	< 0.2	+6.7	15.6	1.4	+7.0	1.6	1.3
	+10.3	1.0	1.3

^aThe column density for $N = 0$ in CN was multiplied by 1.4 to account for excited rotational levels populated by the cosmic background.

^bNo attempt was made to fit the Ca II line toward HD 29647 since the line is predominantly stellar in nature.

Table 3. Column Densities for C₂ and CO Rotational Levels

Line	HD 28975	HD 29647
	C ₂ (10 ¹² cm ⁻²)	
	a	b,c
$N_{C_2}(0)$	4.9(2.0) ^d	20.8(0.6)/19.7(0.4)
$N_{C_2}(2)$	26.4(2.1)	38.9(0.6)/38.5(0.4)
$N_{C_2}(4)$	18.7(2.0)	18.0(0.6)/18.8(0.4)
$N_{C_2}(6)$	15.0(2.5)	10.3(0.7)/7.8(0.4)
$N_{C_2}(8)$	7.8(2.6)	5.8(0.7)/5.0(0.5)
$N_{C_2}(10)$/3.0(0.5)
$N_{tot}(C_2)$	72.8	93.8/92.8
	CO (10 ¹⁶ cm ⁻²)	
	e	f
$N_{CO}(0)$	3.6(1.0)	25.4(1.7)
$N_{CO}(1)$	6.7(1.8)	42.6(1.7)
$N_{CO}(2)$	4.2(1.2)	22.2(1.4)
$N_{CO}(3)$...	5.4(1.2)
$N_{CO}(4)$...	≤ 4.2 ^g
$N_{tot}(CO)$	14.5	95.6

^aLine parameters: v_{LSR} are +6.1 and +9.7 km s⁻¹; b are 1.5 and 1.6 km s⁻¹, with relative fractions of 0.85 and 0.15.

^bThe first entry provides TS results, and the second UVES.

^cLine parameters: TS - v_{LSR} is +5.8 km s⁻¹ and b is 0.9 km s⁻¹; UVES - v_{LSR} is +5.6 km s⁻¹ and b is 0.9 km s⁻¹.

^dThe uncertainties are given in parentheses.

^eLine parameters: v_{LSR} are +6.1 and +9.7 km s⁻¹; b are 1.2 and 1.6 km s⁻¹, with relative fractions of 0.85 and 0.15.

^fLine parameters: v_{LSR} is +5.4 km s⁻¹ and b is 0.5 km s⁻¹.

^gA meaningful 2- σ upper limit was possible in this case.

is assumed to have a strength comparable to that of the average interstellar radiation field, unless evidence suggests otherwise. Analysis of CO excitation (e.g., [Goldsmith 2013](#)) yields an estimate for the density of H₂, provided that the gas temperature is available from H₂ or C₂ measurements. In diffuse molecular gas, with an ionization fraction $x(e) \approx 10^{-4}$, the dominant collision partner for CN excitation is electrons ([Black & van Dishoeck 1991](#)). If the ionization fraction is known, the

resulting electron density can be converted to a total proton density, $n_{tot}(\text{H}) = n(\text{H}) + 2 n(\text{H}_2)$. In molecular clouds, where the ionization fraction is very low (i.e., $\lesssim 10^{-5}$) and gas densities are high ($\gtrsim 10^4 \text{ cm}^{-3}$), collisions involving molecular hydrogen and atomic helium begin to become important. We consider this possibility when attempting to merge the results from our analyses from a diffuse cloud perspective with the results of radio emission from CN toward HD 29647 (Crutcher 1985). Although it is common to infer the density of collision partners, $n(\text{H}) + n(\text{H}_2)$, in analyses of rotational excitation, we determine total proton densities for ease of comparison with analyses based on electron density or chemical considerations. For the molecule-rich diffuse material in our work, we assume that $n(\text{H}) = n(\text{H}_2)$. Throughout the paper, the subscript *tot* refers to *total* proton gas and hydrogen column density.

3.2.1. C_2

For C_2 excitation, the discussion in Hupe et al. (2012) forms the basis for our analysis. In particular, collisional cross sections (Lavendy et al. 1991; Robbe et al. 1992; Najjar et al. 2008, 2009) and the f -value for the $A-X$ (2, 0) band (Erman & Iwamae 1995; Kokkin et al. 2007; Schmidt & Bacskay 2007) are used. The line-of-sight column densities and their uncertainties for the gas toward HD 28975 and HD 29647 appear in Table 3. For HD 27778, the results of Sonnentrucker et al. (2007) are adopted. Results for C_2 toward HD 30122 are not available. We obtain a gas temperature, $T(\text{C}_2)$, and total proton density, $n_{tot}^{ex}(\text{C}_2)$, of 10 K and greater than $\sim 350 \text{ cm}^{-3}$ toward HD 29647. A remarkable outcome of this analysis is that only a value of 10 K for $T(\text{C}_2)$ is possible although temperatures up to 100 K were considered. For the gas toward HD 28975 and HD 27778, values of $T(\text{C}_2)$ and $n_{tot}^{ex}(\text{C}_2)$ are inferred to be 30 K/250 cm^{-3} and 50 K/150 cm^{-3} , respectively. For comparison when adopting the same cross section and f -value, the values for the gas toward HD 27778 from Sonnentrucker et al. (2007) are $50 \pm 10 \text{ K}$ and $140 \pm 20 \text{ cm}^{-3}$. As discussed below, there is evidence for a weaker interstellar radiation field penetrating the TMC; adopting a value for I_{IR} (the strength of the adopted IR radiation field relative to the interstellar value) of 0.5 in this analysis leads to a halving of $n_{tot}^{ex}(\text{C}_2)$.

3.2.2. CO

The effort by Goldsmith (2013), where the cross sections from Yang et al. (2010) are used, is the basis for our analysis of CO excitation. The analysis, however, uses a finer grid of gas temperatures (20, 40, 60, 80, 100 K) and adopts values from observations of H₂ or C₂ instead of generic ones. Once the gas temperature is specified, the CO excitation temperature determines the density of collision partners. As noted in Goldsmith (2013), collisions with H₂ dominate over those involving atomic hydrogen. We multiply this density, $n(\text{H}_2)$, by a factor to convert it to total proton density from CO excitation, $n_{tot}^{ex}(\text{CO})$. The adopted factor depends on properties revealed by our analyses. For diffuse molecular material like that toward HD 27778 and HD 30122, a factor of 3 is adopted, since $n(\text{H})$ and $n(\text{H}_2)$ are comparable. As discussed in §4.1.2, the sight line toward HD 29647 is dominated by molecular gas, while that toward HD 28975 seems to represent an intermediate case. As a result, the conversion factors used are 2 and 2.5, respectively. The excitation temperatures needed for the analysis are $T_{10}(\text{CO})$ and when available $T_{21}(\text{CO})$ and $T_{32}(\text{CO})$. Since the fitting of the CO profiles provides a different set of excitation temperatures, $T_{01}(\text{CO})$, $T_{02}(\text{CO})$, and $T_{03}(\text{CO})$, as was done in Sheffer et al. (2008) for instance, we first transformed the later set into the former ones through the use of equations (2) to (4) from Goldsmith (2013).

All four sight lines have information on CO excitation. For HD 29647 and HD 28975, the IGRINS results presented here are adopted, while for HD 27778 and HD 30122, the HST results from Sheffer et al. (2008) are used. Our fitting of the CO spectrum toward HD 29647 yielded the same values for $T_{10}(\text{CO})$, $T_{21}(\text{CO})$, and $T_{32}(\text{CO})$ of 9.5 K considering the uncertainty in each determination of 1.0 K. Crutcher (1985) obtains CO excitation temperatures of 9.2 K (+5.1 km s⁻¹) and 7.5 K (+6.5 km s⁻¹), where the LSR velocity of the component is in parentheses, from his radio observations. For $T_{10}(\text{CO})$ of 9.5 K and $T_k < 20$ K from $T(\text{C}_2)$, $n_{tot}^{ex}(\text{CO})$ of about 1800 cm⁻³ is inferred. Even higher densities are suggested from $T_{21}(\text{CO})$ and $T_{32}(\text{CO})$. A comparable total proton density is obtained for the gas toward HD 28975 when considering $T_{10}(\text{CO}) = 11.5$ K and $T(\text{C}_2) = 30$ K. The analysis of CO toward HD 27778 and HD 30122 by Sheffer et al. (2008) yielded respective values for $T_{10}(\text{CO})$

of 5.3 and 3.8 K. They also derived gas temperatures from H_2 of 51 and 61 K, from which we find values for $n_{tot}^{ex}(\text{CO})$ of 975 and 450 cm^{-3} .

The radiation temperature, T_R , obtained from the microwave data of [Crutcher \(1985\)](#), as well as from the measurements by [Heyer et al. \(1987\)](#), [van Dishoeck et al. \(1991\)](#), and [Liszt \(2008\)](#), can be used to check for consistency in the physical conditions for the direction toward HD 29647. [Crutcher \(1985\)](#) used the 36-foot NRAO telescope at Kitt Peak for the $J = 1 \rightarrow 0$ line and the 4.9 m University of Texas telescope at the Millimeter Wave Observatory for the $J = 2 \rightarrow 1$ transition. The respective beam sizes and spectral resolutions were $60''/0.52 \text{ km s}^{-1}$ and $65''/0.16 \text{ km s}^{-1}$. Emission was seen at $+5.1$ and $+6.5 \text{ km s}^{-1}$ with line widths of about 1.0 km s^{-1} in both lines. The pairs representing these radial velocities for T_R were 5.8/4.2 K and 3.6/2.0 K for $J = 1 \rightarrow 0$ and $J = 2 \rightarrow 1$, respectively. The 14 m Five College Radio Observatory telescope was used by [Heyer et al. \(1987\)](#) for their measurements of $J = 1 \rightarrow 0$ emission. These observations had a beam size of $45''$, a spectral resolution of 0.52 km s^{-1} , and a spacing of $2'$. The coarse spacing revealed a single component with T_R^* of 5.9 K at $+5.9 \text{ km s}^{-1}$ with a line width of 2.8 km s^{-1} . These results are similar to a single component at $+5.7 \text{ km s}^{-1}$ with emission weighted by T_R found by [Crutcher](#). It is worth noting that our measurements of CH, C_2 , CN, and CO show absorption at about $+6.0 \text{ km s}^{-1}$. The study by [van Dishoeck et al. \(1991\)](#) was based on data obtained with the 15 m Swedish-ESO Submillimeter Telescope for the $J = 1 \rightarrow 0$ lines and the Caltech Submillimeter Observatory for the $J = 2 \rightarrow 1$ and $J = 3 \rightarrow 2$ lines. The respective beam sizes and spectral resolutions were $44''/0.13 \text{ km s}^{-1}$, $32''/0.043 \text{ km s}^{-1}$, and $20''/0.043 \text{ km s}^{-1}$, making these the observations with the highest spatial and spectral resolutions. [van Dishoeck et al. \(1991\)](#) provided beam efficiencies so that we could convert their tabulated values for T_A^* into T_R^* for comparison with the earlier studies. Emission was seen at $+5.2$ and $+7.1 \text{ km s}^{-1}$ and had typical line widths of about 2.0 km s^{-1} . The intensities described by T_R^* were somewhat lower than the earlier measurements and those of [Liszt \(2008\)](#); they found 4.1 and 2.9 K for $J = 1 \rightarrow 0$, 2.2 and 1.6 K for $J = 2 \rightarrow 1$, and 2.2 and 1.1 K for $J = 3 \rightarrow 2$. [Liszt \(2008\)](#) used the 12 m Arizona Radio Observatory for measurements of CO $J = 1 \rightarrow 0$ emission; the beam size and spectral resolution were $65''$ and 0.13 km s^{-1} . The emission, occurring at an average velocity

of $+6.14 \text{ km s}^{-1}$ with T_R^* of 5.84 K, had a peak near $+5.0 \text{ km s}^{-1}$ and a shoulder centered around $+7.0 \text{ km s}^{-1}$; the accompanying spectrum of ^{13}CO emission clearly reveals the two components.

The excitation calculations for CO emission were carried out using the RADEX code (van der Tak et al. 2007). As with the analysis noted above, the rate coefficients for collisions with H_2 were from Yang et al. (2010). We assumed equal abundances of ortho- and para- H_2 , but the dependence on the spin state of H_2 is small for diffuse cloud temperatures, typically $\pm < 10\%$ from the average at 10 K, and much less at higher temperatures. For the $J = 1 \rightarrow 0$ CO transition, the rate coefficients for para- H_2 collisions on CO at 10(100) K are $3.3 \times 10^{-11}(3.5 \times 10^{-11}) \text{ cm}^3 \text{ s}^{-1}$, and those for ortho- H_2 on CO are $3.8 \times 10^{-11}(3.5 \times 10^{-11}) \text{ cm}^3 \text{ s}^{-1}$. An expanding spherical cloud with v proportional to radius or a plane-parallel slab are invoked to handle radiative transfer. The models are based on the large velocity gradient approximation. Optical depths approach values of 100 for $J = 1 \rightarrow 0$ and $J = 2 \rightarrow 1$ when considering column densities of 10^{18} cm^{-2} , as seen toward HD 29647.

We considered cases with T_k equal to 10 and 20 K and line widths of 2.0 km s^{-1} and sought agreement with the excitation temperatures found in our CO measurements and with the values of T_R from CO emission (Crutcher 1985; Heyer et al. 1987; van Dishoeck et al. 1991). Separate models were run with densities differing by 0.25 in the log. These densities of $n(\text{H}_2)$ were multiplied by 2 to yield total proton densities, as noted above for HD 29647. For a given density, the results from the plane-parallel slab yielded slighted higher excitation and radiation temperatures. The calculations with T_k of 20 K produced excitation temperatures larger than observed, for values of $n_{tot}^{ex}(\text{CO})$ greater than 200 cm^{-3} as found in our other analyses. Moreover, the fact that T_k needs to be 10 K confirms our results from C_2 excitation. Total proton densities of about 350 to 600 cm^{-3} best match the observations, within a factor of 2 or so of our other determinations.

We also performed calculations to predict line intensities for CO emission toward HD 28975. We considered T_k of 20 and 30 K from our C_2 analysis and line widths of 2.0 and 3.0 km s^{-1} , seeking agreement with the excitation temperatures found from the analysis of the IR spectra. A value of $1.78 \times 10^{17} \text{ cm}^{-2}$ was adopted for $N_{tot}(\text{CO})$, close to the value found from IGRINS spectra. The most consistent results using RADEX were $n_{tot}^{ex}(\text{CO})$ between 180 and 320 cm^{-3} with values of T_R about

10(7) K for the $J = 1 \rightarrow 0(2 \rightarrow 1)$ line. The plane-parallel model produced satisfactory results for T_k of 20 K. We multiply $n(\text{H}_2)$ by 2.5 to infer a total proton density of about 450 to 800 cm^{-3} for $n_{tot}^{ex}(\text{CO})$, as suggested by the discussion in §4.1.2. It is not surprising that the radiation temperatures are higher in this case in light of the higher kinetic and excitation temperatures but comparable total density. This range in $n_{tot}^{ex}(\text{CO})$ is consistent with the chemical results discussed below and within a factor of 3 or so of those from C_2 excitation.

3.2.3. CN

The degree of excitation observed in CN in diffuse molecular gas differs from the situation for C_2 and CO, the other molecules examined here. When local sources of excitation are present, the CN excitation temperature that corresponds to transitions between the $N = 0$ and $N = 1$ levels, $T_{01}(\text{CN})$, may be somewhat higher than the temperature of the CMB, and only measurements with high signal to noise are able to discern the effect of local sources. The difficulty arises because CN has a much larger dipole moment than CO; the homonuclear C_2 molecule has no dipole moment. Excitation of the $N = 2$ level from $T_{12}(\text{CN})$ is even harder to detect in diffuse gas. For typical values of the ionization fraction, electron impacts will always dominate over collisions with neutral species in populating the upper rotational levels of CN. The results on column density for rotational levels in CN that are used for the analysis of its excitation appear in Table 4; fits to the profiles are provided in Figure 6.

In our analysis of CN excitation toward stars in the Taurus region, we consider local excitation by collisions with electrons with rate coefficients from [Harrison et al. \(2013\)](#) and, for completeness, the effects of collisions from ortho and para H_2 molecules ([Kalugina & Lique 2015](#)) and neutral He atoms ([Lique et al. 2010](#)). The analysis yields the electron density that corresponds to the measured excitation temperature in cases where $T_{01}(\text{CN})$ is statistically greater than T_{CMB} . From our McDonald observations of CN absorption toward HD 29647, we find an excitation temperature of $T_{01}(\text{CN}) = 2.816 \pm 0.127$ K. If the kinetic temperature of the gas in this direction T_k equals $T(\text{C}_2)$ and $T(\text{CO})$ of ≈ 10 K, as indicated by the analyses of C_2 and CO excitation, then the small excess in the CN rotational temperature would indicate that $n(e)$ is about 0.19 cm^{-3} . For $n_{tot}(\text{H})$ of

Table 4. CN Rotational Column Densities and Excitation Temperatures

Star	v_{LSR}	$N = 0$	$N = 1$	$N = 2$	$T_{01}(\text{CN})$	$T_{12}(\text{CN})$
	(km s ⁻¹)	(10 ¹² cm ⁻²)	(10 ¹² cm ⁻²)	(10 ¹² cm ⁻²)	(K)	(K)
HD 27778 ^a	+5.6	9.46 ± 0.47	4.44 ± 0.08	...	2.934 ± 0.084	...
HD 28975	+6.1	42.02 ± 4.08	15.78 ± 0.69	...	2.617 ± 0.134	...
HD 29647 ^b	+6.2	60.36 ± 3.76	26.25 ± 1.61	...	2.816 ± 0.127	...
	+6.2	66.14 ± 3.89	26.90 ± 1.25	0.98 ± 0.08	2.722 ± 0.102	2.847 ± 0.068
HD 30122	+7.0	1.06 ± 0.11	0.48 ± 0.15	...	2.940 ± 0.448	

^aResults are based on the sum of the two main CN components; velocity listed is the column-density weighted mean velocity.

^bFirst line gives results from TS data; second line lists values derived from UVES spectra.

about 1500 cm⁻³, as suggested by the analyses of CO excitation above and CN chemistry below, the electron fraction would be $x(\text{e}) \sim 1.3 \times 10^{-4}$, similar to the value expected for low density diffuse gas. These calculations assume that the H₂ ortho-to-para ratio is that determined by the kinetic temperature, which for the gas toward HD 29647 is assumed to be 10 K. However, even if the ortho-to-para ratio were larger than this, due to turbulent dissipation, for example, the results on $n(\text{e})$ and $x(\text{e})$ would not be significantly different. Our analysis of the UVES data on CN toward HD 29647 yielded $T_{01}(\text{CN})$ of 2.722 ± 0.102 K, which is consistent with no additional excitation over that from the CMB. However, at the 2σ level, this measurement is consistent with $T_{01}(\text{CN}) < 2.926$ K, which would indicate that $n(\text{e}) < 0.45$ cm⁻³, in agreement with the McDonald result. The weighted average of the two measurements yields 2.759 ± 0.080 K for a conservative 2σ limit of 2.919 K and a limit on $x(\text{e})$ of 2.9×10^{-4} . Similarly, the CN excitation temperature that we find toward HD 28975, $T_{01}(\text{CN}) = 2.617 \pm 0.134$ K is consistent with T_{CMB} . At the 2σ level, the upper limit of $T_{01}(\text{CN})$ is 2.885 K for this sight line and yields $n(\text{e})$ less than 0.25 cm⁻³ for T_k of 30 K from C₂ excitation. The values of $n_{\text{tot}}(\text{H})$ inferred from CO excitation (1900 cm⁻³) and CN chemistry (1200 cm⁻³) suggest that $x(\text{e}) < 2.1 \times 10^{-4}$.

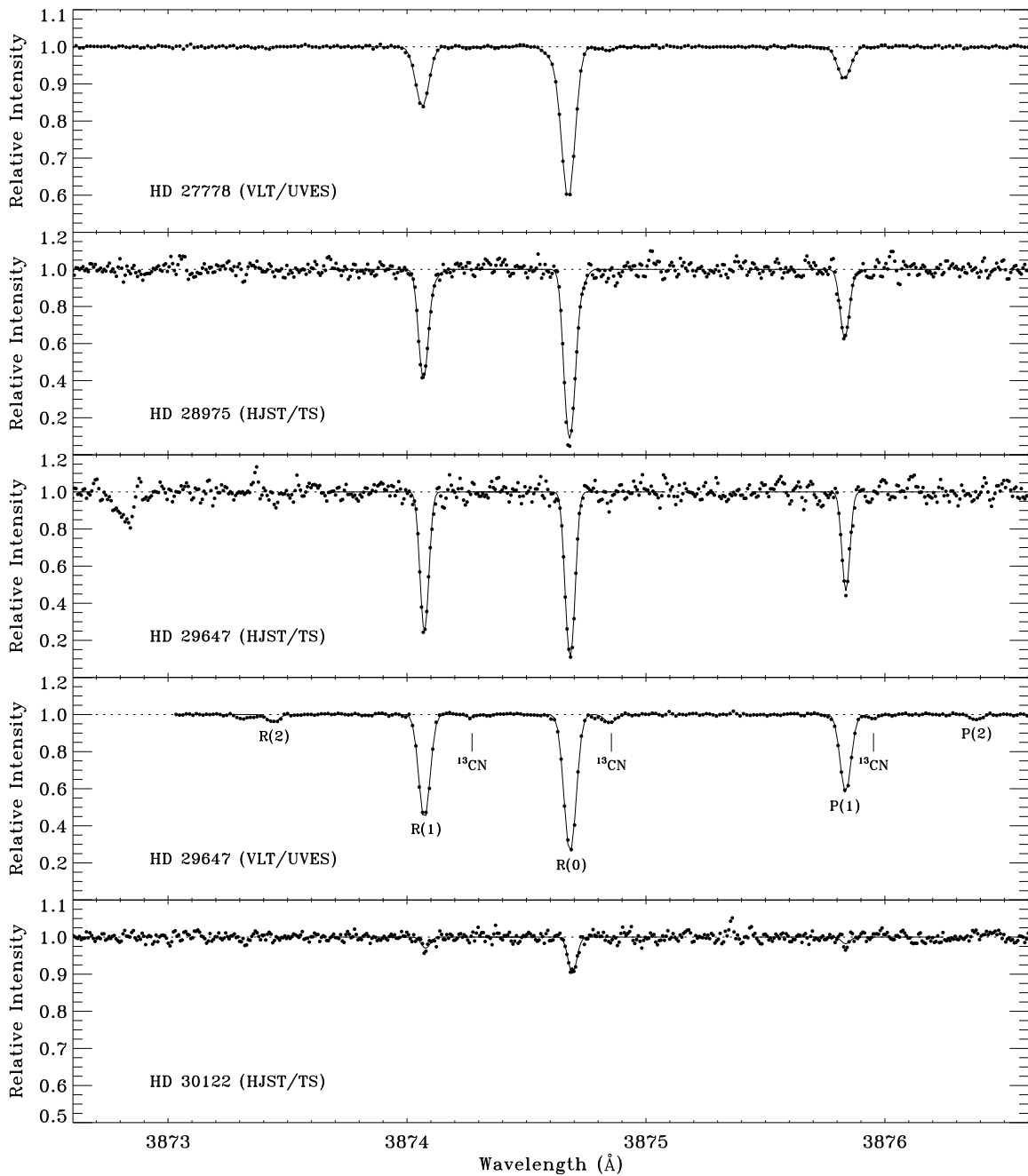


Figure 6. Profile synthesis fits to the $B-X$ (0, 0) band of CN toward HD 27778 (from UVES data), HD 28975 and HD 29647 (from TS data), HD 29647 (from UVES spectra), and HD 30122 (from TS data). The difference in resolution and S/N between the TS and UVES spectra is evident in the figure. In the panel containing the UVES spectrum of HD 29647, we include labels for the individual ^{12}CN lines, and tick marks give the expected positions of the corresponding ^{13}CN features. Solid curves show the synthetic spectra obtained through profile fitting.

We can perform the same analyses on the UVES data for HD 27778 shown in Table 4 and compare them to the results by Roth & Meyer (1995). We obtained column densities for the $N = 0$ and 1 levels of $(9.46 \pm 0.47) \times 10^{12}$ and $(4.44 \pm 0.08) \times 10^{12} \text{ cm}^{-2}$, while Roth & Meyer (1995) found values of $(10.87^{+0.74}_{-0.69}) \times 10^{12}$ and $(4.57^{+0.083}_{-0.086}) \times 10^{12} \text{ cm}^{-2}$, respectively. The two sets of results agree within about 1.2σ considering the mutual uncertainties. The corresponding values for $T_{01}(\text{CN})$ are $2.934 \pm 0.084 \text{ K}$ (present) and $2.747^{+0.096}_{-0.101} \text{ K}$ (Roth & Meyer) are consistent at the combined 1.0σ level; our determination and their 2σ limit are indistinguishable. Our CN excitation temperature suggests an electron density of 0.34 cm^{-3} when adopting a value for T_k of 50 K from H_2 and C_2 observations. With $n_{\text{tot}}(\text{H})$ of about 700 cm^{-3} from our analyses of CO excitation and CN chemistry, an ionization fraction of 4.9×10^{-4} is inferred. The weighted average of the two excitation temperatures is $2.856 \pm 0.064 \text{ K}$, indicating values for $n(e)$ and $x(e)$ of 0.21 cm^{-3} and 3.0×10^{-4} .

These values for $x(e)$ can be compared with the results for observed C^+ abundances in diffuse clouds of about 1.4×10^{-4} (Sofia et al. 1997) and the upper limit for the gas toward HD 27778 of 1.1×10^{-4} (Sofia et al. 2004); C^+ is expected to be the dominant source of electrons in this material. Further discussion with respect to the carbon budget appears in §4.1.2. The results in Table 4 for HD 30122, where the CN column density is much less but the relative uncertainties in $N_{\text{CN}}(0)$ and $N_{\text{CN}}(1)$ are greater, yield an excitation temperature that is not distinguishable from T_{CMB} .

Crutcher (1985) also detected the $(N, J, F) = (1, 3/2, 5/2) - (0, 1/2, 3/2)$ and $(1, 3/2, 3/2) - (0, 1/2, 1/2)$ lines of CN toward HD 29647 with the NRAO 36-foot telescope with a beam width of about $1'$. Each line has a velocity component at v_{LSR} of $+5.1 \text{ km s}^{-1}$ and the stronger $F = 5/2 - 3/2$ transition shows weak emission extending to about $+7 \text{ km s}^{-1}$. Thus, the component structure is similar to the ^{12}CO emission lines. According to Crutcher, the two CN lines have T_R of 0.059 and 0.042 K and line widths of 1.0 km s^{-1} . We also modeled the emission from these lines with RADEX, using the collisional data from Lique et al. (2010). These results for He were scaled by 1.37 to approximate collisions with H_2 . Like the models of ^{12}CO emission discussed above, we considered gas temperatures of 10 and 20 K, where the scaling is most likely to apply. Because CN has a larger dipole moment than CO and as a consequence a larger critical density, we only chose a line

width of 1 km s^{-1} , consistent with the observations for CN (Crutcher 1985) and CO (van Dishoeck et al. 1991). In light of the RADEX results for CO, we only considered geometries representing an expanding sphere. The models most consistent with the measurements by Crutcher (1985) suggest H_2 densities of 1000 cm^{-3} for 10 K and about 600 cm^{-3} for 20 K, corresponding to total proton densities of 2000 and 1200 cm^{-3} , respectively. We favor the 10 K results because this temperature was required to reproduce the results for C_2 and CO excitation above. This leads to comparable total proton densities for CO and CN excitation. For completeness, we note that the optical depths for the two CN emission lines are about 5 and 10 (i.e., weaker versus stronger emission) and that $T_{ex}(\text{CN})$ is about 2.8 K, like we found from the observations at visible wavelengths.

3.3. $^{13}\text{C}^{16}\text{O}$ and $^{13}\text{C}^{14}\text{N}$

Carbon monoxide is the second most abundant molecule after H_2 . As a result, it is the molecular species that contributes the greatest amount to the carbon budget. This in turn affects the relative abundances of carbon isotopologues among molecular species. For example, if the $^{12}\text{C}^{16}\text{O}/^{13}\text{C}^{16}\text{O}$ ratio is greater than the ambient $^{12}\text{C}/^{13}\text{C}$ ratio, the atomic carbon reservoir is depleted in ^{12}C (and vice versa). Thus, carbon-bearing molecules synthesized from the depleted reservoir, such as CN, are expected to show an enhancement in ^{13}C (and vice versa). Ritchey et al. (2011) provided evidence for this inverse relationship for CO and CN in diffuse molecular clouds relative to an ambient $^{12}\text{C}/^{13}\text{C}$ ratio of about 70 extracted from their sample. Two sight lines in the present study, those toward HD 27778 and HD 29647, allow us to extend this analysis.

The relative abundances of CO isotopologues are affected by two photochemical processes. (In what follows, when no isotope is given, the most abundant isotope is assumed, ^{12}C , ^{14}N , or ^{16}O .) Isotope charge exchange, $^{13}\text{C}^+ + ^{12}\text{CO} \rightarrow ^{12}\text{C}^+ + ^{13}\text{CO}$, is favored over the reverse process because ^{13}CO has a lower zero-point energy equivalent to 35 K in temperature units (Watson et al. 1976). On the other hand, isotope selective photodissociation (e.g., Bally & Langer 1982; Chu & Watson 1983; van Dishoeck & Black 1988; Visser et al. 2009) favors the more abundant isotopic variant, ^{12}CO . For carbon monoxide, photodissociation is a line process and the more abundant variant has lines that

are more optically thick, thereby shielding the CO from further photodissociation. The relative mix of the two processes determines the amount of chemical fractionation present.

The data on column densities for CO and CN isotopologues come from [Sheffer et al. \(2007\)](#) for CO toward HD 27778 and from the present study for CN. For HD 27778, the results are 67 ± 10 for $^{12}\text{CO}/^{13}\text{CO}$ and 63 ± 25 for $^{12}\text{CN}/^{13}\text{CN}$. These isotopologue ratios are indistinguishable from the ambient value of 70, suggesting that no fractionation among carbon isotopes is present along this sight line. However, in a plot of $N(^{12}\text{CO})/N(^{13}\text{CO})$ vs. $\log[N(^{12}\text{CO})]$, the data for HD 27778 lie in a region where self shielding may be occurring in both isotopologues ([Rice 2018](#)), returning the ratio to the ambient value for the atomic reservoir.

For the gas toward HD 29647, information on the $^{12}\text{CO}/^{13}\text{CO}$ and the $^{12}\text{CN}/^{13}\text{CN}$ ratios comes from our spectra. For ^{13}CO , we can set an upper limit of $1.06 \times 10^{17} \text{ cm}^{-2}$ for a ratio greater than 10. The UVES spectrum provides a $^{12}\text{CN}/^{13}\text{CN}$ ratio of 109.5 ± 9.6 . While a factor of 5 or so improvement in the IR data for the CO band is required for a definitive conclusion, it appears the ^{13}C reservoir in CO may be enhanced toward HD 29647. Because the ^{12}CO column is so large, the self-shielding factor (see [van Dishoeck & Black 1988](#); [Visser et al. 2009](#)) is much smaller than 1, the value appropriate for unshielded gas (see Fig. 13 in [Sheffer et al. \(2008\)](#) for an illustration of how the factor varies). When combined with the large amount of dust attenuation, one would not expect isotope selective photodissociation to be operating along this direction. That leaves isotope charge exchange, which can be described ([Lambert et al. 1994](#)) by

$$(^{12}\text{CO}/^{13}\text{CO}) = (^{12}\text{C}/^{13}\text{C})\exp(-35/T_k). \quad (1)$$

For $(^{12}\text{C}/^{13}\text{C})$ of 70 and T_k of 10 K, we obtain 2, much smaller than our lower limit. A likely solution to this apparent inconsistency is that isotope charge exchange is not operating either, because the C^+ abundance is very low, a consequence of the limited ionization possible with so much grain attenuation. Since there must be some C^+ along the line of sight to explain the presence of observable amounts of CH^+ (though small), as well as CH and C_2 (see next Section), C^+ must occupy a limited region where sufficient UV radiation penetrates. These points are considered further in the Discussion.

The integrated intensities for CO and ^{13}CO emission toward HD 27778 and HD 29647 are available (van Dishoeck et al. 1991; Liszt 2008). Both studies provide results for the $J = 1 \rightarrow 0$ transition. van Dishoeck et al. (1991) give ratios for each velocity component, but we consider the sum for comparison with Liszt (2008). For HD 27778, Liszt (2008) obtained an intensity ratio of 16.7, and both studies reveal a ratio of 2.8 toward HD 29647. The focus of these efforts was not on estimates for the ambient $^{12}\text{CO}/^{13}\text{CO}$ ratios, and so we can only discuss the results in general terms. It is not surprising that the ratio is much larger toward HD 27778 because $N(\text{CO})$ is a factor of 80 smaller. However, it is not clear whether the ratio of 2.8 toward HD 29647 is mainly a consequence of large optical depths or severe fractionation. At the present time, the IGRINS data only yield an $N(^{12}\text{CO})/N(^{13}\text{CO})$ ratio greater than 10.

3.4. *CN Chemistry*

The chemical network involving $\text{CH} \rightarrow \text{C}_2 \rightarrow \text{CN}$ and $\text{NH} \rightarrow \text{CN}$ is described in Federman et al. (1994) and updated in subsequent papers (e.g., Pan et al. 2001). There are two updates to the chemical model used in the current version. First, many rate coefficients have a measured temperature dependence, along with theoretical confirmation (see McElroy et al. 2013). Second, new photodissociation rates for CN are available (el-Qadi & Stancil 2013; Heays et al. 2017); we adopted the rate of $5.2 \times 10^{-10} \text{ s}^{-1}$ from Heays et al. (2017), which is about a factor of 2 larger than the rate in earlier versions. While we previously modeled the molecular material toward the four sight lines discussed in the present paper (Federman et al. 1994; Sheffer et al. 2008), revisions to $E(B - V)$ (see Table 1), CH, C_2 , and CN column densities (see Tables 2 and 3), and T_k (see §3.2.1) were made. The value for $N_{\text{tot}}(\text{C}_2)$ toward HD 27778 comes from Sonnentrucker et al. (2007) and Hupe et al. (2012). Finally, our values for $N(\text{NH})$ from UVES spectra are utilized: $2.0 \times 10^{12}/0.7 \times 10^{12} \text{ cm}^{-2}$ for the components at $+5.0/+6.5 \text{ km s}^{-1}$ toward HD 27778; and $8.0 \times 10^{12} \text{ cm}^{-2}$ toward HD29647. Changes to $E(B - V)$ lead to new values for the parameter τ_{UV} , the optical depth resulting from grain attenuation at UV wavelengths. A particularly important change is the extinction curve for HD 27778 (Fitzpatrick & Massa 2007) with its rise at short wavelengths.

Table 5. Chemical Results

Star	v_{LSR} (km s ⁻¹)	τ_{UV}	I_{UV}	T_k (K)	$N_o(\text{CH})$ (10 ¹² cm ⁻²)	$N_o(\text{NH})$ (10 ¹² cm ⁻²)	$N_o(\text{C}_2)$ (10 ¹² cm ⁻²)	$N_p(\text{C}_2)$ (10 ¹² cm ⁻²)	$N_o(\text{CN})$ (10 ¹² cm ⁻²)	$N_p(\text{CN})$ (10 ¹² cm ⁻²)	$n_{\text{tot}}(\text{Chem})$ (cm ⁻³)
HD 27778	+0.0	2.97	0.5	65	1.1	1.6	0.5	0.5	675
	+0.0	2.97	1.0	65	1.1	1.7	0.5	0.5	~1400
	+5.0	2.97	0.5	50	19.1	2.0	16.1	20.8	8.0	4.4	300
	+5.0	2.97	1.0	50	19.1	2.0	16.1	20.2	8.0	4.3	575
	+6.5	2.97	0.5	50	10.5	0.7	11.9	15.3	5.9	3.2	500
	+6.5	2.97	1.0	50	10.5	0.7	11.9	15.3	5.9	3.2	1000
HD 28975	+6.1	3.72	0.5	30	50.0	...	61.9	79.0	57.8	36.6	475
	+6.1	3.72	1.0	30	50.0	...	61.9	84.4	57.8	30.1	1200
	+10.0	3.72	0.5	30	7.7	...	10.9	7.0	1.7	1.8	150
	+10.0	3.72	1.0	30	7.7	...	10.9	7.4	1.7	2.0	325
	+10.0	3.72	0.5	50	7.7	...	10.9	6.1	1.7	1.9	175
	+10.0	3.72	1.0	50	7.7	...	10.9	6.3	1.7	2.0	375
HD 29647	+6.2	6.76	0.5	10	58.7	8.0	93.8	88.3	86.6	96.4	~1000
	+6.2	6.76	1.0	10	58.7	8.0	93.8	78.4	86.6	91.5	~1000
HD 30122	+7.0	1.43	0.5	65	15.6	15.4	1.6	1.7	275
	+7.0	1.43	1.0	65	15.6	14.8	1.6	1.6	525

We sought factor-of-two agreement between the observed and predicted column densities for C₂ and CN, and we suggest a similar level of precision for the gas densities. Our latest results appear in Table 5, where the star, the velocity component, τ_{UV} , I_{UV} (the relative enhancement of the UV radiation field over the average interstellar value), T_k , observed (o) and predicted (p) molecular column densities, and the $n_{tot}(\text{H})$ derived from the chemical model, $n_{tot}(\text{Chem})$, are listed. There are multiple components with measures of $N(\text{CN})$ toward HD 27778 and HD 28975, and calculations were performed for each. Since the velocity spread is small, we used the value for τ_{UV} for each component. Because one molecular component toward HD 28975 has much smaller column densities, we considered two gas temperatures, 30 and 50 K, for it. For the gas toward HD 27778, we previously adopted $I_{UV} = 0.5$ in light of the high Galactic latitude for the TMC (Federman et al. 1994; Sheffer et al. 2008). In their studies of the TMC, both Flagey et al. (2009) and Pineda et al. (2010) suggest that the interstellar radiation field is about 50% of the average value throughout the cloud. Making this change with the current version of the model for all four lines sight results in a gas density a factor of about 2 smaller toward HD 27778, HD 28975, and HD 30122, indicating that the C₂ and CN column densities are proportional to $n_{tot}(\text{Chem})/I_{UV}$. In other words, molecular destruction in the gas toward these stars mainly occurs through photodissociation. The difference is not necessarily 2 because any change in $N_p(\text{C}_2)$ is propagated through the CN rate equations. On the other hand, τ_{UV} is so large toward HD 29647 that photodissociation plays a limited role. Then since collisional terms dominate both production and destruction, the density terms in the numerator and denominator of the steady-state rate equations cancel. The results for this sight line in Table 5 come from the middle of the acceptable values. In general, the predictions with a reduced I_{UV} are in better agreement with observed column densities. The results for $n_{tot}(\text{Chem})$ toward HD 30122 are lower than those in Sheffer et al. (2008) because the CN photodissociation rate is larger and τ_{UV} is smaller. Overall, the values for $n_{tot}(\text{Chem})$ from the present study – 100 to 1000 cm⁻³ – are typical of CN and CO rich gas. Since the column densities are so different for the two components toward HD 28975, the gas density of 475 cm⁻³ for the one with larger $N(\text{CN})$ applies to the line-of-sight average as well. For a similar reason, the result for the +0.0 km s⁻¹ component toward HD 27778 does not affect the

average density. The results for gas density from our analyses of excitation and chemistry for each direction are discussed further in §4.3.

3.5. *Dust Temperature*

3.5.1. *HD 27778 and HD 30122*

The environments of HD 27778 and HD 30122 seem to be dominated by the diffuse interstellar medium. No bright filament is visible in the far-IR, and the mid-IR does not reveal any dark cloud either. The dust temperature map is quite homogeneous in the area surrounding both stars with values between 14.5 and 15 K. The dust temperature maps from [Flagey et al. \(2009\)](#) indicate values of 14.7 K (averaged within a 3 arcmin radius region centered on HD 27778) and 14.9 K (averaged within a 3 arcmin radius region centered on HD 30122). Figures 7 and 8 show the mid-IR and far-IR emission in the environment of the two stars. The distances to HD 27778 and HD 30122 are 224 ± 2 pc and 256 ± 4 pc, respectively, according to the *Gaia* DR2 (see Table 1), locating them both well beyond the TMC, which is about 150 pc away as discussed in more detail below.

3.5.2. *HD 28975*

The environment of HD 28975 is dominated by the presence of a dark cloud about 10 arcmin to the SE. A filamentary structure visible in the far-IR emission extends from the dark cloud south of HD 28975, though the emission levels remain low directly toward the star (see Figure 9). The presence of a nearby dark cloud might be the cause of the high $T_{ex}(\text{CO})$ found from IGRINS spectra. The dust temperature averaged within a 3 arcmin radius region centered on HD 28975 is 14.0 K, which indicates that the line of sight might be dominated by somewhat colder gas than toward HD 27778 and HD 30122. The distance to HD 28975 is 194 ± 2 pc according to the *Gaia* DR2 (Table 1), indicating this star is also well beyond the TMC.

3.5.3. *HD 29647*

The environment of HD 29647 is the most intriguing of all background stars in this paper. This star is located within the Heiles Cloud-2 (HCL-2) and was previously associated with an IRAS source (IRAS 04380+2553) by [Whittet et al. \(2004\)](#). Its distance was initially measured by *Hipparcos* at

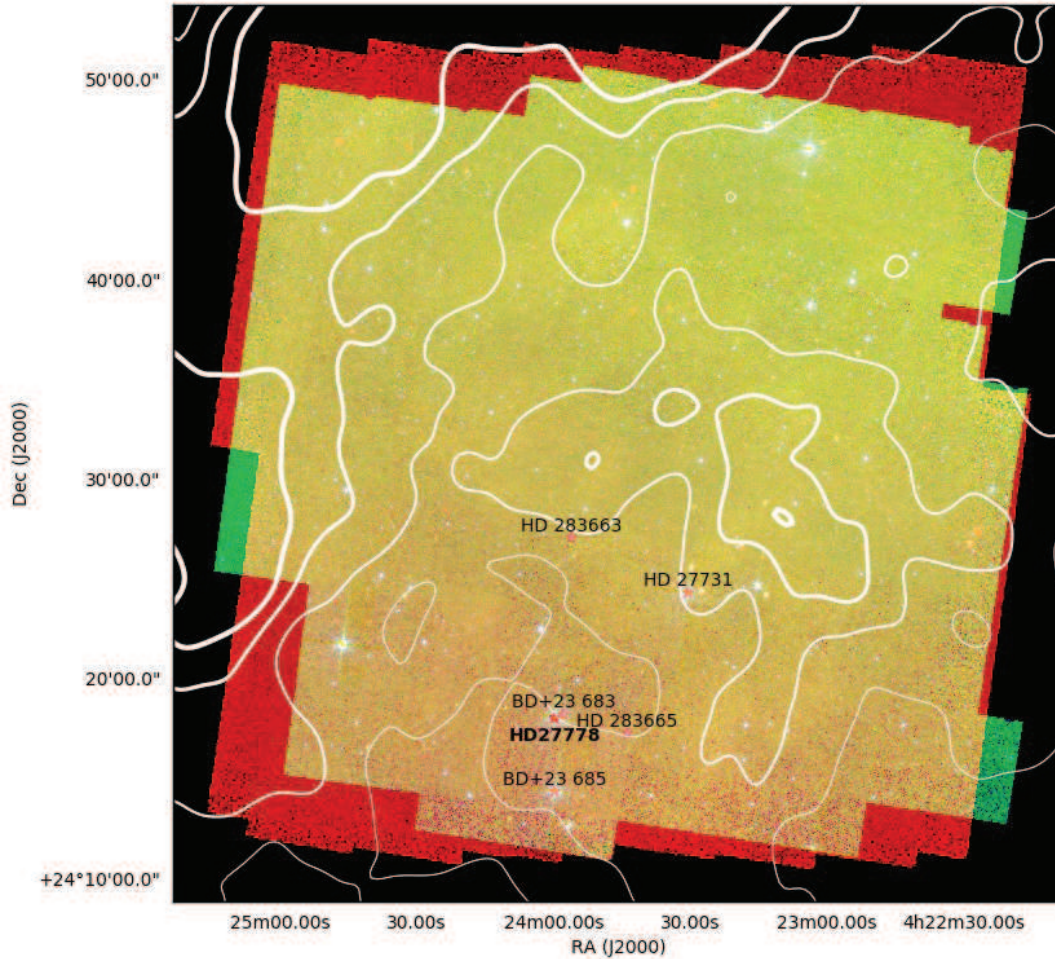


Figure 7. Three color image (blue is 4.5 microns, green is 8.0 microns, and red is 24 microns from Spitzer) of the surroundings of HD 27778. The overlaid contours are from MIPS 160 microns, smoothed by a 3-pixel wide Gaussian. Contours are increasing in thickness from 40 to 55 MJy sr⁻¹ in steps of 5 MJy sr⁻¹. The location of HD 27778 is shown by a red star. Other stars in the vicinity of HD 27778 are also shown.

about 180 pc, which would place the star a few tens of parsecs behind the TMC. Whittet et al. (2004) used extinction curves toward this star and other nearby stars as well as IRAS images to conclude that (1) HD 29647 is “embedded in or in very close proximity to dust that is being warmed, at least in part, by radiation from the star itself” and (2) it is located behind TMC-1 and half-way within a diffuse screen that contributes about 3.6 mag of visual extinction. At higher angular resolution, an infrared nebula centered on HD 29647 and 5 arcminutes in radius, is clearly detected in the mid-

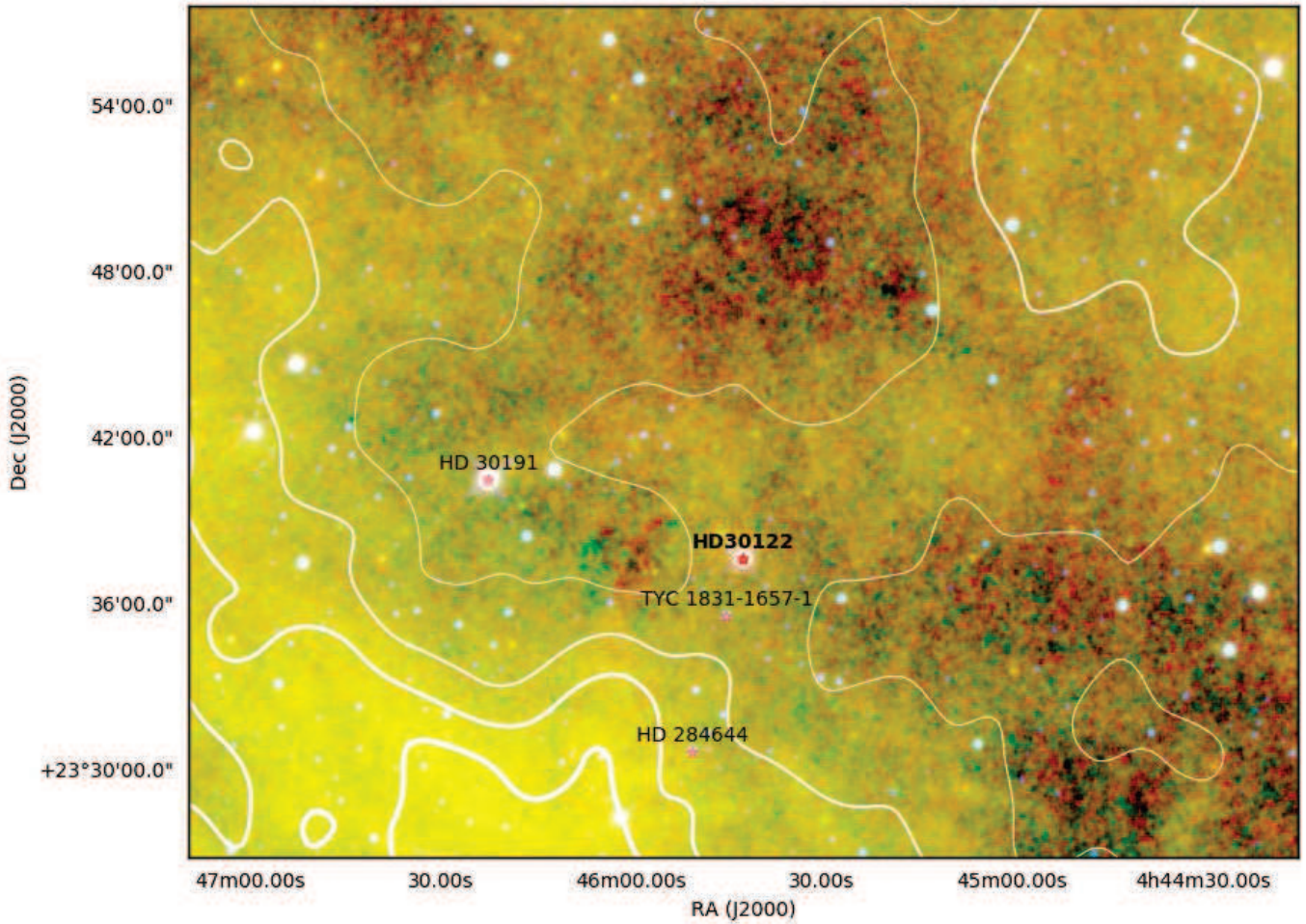


Figure 8. Three color image (blue is 4.6 microns, green is 12 microns, and red is 22 microns from WISE) of the surroundings of HD 30122. The overlaid contours are from MIPS 160 microns, smoothed by a 3-pixel wide Gaussian. Contours are increasing in thickness from 50 to 65 MJy sr^{-1} in steps of 5 MJy sr^{-1} . The location of HD 30122 is shown by a red star. Other stars in the vicinity of HD 30122 are also shown.

to far-IR (3.6 to 160 microns). The nebula is IRAS 04380+2553, and it is not detected at shorter wavelengths because visual extinction along the line of sight is so large.

In the mid-IR, two dark filaments are located to the ENE and S of HD 29647. In the far-IR (160 microns and beyond), these filaments appear in emission, as they trace cold and large dust grains. The dust temperature map of Flagey et al. (2009) tells a similar story with cold filaments surrounding a “warm spot” at the location of HD 29647. The temperature they derive toward the star is 15.4

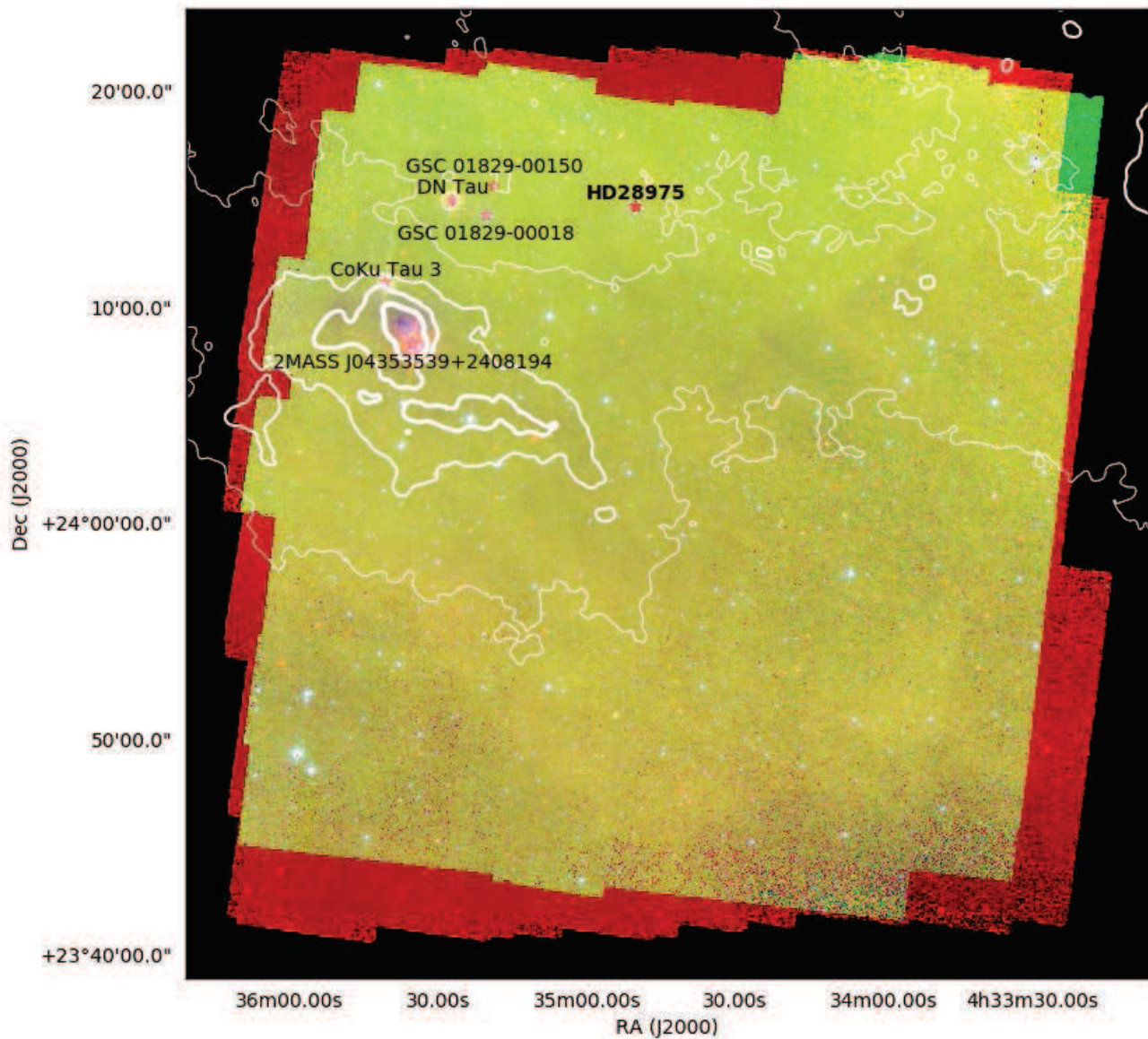


Figure 9. Three color image (blue is 4.5 microns, green is 8.0 microns, and red is 24 microns from Spitzer) of the surroundings of HD 28975. The overlaid contours are from PACS 160 microns, smoothed by a 3-pixel wide Gaussian. Contours are increasing in thickness from 40 to 160 MJy sr^{-1} in steps of 40 MJy sr^{-1} . The location of HD 28975 is shown by a red star. Other stars in the vicinity of HD 28975 are also shown.

K (averaged within a 3 arcmin radius region centered on the peak in dust temperature, 42 arcsec away from HD 29647), while it is about 13.5 K in the filaments and about 14.5 K in the surrounding diffuse medium.

Figure 10 shows a three color mid-IR image of the HD 29647 surroundings (4.5, 8.0, and 24 microns) with far-IR contours (250 microns). The infrared nebula seems to be located exactly in a “hole” delineated by the filamentary structure observed in the far-IR which, at least visually, could be an indication that the two are related, though a fortuitous alignment cannot be ruled out. We also note that the distance to HD 29647 has been revised by *Gaia* DR2 measurements and now is 155 ± 2 pc, which would put the star somewhat closer to TMC-1.

We estimate the distance between HD 29647 and the IR nebula, adopting the method used by Federman et al. (1991) based on the prescription of Draine & Salpeter (1979). In particular, the distance r to a point source whose luminosity is L and with dust temperature T_d of the cloud is given by

$$r = (LQ_\star/16\pi\sigma T_d^4 Q_{ir})^{1/2}, \quad (2)$$

where Q_\star is the effective absorption efficiency for the source spectrum, Q_{ir} is the Planck-averaged emissivity at T_d , and σ is the Stefan-Boltzmann constant. We determined Q_\star from optical properties for silicates (Draine 1985) and Q_{ir} from Draine & Lee (1984). The grain radius was taken to be 0.1 μm . Use of a spectral type of B9III Hg-Mn (Mooley et al. 2013) and T_\star of 10,550 K (Cox 2000) resulted in a value of 0.330 for Q_\star . Selecting a T_\star of 11,500 K (Mooley et al. 2013) with or without an estimate for the effect of line blanketing in this metal-rich star led to Q_\star values differing by only 15%. The adopted values for R_\star and Q_{ir} were 3.9×10^{11} cm ($5.6R_\odot$) (Cox 2000) and 2.51×10^{-4} . With T_d of 15.4 K, the estimate for the distance between HD 29647 and the TMC is about 1 pc.

The final step in this analysis is to determine the likelihood that HD 29647 lies in the diffuse gas on the far side of the TMC, as suggested by Whittet et al. (2004). We infer the extent of the diffuse gas surrounding the TMC by deriving the distance between HD 30122 and the nearby dark cloud, L1538, based on the map (Fig. 4) of Galli et al. (2019). The Galactic coordinates $[l, b]$ for HD 30122 and the cloud are $[176.62^\circ, -14.03^\circ]$ and $[175.50^\circ, -13.05^\circ]$, yielding 1.5° on the sky or 4 pc for a distance of 150 pc. If the total extent of the diffuse envelope surrounding the TMC is about twice this distance (10 pc), a gas density of about 100 cm^{-3} is obtained when the value of $N_{tot}(\text{H})$ from

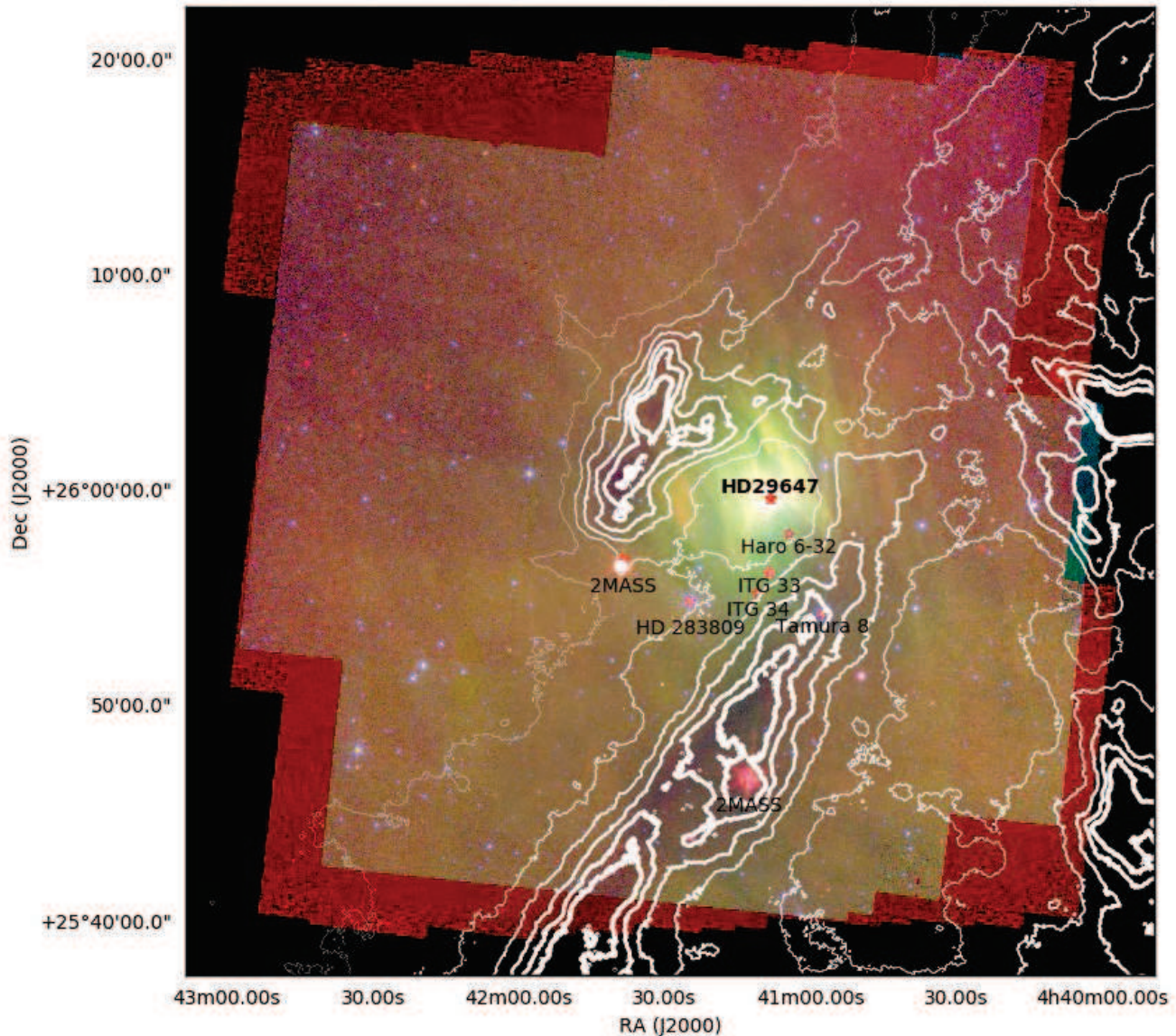


Figure 10. Three color image (blue is 4.5 microns, green is 8.0 microns, and red is 24 microns from Spitzer) of the surroundings of HD 29647. The overlaid contours are from SPIRE 250 microns. Contours are increasing in thickness from 10 to 160 MJy sr^{-1} in steps of 30 MJy sr^{-1} . The location of HD 29647 is shown by a red star, as well as for other objects, including stars in the survey by [Lacy et al. \(2017\)](#).

$N(\text{K I})$ in the direction of HD 29647 is adopted (see §4.1.1). Such a value is very typical of diffuse gas. Therefore, it appears that HD 29647 lies within the diffuse material behind the TMC.

Three groups used *Gaia* DR2 parallaxes to study the distance to the Taurus star-forming region and associated molecular material. [Yan et al. \(2019\)](#) traced the cloud in Planck 857-GHz emission

(Planck Collaboration et al. 2014), deriving a distance of 145_{-16}^{+12} pc, though they see evidence for two components. Building on the work of Schlafly et al. (2014), Zucker et al. (2019) used *Gaia* DR2 results when available and allowed R_V to vary. Their average distance was $141 \pm 2 \pm 7$ pc, where the first number gives the statistical uncertainty and the second the systematic uncertainty. Zucker et al. (2019) also subdivided the clouds in their sample, finding a bimodal distribution for Taurus – 132 and 152 pc. Using the interactive software given by Zucker et al. (2019)¹⁰, we obtain distances to the clouds in front of our stars of $\sim 162_{-4}^{+5}$ pc (HD 27778), 160_{-8}^{+6} pc (HD 28975), 123_{-8}^{+11} pc (HD 29647), and $\sim 162_{-4}^{+5}$ pc (HD 30122). The estimates for HD 27778 and HD 30122 lie somewhat beyond the region considered in this study. Last, Galli et al. (2019) used *Gaia* DR2 and VLBI techniques to obtain distances to Young Stellar Objects (YSOs) in Taurus. They divided the TMC into clusters for different dark clouds and analyzed the results through Bayesian statistics. For HD 29647 (represented by clusters called HCL-2), distances of 140.2(139.9) pc, both with uncertainties of 1.3 pc were inferred. The directions toward HD 27778 and HD 28975 (represented by a single cluster containing L1524 and L1529) had a distance of 129.0 ± 0.8 pc. It is not clear that the same material was sampled in the three studies for the directions that are our focus, and there is the possibility small-scale structure is present in the chosen regions since our analysis is based on absorption along an infinitesimal pencil beam. Still, we can infer two things of importance to our work: the TMC is about 150 pc away so that HD 29647 lies within the diffuse material on the far side of the cloud, and the other three stars are much beyond the cloud.

4. DISCUSSION

Here we explore the implications for the transition from diffuse molecular gas to dark cloud arising from our results presented in the previous section. We begin by providing an overall perspective gleaned from the results for the four directions toward HD 27778, HD 28975, HD 29647, and HD 30122, where the focus is on the presence of enhanced potassium depletion onto grains (§4.1.1), the amount of gas phase carbon in CO (§4.1.2), and the conversion of CH into other molecular species,

¹⁰ https://dataverse.harvard.edu/dataverse/cloud_distances

including CO (§4.1.3). This is followed by a discussion of a number of characteristics distinguishing the line of sight to HD 29647 in §4.2 and a comparison of the material toward the four stars in §4.3. §4.4 places our results into context with the findings from large-scale studies of the TMC (§4.4.1) and from efforts with a focus on specific regions in this molecular cloud (§4.4.2).

4.1. Overall Perspective for the Four Directions in Taurus

4.1.1. Potassium Depletion

The total number of protons, $N_{tot}(\text{H}) = [N(\text{H I}) + 2N(\text{H}_2)]$, along a line of sight is directly obtained from UV observations of H I and H₂ absorption. Of the four sight lines in our study, only that toward HD 27778 has such a determination. From the numerous measurements on diffuse molecular clouds, two other methods yield values of $N_{tot}(\text{H})$. The first uses $E(B - V)$ from [Bohlin et al. \(1978\)](#), $\langle N_{tot}(\text{H})/E(B - V) \rangle = 5.8 \times 10^{21} \text{ cm}^{-2} \text{ mag}^{-1}$. The second method is based on the column density of neutral potassium, $N(\text{K I})$, from [Welty & Hobbs \(2001\)](#). Welty & Hobbs found linear relationships between $\log[N(\text{K I})]$ and $\log[N_{tot}(\text{H})]$; we adopted the one that included all high-resolution measurements and the most reliable medium-resolution ones – $\log[N(\text{K I})] = -27.21 \pm 2.79 + (1.84 \pm 0.13)\log[N_{tot}(\text{H})]$. Toward HD 27778, the measured value for $N_{tot}(\text{H})$ is $2.3 \times 10^{21} \text{ cm}^{-2}$ ([Ritchey et al. 2018](#)); see also [Cartledge et al. \(2001, 2004\)](#). Using $E(B - V)$ from Table 1 and the total $N(\text{K I})$ from our analysis of the UVES spectrum, we obtain values for $N_{tot}(\text{H})$ of 2.1×10^{21} and $1.9 \times 10^{21} \text{ cm}^{-2}$ respectively, within 20% of the UV results.

Therefore, we apply the two methods to the data for HD 30122, HD 28975, and HD 29647. For the gas toward HD 30122, we obtain $1.3 \times 10^{21}/1.6 \times 10^{21} \text{ cm}^{-2}$ from $E(B - V)/N(\text{K I})$, while for HD 28975 we find values of $3.5 \times 10^{21}/3.7 \times 10^{21} \text{ cm}^{-2}$ respectively. The consistency found for the material toward HD 27778, HD 30122, and HD 28975 is not evident when applying the methods for the line of sight toward HD 29647, $6.3 \times 10^{21}/3.6 \times 10^{21} \text{ cm}^{-2}$. Although there are numerous stellar features near the weak K I doublet at 4044 and 4047 Å in the UVES spectrum of HD 29647, we were able to measure $N(\text{K I})$ from the optically thin line at 4047 Å, obtaining a value of $(2.6 \pm 0.6) \times 10^{12} \text{ cm}^{-2}$. This value agrees with the one obtained from our fit of the line at 7698 Å, and so it appears

the amount of depletion onto grains is enhanced by about a factor of two for potassium toward this star.

We can also estimate the extent of the molecular material along the four sight lines. For the very molecule-rich directions toward HD 28975 and HD 29647, we consider the total proton column densities discussed here, while for the diffuse molecular gas toward HD 27778 and HD 30122 we adopt the molecular hydrogen column densities from [Rachford et al. \(2002\)](#) and [Sheffer et al. \(2008\)](#), respectively. When dividing these column densities by the gas densities found from CO excitation and CN chemistry, we find that the molecular portions of the TMC in these directions is approximately 1 pc, varying by only 50%.

4.1.2. *The Amount of Carbon in CO*

Using absorption from the C II intercombination line at 2325 Å, [Sofia et al. \(1997\)](#) determined that the gas phase carbon abundance in diffuse clouds is 1.4×10^{-4} . Since C⁺ is the main source for the electron fraction in diffuse material, our limits and values for $x(e)$ from CN excitation (§3.2.3) suggest higher precision CN measurements are needed to place constraints on C⁺ for the carbon budget. However, with the CO column density ranging from 10^{15} to 10^{18} cm⁻² for the four directions in the present study, we can compare the CO contribution to the carbon budget. We adopt the values of $N_{tot}(H)$ discussed in the previous section – 2.3×10^{21} cm⁻² (HD 27778) from observations as well as 1.3×10^{21} (HD 30122), 3.5×10^{21} (HD 28975), and 6.3×10^{21} (HD 29647) cm⁻² from $E(B - V)$. Besides singly-ionized carbon and CO, another significant contribution to the carbon budget comes from neutral carbon.

For HD 27778, [Sofia et al. \(2004\)](#) obtained an upper limit of 1.1×10^{-4} for the fractional abundance of C⁺, $x(C^+) = n(C^+)/n_{tot}(H)$. Though cruder, we can look at the estimate used in our chemical model to track the conversion of C⁺ into CO ([Federman et al. 1994](#)), $\alpha = [1 + 14 \times (\tau_{UV} - 2)/5]$, where α is the percentage of C⁺ remaining. For this direction, α is 0.27, or $x(C^+)$ is 3.8×10^{-5} , comfortably below the upper limit of [Sofia et al. \(2004\)](#). Moreover, [Burgh et al. \(2010\)](#) quote $\log[N(C\ I)]$ of 15.06, or $x(C)$ at least 5.0×10^{-7} , and [Sheffer et al. \(2008\)](#) give $\log[N(CO)] = 16.09$, or $x(CO)$ of 5.4×10^{-6} .

For this sight line only about 4% of the gas phase carbon in diffuse gas is in CO; it is not clear where the missing carbon resides.

Because [Jenkins & Tripp \(2011\)](#) were not able to measure the amount of C I toward HD 30122, a result of severe blending from stellar features, the other three directions in our sample only have information on CO (and the crude measure for C⁺ from α). We start with the gas toward HD 30122, where τ_{UV} indicates no conversion of C⁺. Using the results of [Sheffer et al. \(2008\)](#), $N(\text{CO})$ of $7.04 \times 10^{14} \text{ cm}^{-2}$, we infer a CO abundance of 5.4×10^{-7} relative to $N_{\text{tot}}(\text{H})$. Here, too, essentially all of the carbon is in C⁺. Turning to the sight line to HD 28975, $N(\text{CO})$ is $1.45 \times 10^{17} \text{ cm}^{-2}$ and $x(\text{CO})$ is 4.1×10^{-5} , or about 30% of the available carbon. With a value for α of 0.17, about 50% of the carbon appears to be in neutral carbon. For the gas toward HD 29647, $N(\text{CO})$ is $9.56 \times 10^{17} \text{ cm}^{-2}$, or $x(\text{CO}) = 1.5 \times 10^{-4}$; all of the interstellar carbon appears to be in the form of CO. Because τ_{UV} is so large, α is only 0.07 and little of the carbon could be in C⁺. This is consistent with our conclusions reached through CO fractionation that C⁺ is only present in the outer portion of the cloud, where the species CH⁺, CH, and C₂ reside. Moreover, [Whittet et al. \(1989\)](#) found an upper limit for the CO column of $5 \times 10^{16} \text{ cm}^{-2}$ in solid form, or 5% of the gas phase abundance. Therefore, it seems that the line of sight toward HD 29647 probes the dark molecular TMC, with a gas temperature cold enough (10 K) to form solid CO but has not yet shown any evidence for it. With a temperature of 30 K, the material toward HD 28975 is too warm for CO depletion onto grains.

4.1.3. CO versus CH

[Sheffer et al. \(2008\)](#) sought relationships among observed quantities in their CO survey. Of particular interest for the present study is the correspondence between column densities of CO and CH for $N(\text{CO}) > 10^{13} \text{ cm}^{-2}$, which they represented as

$$\log[N(\text{CO})] = -(22.3 \pm 11.3) + (2.80 \pm 0.85)\log[N(\text{CH})]. \quad (3)$$

Adopting our results for $N(\text{CH})$, the predicted values for $N(\text{CO})$ toward HD 27778, HD 30122, HD 28975, and HD 29647 are 2.6×10^{15} , 4.4×10^{14} , 1.14×10^{16} , and $1.79 \times 10^{16} \text{ cm}^{-2}$, respectively.

The observed CO column densities are 1.23×10^{16} and 7.04×10^{14} cm^{-2} for the material toward HD 27778 (Sheffer et al. 2007) and HD 30122 (Sheffer et al. 2008); Table 3 provides the column densities for the other two sight lines. We first focus on the sight lines toward HD 27778 and HD 30122. The observed values for $N(\text{CO})$ are 4.7 and 1.6 times larger, respectively, than the values inferred from the relationship above. Looking at Fig. 9 from Sheffer et al. (2008), a plot of $\log[N(\text{CO})]$ vs. $\log[N(\text{CH})]$, the data point for HD 27778 lies near the left upper boundary of the sample, while the data point for HD 30122 is in the middle of the sample. This indicates that the material toward these two stars is representative of diffuse molecular gas and that the gas density is higher toward HD 27778 [as inferred from Fig. 17 in Sheffer et al. (2008)]. This is borne out by our analyses of molecular excitation and CN chemistry.

The differences between observed and predicted $N(\text{CO})$ are greater for the gas toward HD 28975 and HD 29647, with ratios of 13 and 53. The data points for both directions lie beyond the upper boundary shown in Fig. 9 of Sheffer et al. (2008). The data point for HD 28975 would appear approximately near the point for HD 200775, the illuminating source for the reflection nebula NGC 7023. That for HD 29647 would appear about a dex higher, with a CO column density similar to that for a dark cloud [see Fig. 6b in Sheffer et al. (2008)]. We note point $[N(\text{CO}), N(\text{H}_2)]$ for HD 200775 in Fig. 6b of Sheffer et al. (2008) is within the boundary represented by dark clouds. However, the cause for these outliers differs. In NGC 7023, the enhanced flux of UV radiation from HD 200775 preferentially destroys CH relative to CO (and H_2), a consequence of the protection arising from CO (and H_2) self shielding. Since there is no evidence for an enhancement in UV flux in its sight line, the extreme case of HD 29647 is likely the result of converting CH molecules into other molecules, including CO. In a study of CH emission from molecular clouds, Mattila (1986) found the CH column density leveled off in a plot $N(\text{CH})$ versus A_B , consistent with the chemical model of Boland & de Jong (1984) that suggested a value of about 2×10^{13} cm^{-2} . In their study of HCL-2 at 3.8 arcmin resolution, Sakai et al. (2012) found CH column densities falling below the relationship between CH and H_2 from Sheffer et al. (2008). The position of TMC-1(NH_3), which is closest to the sight line toward HD 29647, has a line width about 1.4 km s^{-1} (or b -value of 0.8 km s^{-1} , similar to our observations)

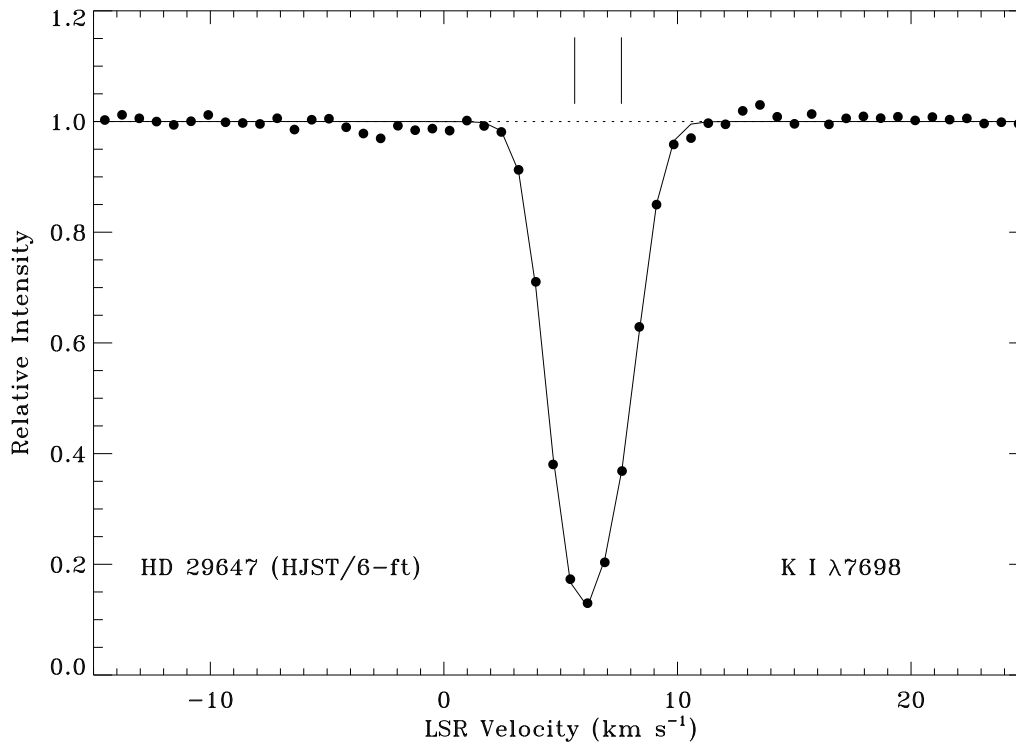


Figure 11. High-resolution spectrum of K I absorption toward HD 29647 from previously unpublished data acquired with the coude 6 foot camera on HJST. Our profile synthesis fit (solid line) indicates two velocity components at +5.6 and +7.6 km s⁻¹ (tick marks).

and $N(\text{CH})$ of $1.79 \times 10^{14} \text{ cm}^{-2}$. This column density is three times larger than what we infer, but their measurements sample the full extent of the cloud. Moreover, subsequent work by Magnani and colleagues (e.g., Magnani & Onello 1995; Magnani et al. 1998, 2003) presented evidence that CH emission was a reliable tracer of H₂ in the diffuse envelopes of dark clouds. In light of our results for HD 29647, we believe that this star probes the outer predominantly molecular portion of the TMC, although it is embedded in the diffuse molecular material on the far side of the cloud (Whittet et al. 2004, §3.5). This is described in more detail in the next section. As for the portion of the TMC in front of HD 28975, we consider it a diffuse molecular cloud because only about 30% of the available carbon is in the form of CO.

Because Welty & Hobbs (2001) concluded that there is a close correspondence between K I and CH, we look at this for our lines of sight. In particular, Welty & Hobbs (2001) find a $N(\text{K I})/N(\text{CH})$

ratio of 0.043 for their sample. The ratios for gas toward HD 27778, HD 28975, HD 29647, and HD 30122 are 0.027, 0.052, 0.050, and 0.040. Though the ratio toward HD 27778 is somewhat lower than the others, all four ratios are within about 20% of the mean value given by Welty & Hobbs (2001). In light of our findings for K I and CH toward HD 29647, we examine why the ratio does not differ, although evidence exists for smaller relative amounts of these two species, by considering the highest resolution spectra for K I from our previously unpublished data acquired with the coudé 6 foot camera on HJST. There is a hint of an asymmetry in the profile (see Fig. 11). Fitting it with two velocity components yields velocities of +5.6 and +7.6 km s⁻¹, *b*-values of 0.72 and 0.48 km s⁻¹, and relative fractions of 0.88 and 0.12 (yielding a total column of 2.58×10^{12} cm⁻², much like the column from our most recent spectrum from HJST). The component velocities are similar to those found for CO emission [+5.1 and +6.5 km s⁻¹ – Crutcher (1985); +5.2 and +7.1 km s⁻¹ – van Dishoeck et al. (1991); +5.4 and +6.7 km s⁻¹ – our estimate from the ¹³CO spectrum in Liszt (2008)]. The Full Widths at Half Maximum of the emission lines are about 1 km s⁻¹ (Crutcher 1985), equivalent to *b*-values of about 0.6 km s⁻¹. The redder component in the ¹³CO spectra of Crutcher (1985) and Liszt (2008) is narrower, much like we infer from fitting the spectrum in Fig. 11. Since Crutcher only detected HCO⁺, HCN, and CN emission from the bluer component (with weaker wings in HCO⁺ and CN), Messinger et al. (1997) inferred that a dense clump with v_{LSR} of +5.1 km s⁻¹ was present toward this star. We suggest the presence of the dense clump results in lower column densities for both K I and CH in this direction, and the relationship between these species in diffuse gas found by Welty & Hobbs (2001) maintains their relative abundances.

4.2. *HD 29647 – A Line of Sight Revealing the Transition from Diffuse Molecular to Dark Molecular Cloud*

Our results for the sight line toward HD 29647 differ significantly from those of molecule rich diffuse clouds like the material toward HD 27778. The most obvious one is $N(\text{CO})$, where the value is about 100 times greater toward HD 29647. There are a number of checks we can perform to verify our results. The maximum optical depth at line center from the fitting of the IGRINS spectrum is a modest 1.7. This optical depth arises from the required consistency when fitting the R(1)/P(1) and

R(2)/P(2) pairs of lines. The inferred b -value from the fit is 0.5 km s^{-1} . [Lacy et al. \(2017\)](#) examined the amount of CO absorption with IGRINS for targets in the vicinity of HD 29647, obtaining column densities via a curve-of-growth analysis. A comparison of the results with ours for HD 29647 appears in Table 6. The focus of the comparison is on stars within 30 arcminutes of HD 29647, corresponding to a separation of 1.3 pc at 150 pc. The results for $N(\text{CO})$, $T_{ex}(\text{CO})$, v_{LSR} , and b -value are very similar, indicating the material within about a 1 pc of the direction toward HD 29647 is relatively homogeneous. We note that HD 283809 and Tamura 8 lie beyond the IR nebula illuminated by HD 29647, and that the larger CO column toward Tamura 8 might arise from its probing one of the filaments mentioned above (see Fig. 10).

Table 6. CO Results for Embedded and Background Stars Near HD 29647

Star	R. A. (2000) ^a (<i>h:m:s</i>)	DEC (2000) ^a (<i>°:′:″</i>)	Distance ^b (pc)	$N(\text{CO})$ (10^{18} cm^{-2})	T_{ex} (K)	v_{LSR} (km s^{-1})	b -value (km s^{-1})
Elias 3-16	04:39:39	+26:11:27	275(58)	2.6	9.8	6.8	0.49
Elias 3-18	04:39:56	+25:45:02	149(5)	0.86	10.0	6.4	0.33:
Tamura 8	04:40:57	+25:54:14	...	2.5	9.5	6.4	0.61
HD 283809	04:41:25	+25:54:48	326(10)	1.3	8.4	6.0	0.41
Kim 1-59	04:41:30	+25:27:03	752(130) ^d	1.1	10.0	6.4	1.5
HD 29647	04:41:08	+25:59:34	155(2)	1.0	9.5	5.4	0.53

^aSIMBAD – [Wenger et al. 2000](#).

^b*Gaia* DR2 – [Bailer-Jones et al. 2018](#).

^cNumbers in parentheses are uncertainties.

^dSource offset in *Gaia* DR2 catalog unusually large.

Other differences involving the gas toward HD 29647 are the enhanced K depletion onto grains and the much lower predicted CO column density from our measured value for $N(\text{CH})$ from the relationship given by [Sheffer et al. \(2008\)](#). [Pan et al. \(2005\)](#) discussed the possibility of K depletion

in terms of similarities derived from profile synthesis to the parameters extracted from Ca I features. While the same applies here (see Table 2), we focused on the lower $N_{tot}(\text{H})$ inferred from $N(\text{K I})$ using the correspondence found by [Welty & Hobbs \(2001\)](#). We deduce from our analyses on $N(\text{K I})$ and $N(\text{CH})$ that the absorption from these species is restricted to the portion of the line of sight sampling typical diffuse molecular gas, while most of the CO (and CN) absorption arises from a denser clump of material in the picture developed by [Whittet et al. \(2004\)](#). Further evidence for this scenario comes from the detection of solid H_2O in the form of an ice mantle toward HD 29647 ([Smith et al. 1993](#); [Teixeira & Emerson 1999](#)). Clearly, HD 29647 probes material in a dark cloud, albeit over only about 4 mag of visual extinction.

We end the section with a comparison of results from analyses by others, mainly based on the material presented by [Crutcher \(1985\)](#). In what follows, we have not tried to adopt a common set of input parameters, and so factors of two agreement are considered satisfactory. We begin by summarizing the relevant findings of [Crutcher \(1985\)](#). He provided estimates for gas density [$n(\text{H}_2)$], T_k , and $x(\text{e})$ in the gas toward HD 29647. From a Large Velocity Gradient (LVG) model of the emission from CO and its isotopologues, he obtained a combined value for $N(\text{CO})$ in the two components of $4.8 \times 10^{17} \text{ cm}^{-2}$, within a factor of two of ours. The H_2 density and T_k inferred from the model were 800 cm^{-3} and 10 K; these agree very well with our results taking into account that we adopted a correspondence, $n_{tot}(\text{H}) = 2n(\text{H}_2)$. From HCO^+ emission and the ionization balance of K, he preferred the result for $x(\text{e})$ of $2 \times 10^{-7} \delta_{\text{K}}^{-1}$, where δ_{K}^{-1} is the enhancement in K depletion over the average interstellar value. Since we find a factor of about 2 for this enhancement (see §4.1.1), his estimate for $x(\text{e})$ becomes 10^{-7} , supporting our conclusion that CO is the dominant constituent of the carbon budget. Another effort based on analyzing excitation of CO emission lines is that of [van Dishoeck et al. \(1991\)](#). The radiative transfer through a uniform spherical cloud was determined via the mean escape probability, though other models were examined as well. The focus was on reproducing observed line intensity ratios, $^{12}\text{CO}(1-0)/(3-2)$, $^{12}\text{CO}(2-1)/(3-2)$, and $^{12}\text{CO}(3-2)/^{13}\text{CO}(1-0)$ in light of results on C_2 excitation. We converted their densities of collision partners into total gas densities by multiplying the C_2 results by a factor of 1.5 and those for CO by

a factor of 2 (H_2 excitation dominates) in what follows. Of the three ratios, the one most consistent with the C_2 results for HD 29647 (as well as for most other directions in their survey) was the $^{12}\text{CO}(3-2)/^{13}\text{CO}(1-0)$ ratio: $525_{-150}^{+450} \text{ cm}^{-3}$ versus a preferred value of 1000 (with a range 400 to 2000) cm^{-3} . These are also consistent with the present results.

Two modeling efforts (Nercessian et al. 1988; van Dishoeck & Black 1989) studied the chemistry of the gas in the $+5.1 \text{ km s}^{-1}$ component toward HD 29647. It is important to note that both efforts incorporated CO self shielding in their model clouds. Nercessian et al. (1988) adopted the gas density and temperatures from Crutcher (1985) allowing elemental depletions and the cosmic ray ionization rate to vary, while van Dishoeck & Black (1989) provided the best-fitting model described in their earlier work (van Dishoeck & Black 1988). A density of 1000 cm^{-3} and temperature of 15 K were adopted by van Dishoeck & Black (1989). For $N(\text{C}_2)$, van Dishoeck & Black (1989) used the measurements of Hobbs et al. (1983). There is generally quite good agreement between available observations and predictions for the molecular species in our survey (CH, C_2 , CN, and CO). However, our column densities tend to be smaller than those quoted earlier, in large part because there is less confusion with stellar features in our spectra, except for CO where it is a factor of nearly 3 larger. The prediction by van Dishoeck & Black (1989) for $N(\text{CN})$ is much closer to ours. For this set of species, the model predictions are within a factor of 2 to 3 of the column densities presented here. Our measurements add NH to the mix for comparison; the NH column of $8.0 \times 10^{12} \text{ cm}^{-2}$ is not consistent with either model. The electron abundance given in Nercessian et al. (1988) is consistent with our findings. With the advancements in astrochemistry since these efforts and our more precise results, it might be worthwhile revisiting the cloud toward HD 29647.

4.3. *A Comparison of the Four Directions*

We describe our results for the other three directions in light of these findings for HD 29647. They appear in Table 7, separated into two classes. There are the more typical diffuse molecular clouds toward HD 27778 and HD 30122 grouped at the bottom, and dark molecular cloud toward HD 29647 along with the intermediate case for the material toward HD 28975 at the top. The main thing to note is the range in $N(\text{CO})$, over a factor of 1000. In order to investigate the cause for this large

Table 7. Summary of Results

Star	$N(\text{CO})$ (10^{15} cm^{-2})	$^{12}\text{CO}/^{13}\text{CO}$	$T(\text{H}_2)$ (K)	$T_{01}(\text{CO})$ (K)	$T(\text{C}_2)$ (K)	$n_{tot}^{ex}(\text{CO})$ (cm^{-3})	$n_{tot}(\text{Chem})^a$ (cm^{-3})	$n_{tot}^{ex}(\text{C}_2)^a$ (cm^{-3})
HD 29647	956.	> 9	...	9.5	10	1800	$\sim 1000/\sim 1000$	$\geq 175/\geq 350$
HD 28975	145.	11.5	30	1900	475/1200	125/250
HD 27778	12.3	67(10)	51	5.3	50	975	400/800	75/150
HD 30122	0.70	...	61	3.8	...	450	275/525	...

^aThe first entry in the column for $n_{tot}(\text{Chem})$ applies to $I_{UV} = 0.5$, and the second 1.0. For the next column, $n_{tot}^{ex}(\text{C}_2)$, the two entries refer to I_{IR} equal to 0.5 or 1.0.

variation, we consider the effects of density, τ_{UV} , and the CO self-shielding factor (van Dishoeck & Black 1988; Visser et al. 2009). For gas density, we utilize $n_{tot}^{ex}(\text{CO})$ and $n_{tot}(\text{Chem})$, which vary by a factor of 3. In diffuse molecular gas, the CO abundance varies roughly as the total gas density, but as the amount of self shielding increases, with $N(\text{CO})$, photodissociation becomes less important and then the CO abundance no longer depends on gas density (as in the case for CN toward HD 29647 discussed in §3.4). Because the chemistry in the dense clump toward HD 29647 is not sensitive to density, a factor of 2 variation is more appropriate. We look at τ_{UV} next, where the range is 1.43 (to HD 30122) to 6.76 (HD 29647); the resulting variation in attenuation is a factor of ~ 200 . This is an upper limit, however, because CO photodissociation does not operate in the dense clump. If we estimate a 25% contribution of the clump to the reddening toward HD 29647, τ_{UV} is lowered to 5.07 and the variation in attenuation becomes of order 50. We suggest the remaining factor of 10 comes from the self-shielding factor. According to Fig. 13 in Sheffer et al. (2008), the self-shielding factor decreases from a value 0.30 at $N(\text{CO})$ of a few 10^{14} cm^{-2} to 0.01 at the edge of the region containing results from dark clouds with $N(\text{CO})$ about 10^{17} cm^{-2} . A column density of $1.45 \times 10^{17} \text{ cm}^{-2}$ is found toward HD 28975, where τ_{UV} is 3.72 and the attenuation is now a factor of 10. This column density is a factor of 200 greater than that toward HD 30122. Thus, the factor-of-5 decrease

in grain attenuation toward HD 28975 accounts for the difference in results for HD 30122. This rough calculation indicates that grain attenuation and self shielding play comparable roles in CO photochemistry when $N(\text{CO})$ approaches the values associated with dark molecular clouds.

We conclude the comparison with a discussion of excitation and gas temperatures and $n_{tot}^{ex}(\text{C}_2)$. The CO excitation temperature seems to be higher toward the stars probing dark cloud material, while the gas temperature inferred from H_2 and C_2 excitation is higher along the other two directions. Since dark molecular clouds have typical temperatures of 10 K, the T_k should decrease as more of the dark cloud material is sampled. Toward HD 29647, T_k and $T_{01}(\text{CO})$ have similar values, and our analysis of CO excitation from the IR absorption spectrum provides confirmation of the near equality. The CO molecule acts as a thermometer for dark clouds. Our analysis using RADEX in §3.2.2 suggests the need for optical depths approaching 100 in order to match our IGRINS results and Crutcher's (1985) for CO emission. The direction toward HD 28975 appears as an intermediate case with T_k somewhat higher than $T_{01}(\text{CO})$ and optical depths of about 10 for the predicted levels of emission. This indicates that ^{13}CO cooling is comparable to that of the more common isotopologue.

An estimate for I_{IR} toward HD 29647 is possible from the analysis in §3.5.3. In particular, adopting a stellar radius of $5.6 R_\odot$ and the distance between the star and nebula yields a dilution factor of $\approx 10^{-14}$, indicating the flux of radiation impinging on the nebula is about equal to the average interstellar flux or I_{IR} is about 2. However, C_2 excitation via optical pumping, which involves populating excited electronic levels followed by radiative cascades into the ground vibrational level, occurs by absorbing photons at wavelengths shorter than $1 \mu\text{m}$. As also noted in §3.5.3, there is no evidence for a reflection nebula at visible wavelengths because the visual extinction is so large. If the visual extinction between the nebula and the surface of the nearside of the TMC is appreciable, there may not be a significant amount of pumping. Thus, an increase in the gas density derived from analysis of excited rotational levels in C_2 does not seem likely. Instead, the similar results for $n_{tot}^{ex}(\text{C}_2)$ among the four sight lines are possibly a consequence of the excitation taking place in diffuse molecular gas common to all our targets.

For the three directions mainly probing diffuse molecular gas (HD 27778, HD 30122, as well as HD 28975), an interesting dichotomy arises. When adopting the average flux, $n_{tot}(\text{Chem})$ and $n_{tot}^{ex}(\text{CO})$ are more similar; however, $n_{tot}^{ex}(\text{C}_2)$ is lower than the other densities. This is probably a consequence of basing our analyses on homogeneous density clouds and that the molecular species are assumed to occupy similar volumes. The responses to changes in the strength of the radiation field for $n_{tot}(\text{Chem})$ and $n_{tot}^{ex}(\text{C}_2)$ arises from details of the processes involved. An increase (decrease) in the strength requires an increase (decrease) in $n_{tot}(\text{Chem})$ to compensate for changes in the photodissociation rate when reproducing the observed column densities. Similarly, an increase in I_{IR} leads to a increase in $n_{tot}^{ex}(\text{C}_2)$ as discussed in [van Dishoeck & Black \(1982\)](#).

The observational results from studies of atomic and molecular absorption are precise enough that more sophisticated approaches are required to achieve agreement between measurements and model predictions significantly better than a factor of 2. As a first step, such models need to derive gas densities in a more consistent way by combining thermodynamics, chemistry, radiative transfer, and excitation. Then for each species of interest, integrated results through the modeled cloud would reveal the regions where the various processes are mainly taking place. Current PDR codes contain essentially all the necessary elements to perform such calculations. It is quite possible that we are seeing differences in total proton density because our diagnostics are located in different portions of a cloud. Such a possibility was noted above for $n_{tot}^{ex}(\text{C}_2)$ and schematically presented in [Pan et al. \(2005\)](#). They developed their picture of a diffuse cloud in part by comparing the b -values obtained for different species. Since the b -values indicate that turbulence dominates over thermal motions, [Pan et al. \(2005\)](#) viewed b -values as revealing the number of clumps sampled by the lines from various species. A smaller b -value arises because fewer clumps are intercepted, suggesting the observations probe a more restricted portion of the cloud. The first step can be time independent, because many processes in diffuse atomic and molecular clouds (the envelopes of self-gravitating molecular clouds) take place under steady-state conditions. Then time-dependent phenomena, such as turbulence, can be introduced for a more complete description of diffuse interstellar matter.

4.4. *A Comparison to Other Studies of the TMC*

4.4.1. *Observations of the Whole Cloud*

We now examine how our study fits into the global picture developed from measurements across the TMC (Flagey et al. 2009; Goldsmith et al. 2008; Narayanan et al. 2008; Pineda et al. 2010) as well as other observations of interstellar gas in Taurus (Paradis et al. 2012; Lee et al. 2006). While we already considered the results on dust emission from Flagey et al. (2009) for our targets in §3.5, some of their other findings are worth discussing. The average dust temperature across the TMC is 14.5 ± 1.0 K, with colder filaments seen in the far-IR emission maps in the middle of warmer material. One such filament lies in the vicinity of the sight line to HD 28975, and multiple filaments surround the sight line to HD 29647. Emission from poly-cyclic aromatic hydrocarbons (or PAHs) and very small grains (VSGs) are correlated, but there is no relationship with emission from large grains. Abundance variations on sub-pc scales of a factor of a few are seen in the PAH and VSG emission, including the more diffuse portions of the TMC with A_V up to a few mag. The far-IR dust opacity was shown to correlate very well with the visual extinction derived from near-IR images and indicated an increase in dust emissivity relative to the diffuse ISM. Their models of the large scale dust emission revealed an overall reduction in the interstellar radiation field, which was incorporated into our analyses above; the strength of the field also showed significant variations in different regions of the TMC.

Goldsmith et al. (2008) created a 100 square degree map of the TMC in emission from the $J = 1 \rightarrow 0$ lines of CO and ^{13}CO , sampled on a $20''$ grid. The map was divided into three regions: one without molecular emission, one with only CO emission, and one showing emission from both isotopologues. Intensities were integrated over velocity from $+2$ to $+9$ km s $^{-1}$. As seen in our Fig. 1, the molecular emission is very filamentary. Peak emission occurs between $+5$ and $+8$ km s $^{-1}$, the interval where we observe strong molecular absorption. Goldsmith et al. (2008) note, however, that emission at about $+10$ km s $^{-1}$ (where we see absorption toward HD 26751 in Appendix C) might not be associated with the TMC. The pixels with no emission suggested an upper limit of $N(\text{CO})$ of 7.5×10^{15} cm $^{-2}$, indicating that the direction toward HD 30122 probed this region of the map. The region showing

only CO emission contained about half the gas, with $N(\text{H}_2)$ less than $2.1 \times 10^{21} \text{ cm}^{-2}$ and an average value for $N(\text{CO})$ of about $3.6 \times 10^{16} \text{ cm}^{-2}$. The sight line toward HD 27778 may probe this type of material. For the region containing both CO and ^{13}CO emission, the average $N(\text{CO})$ spanned a range from 1.3×10^{17} to approximately $1 \times 10^{18} \text{ cm}^{-2}$, consistent with our interpretation for the kind of material probed by HD 28975 and HD 29647. Goldsmith et al. (2008) also used the models by van Dishoeck & Black (1988) to place the results into context, finding (1) the region with no CO emission had H_2 columns less than 10^{21} cm^{-2} , (2) that with only CO emission had values between 10^{21} and about $3 \times 10^{21} \text{ cm}^{-2}$, and (3) that with emission from both CO and ^{13}CO ranged over 1.5 to $10 \times 10^{21} \text{ cm}^{-2}$. For the material analyzed in this paper, we have a measurement (toward HD 27778) and estimates (toward HD 29647 and HD 30122) for $N(\text{H}_2)$ in units of 10^{20} cm^{-2} , 6.2 (Rachford et al. 2002), ~ 30 (see §§4.1.1, 4.1.3), and 4.4 [from our $N(\text{CH})$ and a $N(\text{CH})/N(\text{H}_2)$ ratio of 3.5×10^{-8} from Sheffer et al. (2008)]. Clearly, the sight line toward HD 30122 is similar to regions without CO emission, and HD 29647 samples a region with both isotopologues. It appears that HD 27778 probes gas that is somewhere between regions with and without CO emission based on the CO and H_2 results for this sight line. Narayanan et al. (2008) described details of the observations used in creating the maps and showed the emission in 1 km s^{-1} intervals. For the four lines of sight discussed here, the emission peaked at velocities between 5 and 7 km s^{-1} , where we see the strongest molecular absorption.

These CO and ^{13}CO maps formed the basis for additional analyses. In particular, Pineda et al. (2010) used them for a comparison of H_2 columns derived from dust extinction with the Two Micron All Sky Survey (2MASS) on scales of $200''$. Other improvements to the analyses included recent molecular data, adoption of RADEX for radiative transfer, and comparisons with the updated photochemical code of Visser et al. (2009). The TMC again was divided into three regions based on CO and ^{13}CO emission. Emphasis was placed on results for the CO-to- H_2 conversion factor, $x(\text{CO}) = N(\text{H}_2)/I_{\text{CO}}$, where I_{CO} is the integrated intensity of line emission. A typical value for the conversion factor throughout the cloud was $2.1 \times 10^{20} \text{ cm}^{-2}(\text{K km s}^{-1})^{-1}$. Using our estimate for $N(\text{H}_2)$ from the previous paragraph and I_{CO} from Liszt (2008), we find a very similar value for

$x(\text{CO})$ toward HD 29647, reinforcing our conclusion that this star probes dark cloud material. For A_V less than 3 mag, the conversion factor could be two orders of magnitude smaller. Pineda et al. (2010) averaged nearly 10^6 spectra for the region showing no emission and obtained an average value for $N(\text{CO})$ of $7.8 \times 10^{14} \text{ cm}^{-2}$, much like the value toward HD 30122. This reveals the effort needed to obtain CO column densities typically found in diffuse molecular clouds (e.g., Sheffer et al. 2008). Pineda et al. (2010) found a linear correlation between visual extinction and $N(\text{CO})$ for A_V from 3 to 10 mag with a CO/H₂ ratio of $\sim 10^{-4}$, as we found for the gas toward HD 29647. Their modeling results based on the photochemistry described by Visser et al. (2009) reveal other similarities to our analyses. For A_V less than 5 mag, their data are best described by a varying CO/H₂ ratio, and for T_k of 15 K, the models yield a $n_{\text{tot}}(\text{H})$ of about 800 cm^{-3} ; our analyses suggest such densities apply to the material toward HD 28975 and HD 29647 (and possibly toward HD 27778). The models also indicate a reduced radiation field and that half the mass of the cloud is in the region without detectable amounts of ¹³CO.

There are two large-scale surveys including the TMC that provide useful comparisons. First, Paradis et al. (2012) follow the approach taken by Planck Collaboration et al. (2011), except they use extinction instead of far IR emission to study the presence of CO-dark gas and the CO-to-H₂ conversion factor. The visual extinction comes from Dobashi (2011) and is based on 2MASS data. The more diffuse regions give the optimal value for $A_V/N_{\text{tot}}(\text{H})$; for the solar neighborhood the value is $6.53 \times 10^{-22} \text{ mag cm}^2$, which agrees very well with the UV result of Bohlin et al. (1978) for R_V of 3.1. The global conversion factor is $1.67 \times 10^{20} \text{ cm}^{-2}(\text{K km s}^{-1})^{-1}$, with significant variations, and it is $2.27 \times 10^{20} \text{ cm}^{-2}(\text{K km s}^{-1})^{-1}$ for gas in Taurus, comparable to what Pineda et al. (2010) found. Paradis et al. (2012) obtained average values for the locations of the H-to-H₂ transition (A_V of ~ 0.2 mag) and the H₂-to-CO transition (A_V of ~ 1.5 mag). The location of the H-to-H₂ transition agrees with the results from UV absorption (Savage et al. 1977), and that of the H₂-to-CO transition is consistent with our conclusions that the gas probed by HD 28975 and HD 29647 is predominantly molecular. These authors also find a significant fraction of the molecular content in Taurus in the form of CO-dark gas. Second, Lee et al. (2006) describe diffuse far UV observations of the Taurus

region acquired with SPEAR/FIMS. Because the spatial resolution is coarse (pixel size of 0.2° by 0.2° smoothed by 3 pixels), detailed comparisons with our results are not possible. The measurements can distinguish cloud cores from halos surrounding the cores. The map includes directions toward HD 27778, HD 28975, HD 29647, HD 30122, as well as HD 26571. The sight lines toward HD 28975 and HD 29647 sample edges of cores, while the other sight lines lie within halos. Cloud cores, with $A_V > 1.5$ mag, obscure background far UV radiation, while the flux seen from halos comes from scattered foreground light. Molecular hydrogen fluorescence, which is only seen from halos, is examined with the model of [Black & van Dishoeck \(1987\)](#). The low values for gas density ($\sim 50 \text{ cm}^{-3}$) and $N(\text{H}_2)$ (0.8×10^{20}) are likely caused by the large pixels. Of note is that again a reduced radiation field is required to reproduce the observations.

4.4.2. *Observations of Specific Regions*

A number of efforts examined chemical species associated with diffuse molecular gas in specific dark clouds or regions of the TMC. Since these species are seen along the lines of sight to our stellar background sources, we now describe how our results fit into the perspective of these findings for molecular cloud envelopes. The works by [Sakai et al. \(2012\)](#) and [Ebisawa et al. \(2015\)](#) studied CH emission from HCL-2 and OH emission from material to the east of the cloud, respectively. We already noted that the CH column density lies below the extension of the relationship for diffuse clouds ([Sakai et al. 2012](#)); here we focus on the kinematics. For two of the four regions examined, both a narrow ($\sim 0.3 \text{ km s}^{-1}$) and broad component ($\sim 1.5 \text{ km s}^{-1}$) are seen. Where a narrow component is observed, it contributes about 20% to the total CH column density. Only the narrow component is present in the dense core, while the broad component is more extended and represents the diffuse envelope. The transition from narrow to broad component is probably sharp, but their measurements with a $3.2'$ beam could not resolve it. The presence of the two components might be caused by dissipation of turbulence. Only the broad component is observed in the region closest to HD 29647, TMC-1(NH_3).

All four hyperfine transitions in OH were measured by [Ebisawa et al. \(2015\)](#). The material to the east of HCL-2 is more diffuse and lies about 4.5 pc from the direction of HD 29647. Intensity

anomalies caused by non-LTE effects were found, allowing them to infer gas temperatures over a wide range in density (10^2 to 10^7 cm^{-3}). Toward the center of their strip map acquired with a 8.2 beam, T_k is 53 ± 1 K and increases to about 60 K at the boundaries. The averaged spectrum yields 60 ± 3 K and $N(\text{OH})$ of $(4.4 \pm 0.3) \times 10^{14}$ cm^{-2} . The lines only reveal the broader component (~ 1.3 km s^{-1}). The emission appears to arise from CO-dark gas. The line of sight toward HD 27778 probes similar material, and has a comparable amount of OH (Felenbok & Roueff 1996), $(1.02 \pm 0.04) \times 10^{14}$ cm^{-2} . The somewhat smaller value toward the star could be a consequence of the much larger beam used in the radio measurements.

The surveys by Goldsmith et al. (2008), Narayanan et al. (2008), and Pineda et al. (2010) were used in more focused efforts. Of most relevance to our results, we discuss measurements of emission from H_2 (Goldsmith et al. 2010), from C I and II (Orr et al. 2014), and from CH and OH (Xu et al. 2016a; Xu & Li 2016b). Goldsmith et al. (2010) obtained data on S(0) through S(3) transitions in H_2 for three boundary regions (see Fig. 1), a Linear Edge [RA(J2000) = $4^{\text{h}} 38^{\text{m}} 00^{\text{s}}$ and DEC(J2000) = $+27^\circ 00' 00''$ at the center of the nominal slit position], the Filament [RA(J2000) = $4^{\text{h}} 50^{\text{m}} 30^{\text{s}}$ and DEC(J2000) = $+25^\circ 17' 30''$], and the Globule [RA(J2000) = $4^{\text{h}} 26^{\text{m}} 45^{\text{s}}$ and DEC(J2000) = $+25^\circ 39' 00''$]. The Linear Edge and the Globule regions lie near the center of Fig. 1, while the Filament is near the eastern edge of the TMC. The study emphasized the Linear Edge because it was less complex. The other studies acquired their data on the Linear Edge as well. The emission and relative populations were analyzed with the Meudon PDR code (Le Petit et al. 2006), but the high excitation temperature (210 K) suggested the presence of other processes such as the dissipation of turbulence. The observed ortho-to-para ratio revealed the effects of turbulent diffusion, bringing colder interior gas to the surface. The peak intensity occurred beyond the edge in ^{13}CO emission for the Linear Edge, where the column densities for $J = 2$ through 5 were 1.3×10^{18} , 1.6×10^{17} , $\sim 1.1 \times 10^{16}$, and $\sim 8.5 \times 10^{15}$ cm^{-2} , respectively. These column densities can be compared with the results for the sight line toward HD 27778 (Jensen et al. 2010), which samples similar material: 3.0×10^{18} , 3.5×10^{17} , 4.4×10^{15} , and 2.1×10^{14} cm^{-2} , respectively. The UV data for HD 27778 show more excitation in the lower rotational levels and less in the highest ones. The line of sight

toward HD 210839 (λ Cep) in the survey by [Jensen et al. \(2010\)](#) has column densities for these levels that are most similar to the *Spitzer* measurements ([Goldsmith et al. 2010](#)). Somewhat lower column densities were derived for the Filament.

[Orr et al. \(2014\)](#) also utilized the Meudon PDR code in an attempt to reproduce their observations. The most consistent model indicated the need for a weak radiation field, a low ambient $^{12}\text{C}/^{13}\text{C}$ ratio of 43, a primary cosmic-ray ionization rate of about $5 \times 10^{-17} \text{ s}^{-1}$, and significant sulfur depletion. The emission from neutral carbon and the CO isotopologues appears to come from dark cloud material. While no C II emission was seen, the modeling results reveal a rapid decline in C^+ abundance with depth into the cloud. [Orr et al. \(2014\)](#) suggested ionized carbon was associated with the diffuse component of the cloud. They provided integrated intensities for CO ($\approx 13 \text{ K km s}^{-1}$) and ^{13}CO (3 to 4 K km s^{-1}). For two of the directions in our survey, HD 27778 and HD 29647, [Liszt \(2008\)](#) quoted respective values of 7.17(0.43) and 16.35(5.84) K km s^{-1} , where the numbers in parentheses are for ^{13}CO . Again these values imply the absorption toward HD 27778 samples diffuse material just beyond the edge, while that toward HD 29647 is more like a dark cloud. The predictions for a rapid decline in C^+ abundance are consistent with the small amount of C^+ we infer for the gas toward HD 29647.

Observations of CH and OH emission from the Linear Edge were described by [Xu et al. \(2016a\)](#) and [Xu & Li \(2016b\)](#). Two velocity components are present, one changes from +5.3 to +6.0 km s^{-1} , while the other appears at +6.8 km s^{-1} . The bluer emission comes from the region where ^{13}CO emission is present; the redder component is mainly confined to the gas beyond the edge associated with only detectable amounts of CO. The OH column density is about 50% greater in the more diffuse portions of the strip map, with values of about $4 \times 10^{14} \text{ cm}^{-2}$. In other words, the column densities along the strip intersecting the Linear Edge are about 2 to 4 times greater than what is measured in the diffuse molecular gas toward HD 27778. Column densities for CH were more uncertain because limited information on excitation temperature and optical depth was available. The authors interpret the shift in velocity, the apparent excess in CH at A_V less than about 1 mag, and line anomalies

in the OH satellite line at 1712 MHz as evidence for a continuous or C-shock caused by colliding streams or gas flow.

Our CH^+ results can provide further insight into this phenomenon because C-shocks would be a site of significant production for this molecular ion (e.g., Flower et al. 1985; Draine & Katz 1986). Subsequent reactions can transform CH^+ into CH. This route proceeds in low density gas ($< 100 \text{ cm}^{-3}$) because CH^+ is destroyed rapidly through reactions with H, H_2 , and electrons at higher densities. Another route at higher densities synthesizes CH (as well as CN and most of the CO) and is initiated by a reaction involving radiative association, $\text{C}^+ + \text{H}_2 \rightarrow \text{CH}_2^+ + \text{photon}$. According to Pan et al. (2005), there is a linear relationship between CH associated with CH^+ and CH^+ in terms of column densities. In other words when CH is made in the network involving CH^+ , the molecules have comparable column densities. According to Table 2, each of the velocity components containing absorption from both CH and CH^+ has a much smaller column of CH^+ . The same applies for the results on the sight line toward HD 26571 in Appendix C. Thus, these five directions that sample diffuse and dark molecular clouds, the same type of material seen in CO and ^{13}CO in the TMC (Goldsmith et al. 2008; Pineda et al. 2010), contain little CH^+ . While turbulence is clearly present in the form of non-thermal line widths, evidence for significant amounts of shocked gas appears less convincing.

Rybarczyk et al. (2020) measured small-scale features traced by H I absorption toward radio sources having component structure separated by less than a few arcminutes, or linear scales from 10^3 to 10^5 AU. Resolved velocity components were treated separately in the analysis. Both changes in peak optical depth and line width contribute to the observed variation. These appear to be a transient feature of the cold neutral medium. Differences in optical depth of about 0.05 are common, but reaching factors of 10 larger in some instances. The median change in optical depth corresponds to changes in H I column density of about $3.5 \times 10^{19} \text{ cm}^{-2}$, though for a sight line in Taurus (3C111) the variation in column density is $\sim 2 \times 10^{20} \text{ cm}^{-2}$. For gas in the TMC this corresponds to density variations of 1000 cm^{-3} . Only limits are available for another source in Taurus (3C123), which lies closer to the directions of the stars in our sample. It is important to note that if the material is sheet-

like, the density estimate could be a factor of a few smaller (Heiles 1997). The inferred densities are similar to what we find for the molecular gas probed by HD 27778, HD 28975, HD 29647, and HD 30122. Considering absorption from the same set of species as in the present paper, Pan et al. (2001) detected spatial variations in molecular column densities across members of HD 206267 A/C/D and HD 217035 A/B with separations (10^3 to 10^4 AU) like those used in Rybarczyk et al. (2020). Such a study is not possible for most of the material in the TMC because similar systems tend to be too faint or are in front of the TMC. One interesting exception is the companion to HD 27778 (BD+23° 683), a star with B and V of 8.40 and 8.2 about $30''$ (4,600 AU) from the primary (see Fig. 7).

5. CONCLUDING REMARKS

We presented results on atomic and molecular absorption seen at UV, visible, and IR wavelengths that probe four portions of the TMC. Gas temperatures and densities were inferred from analyses of molecular excitation and chemistry. The line of sight toward HD 29647 differed from the others in a number of ways. It was by far the most molecule rich, with a CO column density of 10^{18} cm^{-2} , and its gas temperature (derived from C_2 and CO excitation) was only 10 K. It appears that essentially all the carbon is in CO. The CH column density for the amount of CO observed revealed a deficit when comparison was made to typical diffuse molecular clouds. The value of $N(\text{K I})$ relative to the total proton column density to this star based on the amount of reddening indicated an enhanced potassium depletion. We surmised that this sight line mainly probes gas associated with the dark molecular cloud, HCL-2; the low value for $N(\text{CH})$ comes from the conversion of CH into other species, including CO. The directions toward HD 27778 and HD 30122 are like diffuse molecular clouds observed elsewhere, while the gas toward HD 28975 represents an intermediate case. For instance, the fraction of carbon in CO for these three sight lines is about 4%, 0.4%, and 30%, respectively.

We also placed our results for these directions within the context of the large-scale maps of CO and ^{13}CO emission (Goldsmith et al. 2008) and dust extinction (Pineda et al. 2010). These authors distinguished three types of material – no emission from CO, only emission from ^{12}CO , and emission

from both isotopologues. The four sight lines emphasized in the present paper can be associated with one of these types. Clearly, HD 30122 probes gas without any CO emission, while HD 28975 and HD 29647 sample gas with emission from both isotopologues. The situation for the gas toward HD 27778 is a little less clear; its properties place it at the interface between regions with and without CO emission. Though only a statistical perspective, the comparison provides a useful means of connecting the two observational techniques.

The analyses conducted on excitation and chemistry yielded values for total proton density that spanned a range of a factor of 2. We discussed the possibility in §4.3 that this is due to the processes considered by us taking place in distinct regions (or portions) of the diffuse gas surrounding molecular clouds, and suggested that further progress in understanding the transition from diffuse material to molecular cloud requires more sophisticated treatments. Available comprehensive PDR codes allow users to incorporate thermodynamics, chemistry, radiative transfer, and excitation into their models for interstellar material. Both generic clouds and focused efforts based on extensive observations for specific lines of sight are necessary.

This work used the Immersion Grating Infrared Spectrometer (IGRINS) that was developed under a collaboration between the University of Texas at Austin and the Korea Astronomy and Space Science Institute (KASI) with the financial support of the US National Science Foundation under grants AST-1229522 and AST-1702267, of the University of Texas at Austin, and of the Korean GMT Project of KASI. This paper includes data taken at The McDonald Observatory of The University of Texas at Austin. These results made use of the Lowell Discovery Telescope. Lowell Observatory is a private, non-profit institution dedicated to astrophysical research and public appreciation of astronomy and operates the LDT in partnership with Boston University, the University of Maryland, the University of Toledo, Northern Arizona University, and Yale University. This work was carried out in part at the Jet Propulsion Laboratory, which is operated for NASA by the California Institute of Technology. This research made use of the SIMBAD database operated at CDS, France. We

thank Dan Welty for the many discussions, for comments on an earlier version of the paper, and for providing data for comparison.

APPENDIX

A. TOTAL EQUIVALENT WIDTHS

Since previous results on interstellar absorption toward HD 28975 and HD 29746 are available, we provide a comparison for total equivalent widths (W_λ) in Tables 8 and 9; Table 8 also lists our results for the sight line toward HD 30122. The first comparison involves the species observed with TS and UVES, except C_2 , where the results appear in the next table. In both tables, additional previously unpublished results are presented. These include our measurements on HJST with the coude 6 foot camera ($R \sim 200,000$) and the Sandiford Spectrograph ($R \sim 60,000$) on the 2.1 m telescope at McDonald Observatory. Also shown are C_2 measurements by D. Welty (2018, private communication) from his analysis of the UVES data as well as results acquired with the Astrophysical Research Consortium echelle spectrograph (ARCES) on the 3.5 m telescope at Apache Point Observatory (Thorburn et al. 2003), where total column densities were presented.

For the most part, the measurements in Tables 8 and 9 show good agreement, especially when considering the uncertainties. The consistency involving the more recent and more precise results from TS and UVES toward HD 29647 should be noted. The blends seen in C_2 with ARCES agree well with the results of summing the W_λ 's for the individual transitions when they are resolved; the same applies to the Q(8)/P(4) blend in the spectrum acquired by Lutz & Crutcher (1983). Where differences are seen, the numerous contaminating stellar features near the interstellar lines of CH and CN in the data of Crutcher (1985) and Slyk et al. (2008) toward HD 29647 or the quality of the CN data (Federman et al. 1994) are the likely cause. For completeness, the equivalent widths for the CO lines detected in IGRINS spectra of HD 28975 and HD 29647 are given in Table 10; we believe these to be the first detections of these lines for the two sight lines.

The diffuse gas toward HD 27778 has been the subject of many efforts. We compare our analysis of UVES spectra with our previously unpublished results with the 6 foot camera and the Sandiford

Table 8. Compilation of Total Equivalent Widths at Visible Wavelengths

Line	HD 28975		HD 29647							HD 30122	
	TS	FSLCVJ94 ^a	TS	UVES	6 foot	Sandiford	CW82 ^a	C85 ^a	ARCES ^b	SBGK08 ^a	TS
K I λ 7698	151.6 ± 1.1^c	...	90 ± 0.5	80.8 ± 0.2	89.6 ± 0.9	...	93 ± 9	110 ± 10	64.5 ± 2.3
Ca II K	132.6 ± 4.6	...	$(164.1 \pm 4.1)^d$	$(147.9 \pm 0.7)^d$...	$(218)/\leq 7.2^d$...	$(280 \pm 15)^d$	63.5 ± 0.7
Ca II H	$(117.1 \pm 1.0)^d$...	$(150)/\leq 9.3^d$...	$(150 \pm 10)^d$
Ca I λ 4226	7.6 ± 0.5	...	2.6 ± 0.5	4.0 ± 0.3	≤ 8	≤ 0.5
CH λ 4300	36.9 ± 0.8	50.0 ± 4.0	34.0 ± 0.5	^e	48 ± 7	65.0 ± 5.0	68.07 ± 0.8	11.7 ± 0.3
CH λ 3886	...	31.0 ± 6.0	...	12.5 ± 0.4	...	17.2 ± 4.2	...	19 ± 3	16.0 ± 2.5	14.60 ± 0.6	...
CH λ 3890	...	≤ 18.0	...	9.3 ± 0.5	...	10.8 ± 4.4	...	23 ± 3
CH λ 3878	...	≤ 18.0	...	5.3 ± 0.5	...	≤ 14.9	6.5 ± 1.5
CH ⁺ λ 4232	11.8 ± 1.1	...	4.4 ± 0.8	4.6 ± 0.3	≤ 12	1.8 ± 0.4
CH ⁺ λ 3957	3.2 ± 0.3	...	≤ 5.2	...	≤ 11
CN $B-X$ (0, 0) R(0)	55.3 ± 1.9	30.0 ± 6.0	45.0 ± 1.4	46.7 ± 0.2	...	54.4 ± 3.6	...	62 ± 3	44.0 ± 1.5	46.37 ± 0.4	4.5 ± 0.4
CN $B-X$ (0, 0) R(1)	32.1 ± 1.9	11.0 ± 3.0	34.4 ± 1.4	32.9 ± 0.2	...	31.5 ± 2.6	...	46 ± 3	30.0 ± 1.0	40.42 ± 0.8	1.4 ± 0.4
CN $B-X$ (0, 0) P(1)	18.4 ± 1.9	≤ 18.0	22.3 ± 1.4	23.9 ± 0.2	...	18.5 ± 2.6	...	31 ± 3	24.0 ± 1.0	30.34 ± 0.5	0.8 ± 0.4
CN $B-X$ (0, 0) R(2)	2.4 ± 0.2	6 ± 2	...
CN $B-X$ (0, 0) P(2)	1.6 ± 0.2	5 ± 2	...
CN $B-X$ (1, 0) R(0)	16.7 ± 0.6	21 ± 4	...
CN $A-X$ (2, 0) ^S R ₂₁ (0)	3.4 ± 0.5	...	4.2 ± 0.3
NH $A-X$ (0, 0) R(1)	3.5 ± 0.9

^aReferences: FSLCVJ94, CW82, C85, and SBGK85 are Federman et al. 1994, Chaffee & White 1982, Crutcher 1985, and Slyk et al. 2005, respectively.

^bARCES data discussed in Thorburn et al. 2003 (Welty 2019, private communication).

^cThe units are mÅ.

^dPossible stellar contamination. The upper limits for the Sandiford are our attempt to estimate the interstellar contribution.

^eStellar contamination present.

Table 9. Compilation of Total Equivalent Widths for the C₂ A–X (2, 0) Band

Line	HD 28975		HD 29647				
	TS	TS	UVES ^a	HBvD83 ^b	LC83 ^b	C85 ^b	ARCES ^c
R(0)	3.7 ± 0.5 ^d	17.1 ± 0.4	18.1 ± 0.4/17.8 ± 0.5	21 ± 2.5	17.2 ± 2.3	17 ± 5	17.8 ± 0.7
R(2)	8.8 ± 0.8	13.4 ± 0.4	14.5 ± 0.4/14.5 ± 0.4	17 ± 2.5	13.9 ± 1.8	17 ± 5	13.0 ± 0.4
Q(2)	10.8 ± 0.8	16.8 ± 0.4	17.6 ± 0.4/17.2 ± 0.5	21 ± 2.5	16.7 ± 2.0	17 ± 5	14.8 ± 0.5
P(2)	...	2.6 ± 0.3	3.6 ± 0.3/3.1 ± 0.3	...	5.8 ± 1.7	...	3.0 ± 0.4
R(4)	6.2 ± 0.9	5.0 ± 0.4	6.1 ± 0.4/5.6 ± 0.4	≤ 2.5	5.7 ± 1.8	≤ 10	7.6 ± 0.4 ^e
Q(4)	9.5 ± 0.9	7.8 ± 0.4	9.4 ± 0.4/9.6 ± 0.5	12 ± 2.5	7.9 ± 2.2	≤ 10	8.1 ± 0.5
P(4)	...	3.0 ± 0.4	2.8 ± 0.3/2.6 ± 0.3	...	^f	...	^f
R(6)	...	3.2 ± 0.5	3.0 ± 0.3/3.3 ± 0.4	≤ 2.5	3.3 ± 0.3
Q(6)	^g	4.4 ± 0.4	3.0 ± 0.3/> 3.1 ± 0.3	7 ± 2.5	3.2 ± 0.4
P(6)	1.9 ± 0.4/< 2.0 ± 0.3
R(8)	...	1.6 ± 0.4	1.7 ± 0.4/...	≤ 2.5	^e
Q(8)	3.4 ± 0.7	2.5 ± 0.3	2.8 ± 0.4/2.6 ± 0.3	≤ 2.5	4.2 ± 1.7 ^f	...	5.1 ± 0.5 ^f
P(8)/...	2.1 ± 0.2
R(10)	...	≤ 1.2	0.9 ± 0.3/0.8 ± 0.3
Q(10)	...	≤ 1.2	1.9 ± 0.4/1.5 ± 0.3
P(10)/...	1.3 ± 0.3
R(12)/...
Q(12)/...
P(12)/...	1.1 ± 0.1

^aOur results from UVES spectrum followed by those of D. Welty (Welty 2018, private communication).

^bReferences: HBvD83, LC83, and C85 are Hobbs et al. 1983, Lutz & Crutcher 1983, and Crutcher 1985, respectively.

^cARCES data discussed in Thorburn et al. 2003 (Welty 2018, private communication).

^dThe units are mÅ.

^eBlended with R(8).

^fBlended with P(4).

^gAffected by cosmic ray.

Spectrograph, along with those of D. Welty and colleagues with the Coude Feed Telescope at Kitt Peak National Observatory and ARCES (Welty 2019, private communication), in Table 11. The comparison with published results appears in Table 12; the results from more focused studies, those involving only one or two lines, are given here. Joseph et al. (1986) reported a value of 29 mÅ for the

Table 10. Total Equivalent Widths for the CO (2, 0) Rovibrational Band

Line	HD 28975	HD 29647
R(0)	11.8 ± 1.9^a	59.6 ± 1.0
R(1)	11.7 ± 1.8	69.4 ± 1.1
P(1)	...	37.8 ± 1.1
R(2)	5.5 ± 1.8	35.0 ± 1.1
P(2)	...	30.8 ± 1.0
R(3)	...	10.1 ± 1.0
P(3)	...	6.5 ± 1.0

^aThe units are mÅ.

Table 11. Same as Table 8 for HD 27778: Previously Unpublished Data

Line	UVES	6 foot	Sandiford	Coude Feed ^a	ARCES ^b
K I λ 7698	84.2 ± 0.2	87.3 ± 1.1	...	$84.0 \pm 1.2/83.8 \pm 1.0$	$88.1 \pm 0.2/88 \pm 2$
Ca II K	60.3 ± 0.3	...	61.9 ± 1.2	$61/63.1 \pm 0.9$	$62.4 \pm 0.5/62 \pm 1$
Ca II H	35.7 ± 0.3	...	40.1 ± 2.1	.../...	.../...
Ca I λ 4226	1.2 ± 0.2	≤ 3.3	≤ 5.1	$<2.4/...$	$1.3 \pm 0.1/1.5 \pm 0.3$
CH λ 4300	22.5 ± 0.3	...	20.2 ± 0.9	$21.0 \pm 0.9/21.6 \pm 0.6$	$22.3 \pm 0.3/22.5 \pm 1.0$
CH λ 3886	6.1 ± 0.2	...	7.6 ± 1.3	$7.4 \pm 0.8/...$	$6.1 \pm 0.3/5.5 \pm 1.0$
CH λ 3890	3.8 ± 0.2	...	4.3 ± 1.0	.../...	$4.3 \pm 0.4/4.5 \pm 1.5$
CH λ 3878	2.1 ± 0.2	...	≤ 5.1	.../...	$2.1 \pm 0.3/2.1 \pm 0.7$
CH ⁺ λ 4232	6.2 ± 0.2	3.7 ± 0.7	5.4 ± 1.0	$9.5 \pm 0.8/...$	$6.6 \pm 0.2/6.7 \pm 0.5$
CH ⁺ λ 3957	3.7 ± 0.2	$4.4 \pm 0.7/...$	$4.4 \pm 0.3/4.5 \pm 1.5$
CN $B-X$ (0, 0) R(0)	30.6 ± 0.3	...	32.5 ± 1.3	$30.9 \pm 0.6/30.3 \pm 1.2$	$30.6 \pm 0.5/31.0 \pm 1.0$
CN $B-X$ (0, 0) R(1)	11.2 ± 0.2	...	9.9 ± 1.4	$12.5 \pm 0.6/11.9 \pm 1.4$	$11.1 \pm 0.5/11.0 \pm 1.0$
CN $B-X$ (0, 0) P(1)	6.0 ± 0.2	...	5.2 ± 1.2	$7.2 \pm 0.6/6.1 \pm 1.1$	$6.1 \pm 0.5/5.5 \pm 0.7$
CN $B-X$ (1, 0) R(0)	3.3 ± 0.1/...	.../...
CN $A-X$ (1, 0) R(1)	0.9 ± 0.1/...	.../...
NH $A-X$ (0, 0) R(1)	1.2 ± 0.1/...	.../...

^aThe first entry under Coude Feed involves results with Camera No. 5 and the second with Camera No. 6 (Welty 2019, private communication).

^bARCES data analyzed by D. Welty (first entry) and J. Thornburn (second entry); the molecular results were discussed in Thornburn et al. 2003 and Fan et al. 2017. Fan et al. 2017 also analyzed the atomic data. (Welty 2019, private communication).

Table 12. Same as Table 8 for HD 27778: Published Data

Line	UVES	FSLCVJ94 ^a	RM95 ^a	MSBMHKG05 ^a	WGMK08 ^a	SBGK08 ^a	WGBK09a,b ^a	WGGK14 ^a
K I λ 7698	84.2 ± 0.2	87.7 ± 4.1
Ca II K	60.3 ± 0.3	51.9 ± 6.1
Ca II H	35.7 ± 0.3	27.7 ± 4.7
Ca I λ 4226	1.2 ± 0.2
CH λ 4300	22.5 ± 0.3	21.7 ± 0.6	...	22.1 ± 0.3	23.3 ± 0.3	23.57 ± 0.8	23.82 ± 2.67^b	22.42 ± 0.28
CH λ 3886	6.1 ± 0.2	6.7 ± 0.8	7.7 ± 0.9	7.59 ± 0.6	9.75 ± 0.78	7.04 ± 0.86
CH λ 3890	3.8 ± 0.2	≤ 6.3	5.1 ± 0.6	...	4.82 ± 0.64	4.47 ± 0.78
CH λ 3878	2.1 ± 0.2	≤ 8.1	2.83 ± 0.69
CH ⁺ λ 4232	6.2 ± 0.2	9.3 ± 0.3	6.55 ± 0.27
CH ⁺ λ 3957	3.7 ± 0.2	4.9 ± 0.3	3.39 ± 0.28
CN $B-X$ (0, 0) R(0)	30.6 ± 0.3	27.3 ± 0.5	30.64 ± 0.13	...	32.6 ± 0.7	31.14 ± 0.4
CN $B-X$ (0, 0) R(1)	11.2 ± 0.2	10.5 ± 0.5	11.73 ± 0.13	...	12.4 ± 0.3	11.89 ± 0.6
CN $B-X$ (0, 0) P(1)	6.0 ± 0.2	4.9 ± 0.4	6.44 ± 0.23	...	7.1 ± 0.5	6.65 ± 0.5
CN $B-X$ (1, 0) R(0)	3.3 ± 0.1	...	3.44 ± 0.23	10.48 ± 2.44	...
CN $A-X$ (1, 0) R(1)	0.9 ± 0.1	...	1.03 ± 0.22	3.38 ± 1.97	...
NH $A-X$ (0, 0) R(1)	1.2 ± 0.1

^aReferences: FSLCVJ94, RM95, MSBMHKG05, WGMK08, SBGK85, WGBK09a,b, and WGGK14 are Federman et al. 1994, Roth & Meyer 1995, Megier et al. 2005, Weselak et al. 2008, Slyk et al. 2008, Weselak et al. 2009a,b, and Weselak et al. 2014, respectively.

^bSince the other entries are based on data from the same spectroscopic setup with the same measures of W_λ , we listed the results for CH λ 4300 from Weselak 2019 in this column.

W_λ of the CN (0, 0) R(0) line, Meyer & Roth (1991) reported the first detection of NH absorption from diffuse gas, with W_λ of 1.1 ± 0.3 mÅ, and Krelowski et al. (1999) obtained measures of W_λ of 24.0 and 23.8 mÅ for CH λ 4300 and of 7.8 mÅ for CH⁺ λ 4232. For atomic species, we note two additional studies: Welty & Hobbs (2001) gave W_λ of 83.6 ± 1.3 mÅ for the K I line and Megier et al. (2009) provided values of 52 ± 6.6 and 28 ± 4.9 mÅ for the Ca II K and H lines. This extensive set of results shows very good agreement, with variations within 2σ levels.

B. CALCIUM IONS AND THE ELECTRON DENSITY

The emphasis for the main text was molecules and related species like K I. Here we briefly interpret results associated with absorption from calcium atoms and ions in our spectra. In the picture of a diffuse cloud presented by Pan et al. (2005), Ca I and Ca II absorption mainly arises from the outer

regions of the cloud where the gas densities are lower [$n_{tot}(\text{H}) < 100 \text{ cm}^{-3}$, e.g., [Rice et al. \(2018\)](#)] and the gas is predominantly atomic. The ionization balance for calcium allows us to estimate the electron density for this material.

The component structures in terms of column densities for Ca I and Ca II appear in Table 2. For the lines of sight toward HD 27778 and HD 28975, the components with the largest Ca II columns and the only ones indicating absorption from Ca I are the molecular ones, a consequence that most of the material is associated with these components. For the clouds toward HD 30122, the sight line with the least amount of molecular material in our sample, the individual components have comparable amounts of singly-ionized Ca and only a limit on the amount of neutral calcium. The two directions resembling a typical diffuse molecular cloud have total column densities of Ca II similar to the well-studied examples toward *o* Per, ζ Per, and ζ Oph (e.g., [Welty et al. 1996](#)); the Ca I column density toward HD 27778 is also similar (see [Welty et al. 2003](#)). The material toward HD 28975 has factor of a few larger total $N(\text{Ca II})$ and is more closely associated with the molecular components; a similar enhancement in $N(\text{Ca I})$ is found. According to [Rice et al. \(2018\)](#), these Ca II components are atomic gas associated with molecular cloud envelopes, in this case TMC. The other components seen in Ca II toward HD 28975 and HD 30122 likely represent absorption from the cold (100 K) neutral medium or the warm (10,000 K) medium detected at radio wavelengths in H I.

For the diffuse molecular clouds toward HD 27778 and HD 28975, ionization balance provides us with an estimate of $n(e)$. Since the recombination rates are temperature dependent (e.g., [Shull & Van Steenberg 1982](#)), we adopt a kinetic temperature of 50 K for both directions. The outcome also depends on the radiation field enhancement factor I/I_0 and we perform calculations for both $I/I_0 = 1.0$ and 0.5 (just as we did for the chemical analysis discussed in Section 3.4). For HD 27778, these calculations yield $n(e)$ of 0.18 and 0.09 cm^{-3} for $I/I_0 = 1.0$ and 0.5, respectively. Similar calculations for HD 28975 yield $n(e)$ of 0.24 and 0.12 cm^{-3} . For HD 27778, the estimates for $n(e)$ obtained here are somewhat lower than those derived from the analysis of CN rotational excitation, which indicated $n(e)$ in the range 0.21 to 0.34 cm^{-3} (Section 3.2.3). For HD 28975, the above estimates for $n(e)$ are consistent with the upper limit provided by the CN analysis. The electron

densities could be larger if the temperature of the Ca I- and Ca II-bearing gas is higher than 50 K. For example, the estimates for $n(e)$ would increase by $\sim 50\%$ if a kinetic temperature of 80 K were adopted instead. Because severe stellar contamination prevents us from measuring interstellar Ca II toward HD 29647, we are not able to extract an electron density for this sight line.

While the values for $n(e)$ derived from CN excitation and ionization balance between neutral and singly-ionized calcium are comparable, analyses of other ion pairs tend to suggest lower electron densities (Welty et al. 2003). Welty et al. found that the results for $N(\text{Ca I})/N(\text{Ca II})$ were typically a factor of ten larger than those for other pairs, such as $N(\text{C I})/N(\text{C II})$, $N(\text{Mg I})/N(\text{Mg II})$, $N(\text{S I})/N(\text{S II})$, and $N(\text{Fe I})/N(\text{Fe II})$. These relative results did not depend on whether or not charge exchange between ions and small grains (e.g., Weingartner & Draine 2001) was included. It is also important to remember that our analyses refer to diffuse molecular gas (CN) and atomic gas (ionization balance), but the gas densities are a factor of several or more greater in the molecular material. Thus, the ionization fraction, $x(e)$, appears to be much larger than that obtained from C^+ observations (Sofa et al. 1997) although C^+ is often assumed to be the main contributor of electrons in neutral diffuse gas. Welty et al. (2003) noted that inclusion of charge exchange with small grains leads to more consistent results for the amount of ionization, but not for all ion pairs.

C. THE LINE OF SIGHT TOWARD HD 26571

A number of observational studies included measurements on atomic and molecular species for the gas in front of HD 26571, a B8III star (Mooley et al. 2013) with $E(B - V)$ of 0.27 and an R_V comparable to the average interstellar value (Wegner 2003). While the line of sight to this star is located in the lower right-hand corner of Fig. 1, where at higher contrast CO emission is seen (Goldsmith et al. 2008; Narayanan et al. 2008; Pineda et al. 2010), there are no high-resolution measurements for the type of analyses conducted above. Of particular relevance to the work presented here are the data on absorption from Dickman et al. (1983), Joseph et al. (1986), Crawford (1990), and Thorburn et al. (2003) and on CO emission by Dickman et al. (1983) and van Dishoeck et al. (1991). Tables 13 and 14 provide compilations of published and previously unpublished total equivalent widths. The molecular absorption occurs at $+10 \text{ km s}^{-1}$. The maps of CO and ^{13}CO emission

(Narayanan et al. 2008) peak at +9 to +11 km s⁻¹ along the line of sight. In what follows, we use data from ARCES on CH, C₂, and CN from the analysis by D. Welty (2020, private communication). The higher resolution spectra of Crawford (1990) (3 km s⁻¹) reveal only one molecular component, and ours from the HJST coudé 6 foot camera (1.5 km s⁻¹) show an additional very weak component in K I absorption with W_λ of 2.5(0.4) mÅ. For K I, our W_λ associated with molecular absorption is adopted. Table 14 also includes the column densities for each rotational level.

The results displayed in Tables 13 and 14 are generally consistent, with a few exceptions. Like HD 29647, HD 26571 is a late-type peculiar B star, causing severe stellar contamination especially in the vicinity of the interstellar Ca II, CH⁺, and Na I D lines (see Crawford 1990). The data for the Na I transitions are not included in the tables. We used curves of growth to convert equivalent widths into column densities. For CH and CN, consistency was sought between weak and strong lines, thereby providing an estimate for the b -value. The CH transitions at 3886 and 4300 Å were used, as were CN $\lambda\lambda 7906, 3874$ from $N'' = 0$. Because CH $\lambda 3886$ only represents one of the Λ -doubling components in the ground state and because the members of the doublet should have equal populations, the value for $N(\text{CH})$ was multiplied by 2. The lines associated with the other component, $\lambda\lambda 3878, 3890$, were not seen in the ARCES spectrum. A b -value of 1.2 km s⁻¹ best describes the data and is consistent with the analysis performed by Crawford (1990) and with the line widths seen in CO emission (Dickman et al. 1983; van Dishoeck et al. 1991). This b -value was also adopted for absorption from C₂ and K I, while a slightly larger value for CH⁺ of 1.5 km s⁻¹ was chosen in light of the findings by Pan et al. (2005). Since the optical depth at line center for CH⁺ $\lambda 4232$ is only 0.10, the curve-of-growth results do not differ much from considering an optically thin line in the calculation. When more than one line yielded a column density for a rotational level, we quote the weighted mean. Moreover, the estimates for CO column density from UV absorption (Dickman et al. 1983; Joseph et al. 1986) and millimeter-wave emission (Dickman et al. 1983; van Dishoeck et al. 1991) are similar, yielding values of 10¹⁶ cm⁻² to within 30%.

The column densities for CH, C₂, CN, CH⁺, and K I, along with the column densities for rotational levels in C₂ and CN, are used in our analyses on excitation and chemistry. We obtain respective

Table 13. Same as Table 8 for HD 26571

Line	6 foot	Sandiford	JSSC86 ^a	c90 ^a	FSLCVJ94 ^a	Coude Feed ^b	ARCES ^c
K I λ 7698	94.9 ± 0.8	94.1 ± 1.1	$96.9 \pm 0.5/99.3 \pm 0.4$
Ca II K	...	186.7 ± 3.3^d	...	90 ± 23	$174 \pm 1^d/175 \pm 6^d$
Ca II H	...	104.4 ± 4.6^d/108 \pm 9 ^d
Ca I λ 4226	≤ 1.5	≤ 1.7/ ≤ 2.0
CH λ 4300	...	16.1 ± 0.6	...	13 ± 2	10.3 ± 1.3	...	$13.8 \pm 0.3/13.6 \pm 0.8$
CH λ 3886	...	5.2 ± 0.9	$4.7 \pm 0.4/3.7 \pm 1.0$
CH λ 3890	...	1.3 ± 0.5/ ≤ 4.0
CH λ 3878	...	≤ 3.3/1.7 \pm 0.5
CH ⁺ λ 4232	3.9 ± 0.6	^d	...	≤ 6.0	$3.5 \pm 0.3/\leq 6.9$
CH ⁺ λ 3957	...	$\leq 2.2^d$/ $\leq 4.0^d$
CN <i>B-X</i> (0, 0) R(0)	...	21.7 ± 0.7	22	21 ± 3	$22.7 \pm 0.6/21.5 \pm 1.0$
CN <i>B-X</i> (0, 0) R(1)	...	5.2 ± 0.9	...	11 ± 4	$9.3 \pm 0.5/9.5 \pm 0.7$
CN <i>B-X</i> (0, 0) P(1)	...	7.0 ± 0.8	...	8 ± 3	$3.7 \pm 0.4/4.1 \pm 0.7$
CN <i>A-X</i> (2, 0) R ₁ (0)	≤ 4.5	$2.4 \pm 0.4/3.0 \pm 0.6$

^aReferences: JSSC86, C90, and FSLCVJ94 are Joseph et al. 1986, Crawford 1990, and Federman et al. 1994, respectively.

^bThe entry under Coude Feed involves results with Camera No. 5 (Welty 2020, private communication).

^cARCES data analyzed by D. Welty (first entry) and J. Thornburn (second entry); the molecular results were discussed in Thornburn et al. 2003. (Welty 2020, private communication).

^dLikely affected by stellar contamination.

Table 14. Compilation of Results for the C₂ A–X (2, 0) Band Toward HD 26571

Line	FSLCVJ94 ^a	ARCES ^b	Column Density 10 ¹² cm ⁻²
R(0)	4.2 ± 1.0 ^c	5.0 ± 0.4/4.5 ± 1.0 ^c	5.4 ± 0.4 ^d
R(2)	7.3 ± 1.1	5.9 ± 0.7/6.9 ± 1.3	15.3 ± 0.8
Q(2)	8.2 ± 1.1	6.9 ± 0.4/6.9 ± 1.0	...
P(2)	...	2.7 ± 1.0/5.5 ± 1.3	...
R(4)	7.3 ± 1.2	5.0 ± 0.3 ^e /4.0 ± 1.3	11.7 ± 1.4
Q(4)	9.5 ± 1.2	5.4 ± 0.6/4.8 ± 1.2	...
P(4)	...	3.3 ± 0.3 ^f /6.0 ± 1.5	...
R(6)	...	1.0 ± 0.3/≤ 3.0	3.4 ± 1.0
Q(6)	...	≤ 2.4/≤ 4.0	...
P(6)	...	≤ 1.2/≤ 3.0	...
R(8)	...	^e /...	3.7 ± 1.1
Q(8)	...	^f /≤ 3.0	...
P(8)/≤ 3.0	...
R(10)	...	≤ 1.2/...	≤ 4.4
Q(10)/≤ 3.0	...

^aReference: FSLCVJ94 is Federman et al. 1994.

^bARCES data analyzed by D. Welty (first entry) and J. Thornburn (second entry); the molecular results were discussed in Thornburn et al. 2003. (Welty 2020, private communication).

^cThe units for W_λ are mÅ.

^dColumn density appears in first row for that rotational level.

^eBlended with R(8).

^fBlended with Q(8).

values for $N(\text{CH})$, $N(\text{C}_2)$, $N(\text{CN})$, $N(\text{CH}^+)$, and $N(\text{K I})$ of 20.8×10^{12} , 39.5×10^{12} , 10.7×10^{12} , 4.2×10^{12} , and 1.91×10^{12} cm⁻². The column densities for the C₂ rotational levels appear in Table 14. Those for CN are 7.52×10^{12} cm⁻² for $N = 0$ and 3.22×10^{12} cm⁻² for $N = 1$, and $T_{01}(\text{CN})$ is 2.8 ± 0.1 K. The analysis for C₂ excitation reveals a gas temperature of 20 (10 to 30) K and total proton density of $\sim 100(225)$ cm⁻³ when adopting I_{IR} of 0.5(1.0). A temperature of 20 K and τ_{UV} of 1.65 were used in our simple chemical model. The model yields total proton densities of 275(550)

cm^{-3} when considering similar strengths for the UV field permeating the gas. For these physical conditions, the predictions for $N(\text{C}_2)$ and $N(\text{CN})$ are 45.2×10^{12} and $8.7 \times 10^{12} \text{ cm}^{-2}$, respectively, independent of the strength of the radiation field. The value for $N_{\text{tot}}(\text{H})$ ranges from 1.6×10^{21} to $2.9 \times 10^{21} \text{ cm}^{-2}$, depending on whether it is based on $E(B - V)$ or $N(\text{K I})$. This indicates that the fractional abundance of CO is between 3.4×10^{-6} and 6.2×10^{-6} , only a few percent of the carbon budget. Finally, using $N(\text{CH})$ to predict the CO column density (Sheffer et al. 2008) leads to $N(\text{CO})$ of about 10^{15} cm^{-2} , a factor of 10 less than observed. It appears that the line of sight toward HD 26571 is very similar to the one toward HD 27778, with a somewhat lower gas temperature, as shown in Table 7.

Earlier studies of the interstellar material toward HD 26571 gave estimates of gas densities that we can compare with ours. As in our earlier comparisons, we do not adjust the input parameters. When the results are given in terms of density of collision partners, we multiply these by a factor of 1.5. Joseph et al. (1986) used C I excitation to infer a pressure and assumed a gas temperature of 40 K to infer a total proton density between 180 and 2000 cm^{-3} . They also obtained a density from C I excitation toward HD 27778 of 175 to 800 cm^{-3} ; the range is similar to what we find from our analyses (see Table 7). Crawford (1990) used an earlier version of our chemical model to extract a value for $n_{\text{tot}}(\text{Chem})$ from his CN measurements, obtaining 1300 cm^{-3} which is similar to the value quoted by Federman et al. (1994). From their analysis of CO excitation, van Dishoeck et al. (1991) obtained $n_{\text{tot}}^{\text{ex}}(\text{CO})$ between 750 and 2250 cm^{-3} with a preferred density of 1200 cm^{-3} . Besides modeling the CN chemistry, Federman et al. (1994) found a gas density from C_2 excitation of 800 cm^{-3} and a gas temperature of about 50 K, higher than we obtain. These results and ours are in reasonable agreement, especially when one considers the precision of the earlier absorption-line measurements. In light of the current results for $T_{01}(\text{CN})$ showing no excess over the CMB, we suggest treating the electron and molecular hydrogen densities, 0.59 and 5900 cm^{-3} , determined by Black & van Dishoeck (1991) as upper limits.

Facilities: McDonald:HJST(TS, IGRINS), VLT(UVES), Lowell:LDT(IGRINS)

Software: IRAF(Tody 1986, 1993), ISMOD(Sheffer et al. 2008), RADEX(van der Tak et al. 2007)

REFERENCES

- Bailer-Jones, C. A. L., Rybizki, J., Fouesneau, M., Mantelet, G., & Andrae, R. 2018, *AJ*, 156, 58
- Bally, J., & Langer, W. D. 1982, *ApJ*, 255, 143
- Black, J. H., & van Dishoeck, E. F. 1987, *ApJ*, 322, 412
- Black, J. H., & van Dishoeck, E. F. 1991, *ApJL*, 369, L9
- Black, J. H., & Willner, S. P. 1984, *ApJ*, 279, 673
- Bohlin, R. C., Savage, B. D., & Drake, J. F. 1978, *ApJ*, 224, 132
- Boland, W., & de Jong, T. 1984, *A&A*, 134, 87
- Brooke, J. S. A., Ram, R. S., Western, C. M., et al. 2014, *ApJS*, 210, 23
- Burgh, E. B., France, K., & Jenkins, E. B. 2010, *ApJ*, 708, 334
- Cartledge, S. I. B., Meyer, D. M., Lauroesch, J. T., et al. 2001, *ApJ*, 562, 394
- Cartledge, S. I. B., Lauroesch, J. T., Meyer, D. M., et al. 2004, *ApJ*, 613, 1037
- Chaffee, F. H., & White, R. E. 1982, *ApJS*, 50, 169
- Chu, Y.-H., & Watson, W. D. 1983, *ApJ*, 267, 151
- Cox, A. N. 2000, *Allen's Astrophysical Quantities*
- Cox, N. L. J., Cami, J., Farhang, A., et al. 2017, *A&A*, 606, A76
- Crawford, I. A. 1990, *MNRAS*, 243, 593
- Crutcher, R. M. 1985, *ApJ*, 288, 604
- Cutri, R. M., Skrutskie, M. F., van Dyk, S., et al. 2003, *VizieR Online Data Catalog*, II/246
- Dickman, R. L., Somerville, W. B., Whittet, D. C. B., et al. 1983, *ApJS*, 53, 55
- Dobashi, K. 2011, *PASJ*, 63, S1
- Draine, B. T. 1985, *ApJS*, 57, 587
- Draine, B. T., & Katz, N. 1986, *ApJ*, 306, 655
- Draine, B. T., & Lee, H. M. 1984, *ApJ*, 285, 89
- Draine, B. T., & Salpeter, E. E. 1979, *ApJ*, 231, 438
- Ducati, J. R. 2002, *VizieR Online Data Catalog*
- Ebisawa, Y., Inokuma, H., Sakai, N., et al. 2015, *ApJ*, 815, 13
- el-Qadi, W. H., & Stancil, P. C. 2013, *ApJ*, 779, 97
- Erman, P., & Iwamae, A. 1995, *ApJL*, 450, L31
- Fan, H., Welty, D. E., York, D. G., et al. 2017, *ApJ*, 850, 194
- Federman, S. R., Knauth, D. C., & Lambert, D. L. 1997, *ApJ*, 489, 758
- Federman, S. R., Strom, C. J., & Good, J. C. 1991, *AJ*, 102, 1393
- Federman, S. R., Strom, C. J., Lambert, D. L., et al. 1994, *ApJ*, 424, 772
- Felenbok, P., & Roueff, E. 1996, *ApJL*, 465, L57
- Fernando, A. M., Bernath, P. F., Hodges, J. N., et al. 2018, *JQSRT*, 217, 29
- Fitzpatrick, E. L., & Massa, D. 2007, *ApJ*, 663, 320

- Fixsen, D. J. 2009, *ApJ*, 707, 916
- Flagey, N., Noriega-Crespo, A., Boulanger, F., et al. 2009, *ApJ*, 701, 1450
- Flower, D. R., Pineau des Forets, G., & Hartquist, T. W. 1985, *MNRAS*, 216, 775
- Gaida, M., Ungerechts, H., & Winnewisser, G. 1984, *A&A*, 137, 17
- Galli, P. A. B., Loinard, L., Bouy, H., et al. 2019, *A&A*, 630, A137
- Gerin, M., de Luca, M., Goicoechea, J. R., et al. 2010, *A&A*, 521, L16
- Goldsmith, P. F. 2013, *ApJ*, 774, 134
- Goldsmith, P. F., Heyer, M., Narayanan, G., et al. 2008, *ApJ*, 680, 428
- Goldsmith, P. F., Velusamy, T., Li, D., et al. 2010, *ApJ*, 715, 1370
- Gredel, R., van Dishoeck, E. F., & Black, J. H. 1993, *A&A*, 269, 477
- Harrison, S., Faure, A., & Tennyson, J. 2013, *MNRAS*, 435, 3541
- Heays, A. N., Bosman, A. D., & van Dishoeck, E. F. 2017, *A&A*, 602, A105
- Heiles, C. 1997, *ApJ*, 481, 193
- Heyer, M. H., Snell, R. L., Goldsmith, P. F., et al. 1987, *ApJ*, 321, 370
- Hobbs, L. M., Black, J. H., & van Dishoeck, E. F. 1983, *ApJL*, 271, L95
- Høg, E., Fabricius, C., Makarov, V. V., et al. 2000, *A&A*, 355, L27
- Hupe, R. C., Sheffer, Y., & Federman, S. R. 2012, *ApJ*, 761, 38
- Indriolo, N., & McCall, B. J. 2012, *ApJ*, 745, 91
- Jenkins, E. B. 2009, *ApJ*, 700, 1299
- Jenkins, E. B., & Tripp, T. M. 2011, *ApJ*, 734, 65
- Jensen, A. G., Rachford, B. L., & Snow, T. P. 2007, *ApJ*, 654, 955
- Jensen, A. G., Snow, T. P., Sonneborn, G., et al. 2010, *ApJ*, 711, 1236
- Joseph, C. L., Snow, T. P., Seab, C. G., et al. 1986, *ApJ*, 309, 771
- Kalugina, Y., & Lique, F. 2015, *MNRAS*, 446, L21
- Kirk, J. M., Ward-Thompson, D., Palmeirim, P., et al. 2013, *MNRAS*, 432, 1424
- Knauth, D. C., Federman, S. R., Pan, K., et al. 2001, *ApJS*, 135, 201
- Kokkin, D. L., Bacskay, G. B., & Schmidt, T. W. 2007, *JChPh*, 126, 084302
- Krełowski, J., Ehrenfreund, P., Foing, B. H., et al. 1999, *A&A*, 347, 235
- Kurucz, R. L. 1979, *ApJS*, 40, 1
- Lacy, J. H., Sneden, C., Kim, H., et al. 2017, *ApJ*, 838, 66
- Lambert, D. L., Sheffer, Y., Gilliland, R. L., et al. 1994, *ApJ*, 420, 756
- Lavendy, H., Robbe, J. M., Chambaud, G., et al. 1991, *A&A*, 251, 365
- Le Petit, F., Nehmé, C., Le Bourlot, J., et al. 2006, *ApJS*, 164, 506
- Lee, D.-H., Yuk, I.-S., Jin, H., et al. 2006, *ApJL*, 644, L181
- Lee, J.-J., Gullikson, K., & Kaplan, K. 2017, *igrins/plp*, v2.1-alpha.3, Zenodo, 10.5281/zenodo.845059

- Lique, F., Spielfiedel, A., Feautrier, N., et al. 2010, JChPh, 132, 024303
- Liszt, H. S. 2008, A&A, 492, 743
- Liszt, H., & Lucas, R. 1996, A&A, 314, 917
- Liszt, H. S., & Lucas, R. 1998, A&A, 339, 561
- Liszt, H., & Lucas, R. 2002, A&A, 391, 693
- Lutz, B. L., & Crutcher, R. M. 1983, ApJL, 271, L101
- Mace, G., Kim, H., Jaffe, D. T., et al. 2016, Proc. SPIE, 99080C
- Mace, G., Sokal, K., Lee, J.-J., et al. 2018, Proc. SPIE, 107020Q
- Magnani, L., Chastain, R. J., Kim, H. C., et al. 2003, ApJ, 586, 1111
- Magnani, L., & Onello, J. S. 1995, ApJ, 443, 169
- Magnani, L., Onello, J. S., Adams, N. G., et al. 1998, ApJ, 504, 290
- Mattila, K. 1986, A&A, 160, 157
- McElroy, D., Walsh, C., Markwick, A. J., et al. 2013, A&A, 550, A36
- Megier, A., Strobel, A., Bondar, A., et al. 2005, ApJ, 634, 451
- Megier, A., Strobel, A., Galazutdinov, G. A., et al. 2009, A&A, 507, 833
- Messinger, D. W., Whittet, D. C. B., & Roberge, W. G. 1997, ApJ, 487, 314
- Meyer, D. M., & Roth, K. C. 1991, ApJL, 376, L49
- Miville-Deschênes, M.-A., & Lagache, G. 2005, ApJS, 157, 302
- Mizuno, A., Yamaguchi, R., Tachihara, K., et al. 2001, PASJ, 53, 1071
- Mooley, K., Hillenbrand, L., Rebull, L., et al. 2013, ApJ, 771, 110
- Morton, D. C. 2003, ApJS, 149, 205
- Myers, P. C., & Benson, P. J. 1983, ApJ, 266, 309
- Myers, P. C., Linke, R. A., & Benson, P. J. 1983, ApJ, 264, 517
- Najar, F., Ben Abdallah, D., Jaidane, N., et al. 2008, Chemical Physics Letters, 460, 31
- Najar, F., Ben Abdallah, D., Jaidane, N., et al. 2009, JChPh, 130, 204305
- Narayanan, G., Heyer, M. H., Brunt, C., et al. 2008, ApJS, 177, 341
- Nercessian, E., Benayoun, J. J., & Viala, Y. P. 1988, A&A, 195, 245
- Orr, M. E., Pineda, J. L., & Goldsmith, P. F. 2014, ApJ, 795, 26
- Pan, K., Federman, S. R., Sheffer, Y., et al. 2005, ApJ, 633, 986
- Pan, K., Federman, S. R., & Welty, D. E. 2001, ApJL, 558, L105
- Paradis, D., Dobashi, K., Shimoikura, T., et al. 2012, A&A, 543, A103
- Park, C., Jaffe, D. T., Yuk, I.-S., et al. 2014, Proc. SPIE, 91471D
- Patel, N. A., Goldsmith, P. F., Heyer, M. H., et al. 1998, ApJ, 507, 241
- Patel, N. A., Goldsmith, P. F., Snell, R. L., et al. 1995, ApJ, 447, 721
- Pineda, J. E., Caselli, P., & Goodman, A. A. 2008, ApJ, 679, 481
- Pineda, J. L., Goldsmith, P. F., Chapman, N., et al. 2010, ApJ, 721, 686

- Planck Collaboration, Ade, P. A. R., Aghanim, N., et al. 2011, *A&A*, 536, A17
- Planck Collaboration, Ade, P. A. R., Aghanim, N., et al. 2014, *A&A*, 571, A1
- Rachford, B. L., Snow, T. P., Tumlinson, J., et al. 2002, *ApJ*, 577, 221
- Rebull, L. M., Padgett, D. L., McCabe, C.-E., et al. 2010, *ApJS*, 186, 259
- Rice, J. S. 2018, Univ. of Toledo dissertation
- Rice, J. S., Federman, S. R., Flagey, N., et al. 2018, *ApJ*, 858, 111
- Ritchey, A. M., Federman, S. R., & Lambert, D. L. 2011, *ApJ*, 728, 36
- Ritchey, A. M., Federman, S. R., & Lambert, D. L. 2018, *ApJS*, 236, 36
- Robbe, J. M., Lavendy, H., Lemoine, D., et al. 1992, *A&A*, 256, 679
- Rosolowsky, E. W., Pineda, J. E., Foster, J. B., et al. 2008, *ApJS*, 175, 509
- Roth, K. C., & Meyer, D. M. 1995, *ApJ*, 441, 129
- Rothman, L. S., Jacquemart, D., Barbe, A., et al. 2005, *JQSRT*, 96, 139
- Rybarczyk, D. R., Stanimirović, S., Zweibel, E. G., et al. 2020, *ApJ*, 893, 152
- Sakai, N., Maezawa, H., Sakai, T., et al. 2012, *A&A*, 546, A103
- Savage, B. D., Bohlin, R. C., Drake, J. F., et al. 1977, *ApJ*, 216, 291
- Schlafly, E. F., Green, G., Finkbeiner, D. P., et al. 2014, *ApJ*, 786, 29
- Schmidt, T. W., & Bacskay, G. B. 2007, *JChPh*, 127, 234310
- Sheffer, Y., Rogers, M., Federman, S. R., et al. 2008, *ApJ*, 687, 1075
- Sheffer, Y., Rogers, M., Federman, S. R., et al. 2007, *ApJ*, 667, 1002
- Shull, J. M., & Van Steenberg, M. 1982, *ApJS*, 48, 95
- Slyk, K., Bondar, A. V., Galazutdinov, G. A., et al. 2008, *MNRAS*, 390, 1733
- Smith, R. G., Sellgren, K., & Brooke, T. Y. 1993, *MNRAS*, 263, 749
- Snedden, C., Lucatello, S., Ram, R. S., et al. 2014, *ApJS*, 214, 26
- Sofia, U. J., Cardelli, J. A., Guerin, K. P., et al. 1997, *ApJL*, 482, L105
- Sofia, U. J., Lauofroesch, J. T., Meyer, D. M., et al. 2004, *ApJ*, 605, 272
- Sonnentrucker, P., Welty, D. E., Thorburn, J. A., et al. 2007, *ApJS*, 168, 58
- Teixeira, T. C., & Emerson, J. P. 1999, *A&A*, 351, 292
- Thorburn, J. A., Hobbs, L. M., McCall, B. J., et al. 2003, *ApJ*, 584, 339
- Tody, D. 1986, *Proc. SPIE*, 627, 733
- Tody, D. 1993, *Astronomical Data Analysis Software and Systems II*, 52, 173
- Tull, R. G., Macqueen, P. J., Sneden, C., & Lambert, D. L. 1995, *PASP*, 107, 251
- van der Tak, F. F. S., Black, J. H., Schöier, F. L., et al. 2007, *A&A*, 468, 627
- van Dishoeck, E. F., & Black, J. H. 1982, *ApJ*, 258, 533

- van Dishoeck, E. F., & Black, J. H. 1988, *ApJ*, 334, 771
- van Dishoeck, E. F., & Black, J. H. 1989, *ApJ*, 340, 273
- van Dishoeck, E. F., Black, J. H., Phillips, T. G., et al. 1991, *ApJ*, 366, 141
- Visser, R., van Dishoeck, E. F., & Black, J. H. 2009, *A&A*, 503, 323
- Watson, W. D., Anicich, V. G., & Huntress, W. T. 1976, *ApJL*, 205, L165
- Weingartner, J. C. & Draine, B. T. 2001, *ApJ*, 563, 842
- Welty, D. E., & Hobbs, L. M. 2001, *ApJS*, 133, 345
- Welty, D. E., Hobbs, L. M., & Morton, D. C. 2003, *ApJS*, 147, 61
- Welty, D. E., Morton, D. C., & Hobbs, L. M. 1996, *ApJS*, 106, 533
- Wegner, W. 2003, *Astronomische Nachrichten*, 324, 219
- Wenger, M., Ochsenbein, F., Egret, D., et al. 2000, *A&AS*, 143, 9
- Weselak, T. 2019, *A&A*, 625, A55
- Weselak, T., Galazutdinov, G., Beletsky, Y., et al. 2009, *A&A*, 499, 783
- Weselak, T., Galazutdinov, G. A., Beletsky, Y., et al. 2009, *MNRAS*, 400, 392
- Weselak, T., Galazutdinov, G. A., Gnaciński, P., et al. 2014, *AcA*, 64, 277
- Weselak, T., Galazutdinov, G. A., Musaev, F. A., et al. 2008, *A&A*, 484, 381
- Whittet, D. C. B., Adamson, A. J., Duley, W. W., et al. 1989, *MNRAS*, 241, 707
- Whittet, D. C. B., Shenoy, S. S., Clayton, G. C., et al. 2004, *ApJ*, 602, 291
- Wright, E. L., Eisenhardt, P. R. M., Mainzer, A. K., et al. 2010, *AJ*, 140, 1868
- Xu, D., & Li, D. 2016, *ApJ*, 833, 90
- Xu, D., Li, D., Yue, N., et al. 2016, *ApJ*, 819, 22
- Yan, Q.-Z., Zhang, B., Xu, Y., et al. 2019, *A&A*, 624, A6
- Yang, B., Stancil, P. C., Balakrishnan, N., et al. 2010, *ApJ*, 718, 1062
- Yuk, I.-S., Jaffe, D. T., Barnes, S., et al. 2010, *Proc. SPIE*, 77351M
- Zucker, C., Speagle, J. S., Schlafly, E. F., et al. 2019, *ApJ*, 879, 125